

A NOVEL INTEGRATED SPACECRAFT ATTITUDE CONTROL SYSTEM USING  
VARIABLE SPEED CONTROL MOMENT GYROSCOPES: A LYAPUNOV-BASED  
APPROACH

By  
DOHEE KIM

A DISSERTATION PRESENTED TO THE GRADUATE SCHOOL  
OF THE UNIVERSITY OF FLORIDA IN PARTIAL FULFILLMENT  
OF THE REQUIREMENTS FOR THE DEGREE OF  
DOCTOR OF PHILOSOPHY

UNIVERSITY OF FLORIDA

2011

© 2011 Dohee Kim

To my parents, Sang-yeol Kim and Namsoon Hahn, and my brother, Dukyoon Kim for  
their unwavering support and constant encouragement

## ACKNOWLEDGMENTS

I would like to express sincere gratitude to my advisor, Warren E. Dixon, whose experience and motivation have been instrumental in the successful completion of my PhD. The guidance and the patience he has shown over the years have helped me mature in my research and as a professional. I would also like to extend my gratitude to my committee members Dr. Norman Fitz-Coy, Dr. Carl Crane, and Dr. Oscar Crisalle for the time and help they provided. Also, I would like to thank my coworkers, family, and friends for their support and encouragement.

## TABLE OF CONTENTS

	<u>page</u>
ACKNOWLEDGMENTS . . . . .	4
LIST OF TABLES . . . . .	8
LIST OF FIGURES . . . . .	9
LIST OF ABBREVIATIONS . . . . .	12
ABSTRACT . . . . .	13
CHAPTER	
1 INTRODUCTION . . . . .	17
1.1 Motivation and Problem Statement . . . . .	17
1.2 Contributions . . . . .	24
2 SYSTEM MODEL . . . . .	28
2.1 Kinematic Model . . . . .	28
2.2 VSCMG-actuated Satellite Model . . . . .	28
2.3 Singularities . . . . .	33
2.3.1 What is a singularity? . . . . .	34
2.3.2 Singularity of CMGs . . . . .	34
2.3.2.1 External singularity . . . . .	36
2.3.2.2 Internal singularity . . . . .	36
3 PRECISION IPACS IN THE PRESENCE OF DYNAMIC UNCERTAINTY . . . . .	38
3.1 Dynamic Model for IPACS in the Presence of Dynamic Uncertainty . . . . .	38
3.2 Control Objectives . . . . .	39
3.2.1 Attitude Control Objective . . . . .	39
3.2.2 Power Tracking Objective . . . . .	40
3.3 Adaptive IPACS . . . . .	41
3.3.1 Adaptive Attitude Control Development . . . . .	41
3.3.2 Adaptive Power Tracking Control Development . . . . .	45
3.3.3 Stability Analysis . . . . .	47
3.4 Simulation Study . . . . .	50
3.5 Summary . . . . .	59
4 INTEGRATED POWER REDUCTION AND ADAPTIVE ATTITUDE CONTROL SYSTEM OF A SATELLITE . . . . .	64
4.1 Coupled Dynamics . . . . .	64
4.1.1 Dynamics for VSCMGs . . . . .	64
4.1.2 Dynamics for a satellite actuated by VSCMGs . . . . .	67

4.2	Attitude Control Objective . . . . .	69
4.3	Attitude Control Development . . . . .	69
4.3.1	Stability Analysis . . . . .	75
4.4	Simulation Study . . . . .	77
4.4.1	Simulation Setup . . . . .	77
4.4.2	Simulation Results . . . . .	78
4.5	Summary . . . . .	85
5	A NEW INITIAL START-UP METHOD USING INTERNAL MOMENTUM MANAGEMENT OF VSCMGS . . . . .	86
5.1	Control Objectives . . . . .	86
5.1.1	Attitude Control Objective . . . . .	86
5.1.2	Flywheel Angular Momentum Management Objective . . . . .	86
5.2	Controller Development . . . . .	87
5.2.1	Adaptive Attitude Control Development . . . . .	87
5.2.2	Momentum Tracking Control Development . . . . .	92
5.2.3	Stability Analysis . . . . .	93
5.3	Numerical Examples . . . . .	95
5.3.1	Simulation Setup . . . . .	95
5.3.2	Simulation Results . . . . .	96
5.4	Summary . . . . .	103
6	A RNN-BASED ATTITUDE CONTROL METHOD FOR A VSCMG-ACTUATED SATELLITE . . . . .	105
6.1	Dynamic Model . . . . .	105
6.2	Control Objectives . . . . .	107
6.2.1	Attitude Control Objective . . . . .	107
6.2.2	Flywheel Angular Momentum Management Objective . . . . .	107
6.3	Adaptive RNN Controller . . . . .	107
6.3.1	Adaptive Attitude Control Development . . . . .	107
6.3.1.1	Open-Loop Error System . . . . .	107
6.3.1.2	Closed-Loop Error System . . . . .	112
6.3.2	Momentum Tracking Control Development . . . . .	115
6.3.3	Stability Analysis . . . . .	115
6.4	Numerical Example . . . . .	118
6.5	Summary . . . . .	121
7	A NEW SINGULARITY DETECTION METHOD FOR VSCMGS USING FLS 122	
7.1	Singularity Detection Strategy . . . . .	123
7.1.1	Passability Condition by Null Motion near Singularity . . . . .	123
7.1.2	Fuzzification . . . . .	125
7.1.3	Product Inference Engine . . . . .	128
7.1.4	Defuzzification . . . . .	128
7.2	Implementation of FLS-based singularity detection index . . . . .	129

7.3	Numerical Examples . . . . .	130
7.3.1	Simulation Setup . . . . .	130
7.3.2	Simulation Results . . . . .	130
7.4	Summary . . . . .	137
8	CONCLUSIONS AND FUTURE WORK . . . . .	138
8.1	Conclusions . . . . .	138
8.2	Future Work . . . . .	141
	REFERENCES . . . . .	142
	BIOGRAPHICAL SKETCH . . . . .	150

LIST OF TABLES

<u>Table</u>	<u>page</u>
4-1 Physical parameters for the VSCMG simulation. . . . .	77
4-2 Initial parameters for the VSCMG simulation. . . . .	77
5-1 Physical parameters for the VSCMG simulation. . . . .	95
5-2 Initial parameters for the VSCMG simulation. . . . .	96

LIST OF FIGURES

<u>Figure</u>	<u>page</u>
2-1 Geometry of satellite with $i^{th}$ VSCMG. . . . .	29
2-2 Pyramidal arrangement of 4 VSCMGs system. . . . .	30
2-3 Total angular momentum envelope of CMGs . . . . .	36
3-1 Quaternion tracking error $e(t)$ during closed-loop operation. . . . .	54
3-2 Transient response of the quaternion tracking error $e(t)$ . . . . .	54
3-3 Response of the quaternion tracking error $e(t)$ during the sudden increase in friction at 6,000 sec. . . . .	55
3-4 Desired power and energy profiles and actual closed-loop power tracking response. . . . .	55
3-5 Transient power and energy tracking error. . . . .	56
3-6 Power and energy tracking error response during sudden friction increase at 6,000 sec. . . . .	56
3-7 Control input gimbal rates $\dot{\delta}(t)$ and wheel accelerations $\dot{\Omega}(t)$ . . . . .	57
3-8 Transient response of the control input gimbal rates $\dot{\delta}(t)$ and wheel accelerations $\dot{\Omega}(t)$ . . . . .	58
3-9 Response of the control input gimbal rates $\dot{\delta}(t)$ and wheel accelerations $\dot{\Omega}(t)$ during sudden increase of friction parameters at 6,000 sec. . . . .	58
3-10 Wheel speeds $\Omega(t)$ during closed-loop controller operation. . . . .	59
3-11 Adaptive parameter estimates $\hat{\theta}_1(t)$ , $\hat{\theta}_2(t)$ , and $\hat{\theta}_3(t)$ during closed-loop operation. . . . .	60
3-12 Initial transient response of the vector elements of the adaptive estimate $\hat{\theta}_1(t)$ . . . . .	60
3-13 Response of the vector elements of the adaptive estimate $\hat{\theta}_1(t)$ during the sudden friction increase at 6,000 sec. . . . .	61
3-14 Initial transient response of the vector elements of the adaptive estimate $\hat{\theta}_2(t)$ . . . . .	61
3-15 Response of the vector elements of the adaptive estimate $\hat{\theta}_2(t)$ during the sudden friction increase at 6,000 sec. . . . .	62
3-16 Initial transient response of the adaptive estimate $\hat{\theta}_3(t)$ . . . . .	62
4-1 Quaternion tracking error $e(t)$ during closed-loop operation. . . . .	78
4-2 Actual control input gimbal rates $\dot{\delta}(t)$ and flywheel speeds $\Omega(t)$ . . . . .	79

4-3	Close-up of actual control input gimbal rates $\dot{\delta}(t)$ and wheel speeds $\Omega(t)$ when encountering extreme singularity. . . . .	79
4-4	Singularity measure function $f(\delta)$ , null motion switch $S(\delta)$ , and weight function $W(\delta)$ . . . . .	81
4-5	Null motion: gimbal reconfiguration and wheel deceleration error $\mu(t)$ . . . . .	81
4-6	Adaptive parameter estimates $\hat{\theta}_1(t)$ during closed-loop operation. . . . .	82
4-7	Adaptive parameter estimates $\hat{\theta}_2(t)$ during closed-loop operation. . . . .	82
4-8	Applied gimbal torque, gimbal friction torque, and total gimbal torque during closed-loop controller operation. . . . .	83
4-9	Close-up of applied gimbal torque, gimbal friction torque, and total gimbal torque during the entire closed-loop operation. . . . .	83
4-10	Applied wheel torque, wheel friction torque, and total wheel torque during closed-loop controller operation. . . . .	84
4-11	Close-up of applied wheel torque, wheel friction torque, and total wheel torque during closed-loop operation providing input power reduction. . . . .	84
5-1	Quaternion tracking error $e(t)$ for Case 1. . . . .	96
5-2	Control input gimbal rates $\dot{\delta}(t)$ and wheel accelerations $\dot{\Omega}(t)$ for Case 1. . . . .	97
5-3	Flywheel speed $\Omega(t)$ induced from internal momentum management for Case 1. . . . .	97
5-4	Singularity measure function $f(\delta)$ and null motion weight $S(\delta)$ for Case 1. . . . .	98
5-5	Null motion: gimbal reconfiguration and internal momentum tracking error $\mu(t)$ for Case 1. . . . .	99
5-6	Adaptive parameter estimates $\hat{\theta}_1(t)$ and $\hat{\theta}_2(t)$ for Case 1. . . . .	99
5-7	Transient response of adaptive parameter estimate $\hat{\theta}_1(t)$ for Case 1. . . . .	100
5-8	Transient response of adaptive parameter estimate $\hat{\theta}_2(t)$ for Case 1. . . . .	101
5-9	Control input gimbal rates $\dot{\delta}(t)$ and wheel accelerations $\dot{\Omega}(t)$ for Case 2. . . . .	102
5-10	Flywheel speed $\Omega(t)$ induced from internal momentum management for Case 2. . . . .	102
5-11	Singularity measure function $f(\delta)$ and null motion weight $S(\delta)$ for Case 2. . . . .	103
5-12	Null motion: gimbal reconfiguration and internal momentum tracking error $\mu(t)$ for Case 2. . . . .	104
6-1	Quaternion tracking error $e(t)$ during closed-loop operation. . . . .	118

6-2	RNN estimation error $\tilde{\eta}(\tilde{\Omega}, \tilde{\delta})$ during closed-loop operation. . . . .	119
6-3	Induced infinity norm of RNN weight matrices $\hat{W}(t), \hat{V}(t)$ . . . . .	119
6-4	Singularity measure function $h(\delta)$ , null motion weight $S(\delta)$ , and mode weight $W_c(\delta)$ . . . . .	120
7-1	Membership function for singularity measure index $f(\delta)$ . . . . .	127
7-2	Block diagram of FLS-based singularity detection method. . . . .	128
7-3	Quaternion tracking error $e(t)$ for Case 1. . . . .	131
7-4	Control input gimbal rates $\dot{\delta}(t)$ and wheel accelerations $\dot{\Omega}(t)$ for Case 1. . . . .	132
7-5	Flywheel speed $\Omega(t)$ for Case 1. . . . .	132
7-6	Singularity detection index $\Delta(t)$ and null motion condition $\det(Q)$ for Case 1. . . . .	133
7-7	Singularity measure index $f(\delta)$ , null motion weight $S(\Delta)$ , and mode weight $W(\Delta)$ for Case 1. . . . .	133
7-8	Null motion results for gimbal reconfiguration and wheel speed tracking error $\mu(t)$ for Case 1. . . . .	134
7-9	Parameter estimates $\hat{\theta}_1(t), \hat{\theta}_2(t)$ for Case 1. . . . .	134
7-10	Singularity detection index $\Delta(t)$ and null motion condition $\det(Q)$ for Case 2. . . . .	135
7-11	Singularity measure index $f(\delta)$ , null motion weight $S(\Delta)$ , and mode weight $W(\Delta)$ for Case 2. . . . .	135
7-12	Null motion results for gimbal reconfiguration and wheel speed tracking error $\mu(t)$ for Case 2. . . . .	136
7-13	Flywheel speed $\Omega(t)$ for Case 2. . . . .	136

## LIST OF ABBREVIATIONS

ACS	Attitude Control System
ADCS	Attitude Determination and Control System
AI	Artificial Intelligence
C.M.	Center of Mass
CMG	Control Moment Gyroscope
DCM	Direction Cosine Matrix
DGCMGs	Double Gimbal Control Moment Gyroscopes
DOF	Degree Of Freedom
FACETS	Flywheel Attitude Control and Energy Transmissions System
FLS	Fuzzy Logic System
FNNs	Feedforward Neural Networks
GUUB	Globally Uniformly Ultimately Bounded
IPACS	Integrated Power and Attitude Control System
ISS	International Space Station
MW	Momentum Wheel
NN	Neural Networks
RBF	Radial Basis Function
RNNs	Recurrent Neural Networks
RW	Reaction Wheel
SGCMGs	Single Gimbal Control Moment Gyroscopes
SHM	Safe Holde Mode
UF	University of Florida
UUB	Uniformly Ultimately Bounded
VSCMG	Variable Speed Control Moment Gyroscope

Abstract of Dissertation Presented to the Graduate School  
of the University of Florida in Partial Fulfillment of the  
Requirements for the Degree of Doctor of Philosophy

A NOVEL INTEGRATED SPACECRAFT ATTITUDE CONTROL SYSTEM USING  
VARIABLE SPEED CONTROL MOMENT GYROSCOPES: A LYAPUNOV-BASED  
APPROACH

By

Dohee Kim

December 2011

Chair: Warren E. Dixon

Major: Mechanical Engineering

A Variable Speed Control Moment Gyroscope (VSCMG) is a momentum exchange device used for attitude control in various objects such as satellite, aircraft, and underwater vehicles. The main body accomplishes the desired attitude maneuver by changing the direction of the angular momentum vector of the momentum exchange device. Momentum exchange devices such as VSCMG, Control Moment Gyroscope (CMG), and Reaction Wheel (RW) achieve precise attitude control since they operate in a continuous manner contrary to the on/off operation of gas jets. The VSCMG is regarded as a hybrid between a CMG and RW since the spinning rotor can be rotated or gimballed for momentum transfer with an extra degree of freedom (DOF) resulting from the variable speed flywheel. Hence, the VSCMG can take advantage of torque amplification like a conventional CMG and can additionally acquire several benefits like singularity escape, power tracking, internal momentum management, start-up, and so on by its extra DOF resulting from the flywheels with variable speed.

The focus of this dissertation is to develop various control laws and further a new singularity detection method for a VSCMG-actuated satellite in the presence of uncertain satellite inertia, uncertain actuator inertia, and uncertain dynamic and static friction. Using novel control laws, this research achieves attitude stabilization as well as energy storage, initial start-up, and power reduction in the presence of friction.

A kinematic model quantified by quaternion and a nonlinear VSCMG-actuated satellite dynamic model are developed in Chapter 2. To actively and effectively utilize CMG mode of VSCMG, analysis for CMG singularities is also included in this chapter.

In Chapter 3, an adaptive robust integrated power and attitude control system (IPACS) is presented for a VSCMG-actuated satellite. The key concept is that the VSCMG cluster stores kinetic energy by spinning up the flywheels during sunlight periods so that during eclipse periods supporting power for the satellite subsystems by spinning down its flywheels. Such energy storage capability can be used as a mechanical battery. The developed IPACS method is capable of achieving precision attitude control while simultaneously achieving asymptotic power tracking for a rigid-body satellite in the presence of uncertain friction in the VSCMG gimbals and wheels. In addition, the developed controller compensates for the effects of uncertain, time-varying satellite inertia properties. Some challenges encountered in the control design are that the control input is premultiplied by a non-square, time-varying, nonlinear, uncertain matrix and is embedded in a discontinuous nonlinearity.

In the presence of uncertain actuator friction, Chapter 4 provides an adaptive attitude controller developed for a satellite that is actuated by a pyramidal arrangement of four single gimbal VSCMGs. From a cascade connection of satellite, gimbal, and wheel dynamics equations, a backstepping method is exploited to develop the controller. Internal friction is included in each torque expressions of the gimbal and the wheel assemblies since friction effects are significant when scaling the size of the VSCMGs. A system utilizing internal friction can reduce the consumption of battery power when decelerating on the developed dynamic structure. A null motion strategy lets the wheels operate in deceleration mode while simultaneously performing the gimbal reconfiguration for singularity avoidance. The applied torques of the wheels containing friction losses contribute to power reduction when in deceleration mode.

Chapter 5 develops a new initial start-up method for a satellite actuated by a pyramidal arrangement of VSCMGs despite the effects of uncertain, time-varying satellite inertia properties and uncertain actuator inertia properties. The method provides closed-loop internal momentum tracking control to enable the flywheels to start from rest and reach desired wheel speeds in the transition from safe hold mode (SHM) to initial attitude acquisition mode. The proposed controller functioning as a VSCMG steering law is developed in terms of the gimbal rates and the flywheel accelerations which are weighted by a singularity measure. Specifically, using null motion, a strategy is developed to simultaneously perform gimbal reconfiguration for singularity avoidance and internal momentum management for flywheel start-up.

Using obvious benefits of artificial intelligence (AI) techniques which can effectively approximate nonlinearity and complexity, a recurrent neural network (RNN)-based adaptive attitude controller developed in Chapter 6 achieves attitude tracking in the presence of parametric uncertainty, actuator uncertainty, and nonlinear external disturbance torques, which do not satisfy the linear-in-the-parameters assumption (i.e., non-LP). The adaptive attitude controller results from a RNN structure while simultaneously acting as a composite VSCMG steering law. In addition to accurate attitude control, a null motion strategy is developed to simultaneously perform gimbal reconfiguration for singularity avoidance and wheel speed regularization for internal momentum management.

Chapter 7 develops a new singularity detection method using fuzzy logic system (FLS). If a specific type of singularity is detected, a VSCMG steering law can efficiently select operation modes such as CMG mode and RW mode corresponding to the singularity type. The FLS-based singularity detection method is based on the passibility condition by null motion near singularity to classify a singularity identity into elliptic and hyperbolic singularity, and then using additional information denoted as a conventional singularity measure index degenerate hyperbolic singularity can also be escaped. The FLS effectively extracts significant information from singularity with nonlinear and complex patterns.

By using the FLS-based singularity detection method, all internal singularities can be classified and escaped online.

# CHAPTER 1 INTRODUCTION

## 1.1 Motivation and Problem Statement

A control moment gyroscope (CMG) is an attitude actuator that generates torque by exchanging momentum with a main body. Compared to momentum exchange devices such as a reaction wheel (RW), CMGs yield advantages such as torque amplification and rapid response. CMGs can provide a precise attitude control and rapid retargeting in a continuous manner, whereas a thruster for attitude control operates on/off discontinuous gas jets with propellants affecting mass, power, and volume.

CMGs can be configured in different ways. The extra gimbal in a double gimbal control moment gyroscope (DGCMG) provides an additional degree of freedom (DOF). Additional DOF can be used for singularity avoidance strategies, but DGCMGs are mechanically complex and massive [30, 42, 82, 110]. Single gimbal control moment gyroscopes (SGCMGs) have a mechanically simpler structure which consists of single controllable gimbal and constant flywheel and can generate more torque amplification than DGCMGs. However, since a CMG system only changes the direction but not the magnitude of the angular momentum vector, SGCMGs inherently suffer from singularity problems. In a three-dimensional workspace, SGCMGs are unable to produce torque along an arbitrary singular direction since all admissible torque directions lie on a two-dimensional surface perpendicular to the singular direction. SGCMGs singularities are classified as an external/saturation singularity and an internal singularity. The specific arrangement of the gimbals affects the type and number of singularities.

A variable speed control moment gyroscope (VSCMG) combines the properties of a CMG and a RW in that the flywheel speed is variable, providing an extra DOF. This extended capability enables a VSCMG cluster to avoid internal elliptic and hyperbolic singularities. Therefore, VSCMGs can be considered a geometrically singularity-free device. If all the CMG torque axes lie in a plane, torque generated by the variable

flywheel of the VSCMG cluster will enable the CMG configuration to be out of the plane (i.e., RW mode). The extra DOF present in VSCMGs provides more robust options against singularity encounter than CMGs. For instance, the gimbal null solutions of CMGs allow the gimbal angles to reconfigure without any request of torque generation. The singularity avoidance method using gimbal null motions reduces/eliminates the amount of time that the VSCMG has to operate in RW mode when the CMG Jacobian becomes singular. Based on the quaternion-based kinematic model and the VSCMG-actuated satellite dynamic model developed in Chapter 2, the wheel null motions enable dual use objectives including: power storage as a mechanical battery (Chapter 3), wheel deceleration for power reduction (Chapter 4), and internal momentum tracking for initial start-up (Chapter 5) while maintaining precise attitude control.

In Chapters 3 - 6 of this dissertation, various intelligent control methods are developed for VSCMG-actuated satellite in the presence of uncertain satellite inertia, uncertain actuator inertia, and uncertain dynamic and static friction. In Chapter 7, a new singularity detection and classification method is developed using a fuzzy logic system (FLS) under analysis for CMG singularities in Chapter 2. Following the existence of the null motion, a type of singularity can be primarily detected into elliptic singularity and hyperbolic singularity, and then using additional information which is a conventional singularity measure index, the method can further discriminate degenerate hyperbolic singularities which do not affect the rank of CMG Jacobian.

By combining the attitude control capability of CMG with the energy storage capability of variable-speed flywheels, VSCMGs offer the potential to combine energy storage and attitude control functions in a single device. This integration of attitude control and energy storage functions can reduce the satellite bus mass, volume, and cost. In light of launch costs as a function of mass, the advantage of integrated functionality is apparent. The variable wheel spin rates of VSCMGs endow them with additional DOF, which can be used to achieve multiple objectives such as simultaneous attitude control

and energy storage. For this reason, VSCMGs are often utilized in the design of integrated power and attitude control system (IPACS) [1, 2, 21, 22, 25, 41, 43, 79, 84–86, 89, 92, 99, 100]. However, the energy storage and attitude control capabilities of VSCMGs can deteriorate over time due to changes in the dynamics such as bearing degradation and increased friction in the gimbals or wheels [68]. For example, the ramifications of friction buildup include degraded power transfer capabilities and potential destabilizing disturbances. Friction buildup in the constant speed CMGs on the Skylab space station and the Magellan satellite [32] resulted in catastrophic failures of those systems. The potential for a failure due to friction uncertainties/changes in the gimbal and flywheel dynamics necessitates special consideration in designing IPACS for VSCMG-actuated satellites. Motivated by the virtues of using VSCMGs, the problem of designing IPACS in the presence of uncertainties has been investigated by several researchers. In [89], a feedback control law is designed for a VSCMG-actuated satellite, which achieves asymptotic attitude regulation for a satellite with known inertia properties. Model-based and adaptive control strategies are presented in [15], which achieve asymptotic tracking for a spacecraft in the presence of constant uncertainty in the spacecraft inertia, while simultaneously tracking a desired energy/power profile. In [100], model-based and indirect adaptive controllers are developed for a spacecraft with uncertain inertia properties. An adaptive control algorithm is developed in [102], which achieves attitude control for a VSCMG-actuated satellite in the presence of unknown misalignments of the axis directions of the VSCMG actuators. The control developments in [15, 89, 100, 102] assume that the satellite inertia properties are constant. While this assumption may be valid for larger satellites, significant fluctuations in the overall satellite inertia can occur in smaller satellites (small-sats) due to the motion of the VSCMGs. Further, the controllers in [15, 89, 100] assume no dynamic uncertainty in the VSCMG actuators. While the aforementioned controllers perform well for applications involving large satellites, they may not be well suited for IPACS for VSCMG-actuated small-sats. The control development in [47, 48] and in

Chapter 3 is motivated by the desire to include the uncertain dynamics of the gimbals and flywheels in the control design for improved robustness to these disturbances.

The majority of research focused on VSCMGs has assumed ideal conditions such as frictionless flywheel and gimbal bearings and a system of VSCMGs as a rigid body. When scaling the size of CMGs/VSCMGs, the effects of friction present in the system are significant (i.e., due to less efficient bearings and motors and the lack of available hardware components) [63, 65, 68]. IPACS and/or flywheel attitude control and energy transmission system (FACETS) use VSCMGs for a mechanical battery by de-spinning the flywheels of the VSCMG and utilizing their kinetic energy [21, 40, 47, 76, 84, 100]. This approach may seem feasible for VSCMG systems with more efficient motors and bearings (i.e., large spacecraft); however, for smaller systems the effects of friction are more significant and cannot be neglected. Hence, Chapter 4 explores the utilization of bearing and/or motor friction to decelerate the VSCMG flywheels. Utilizing system friction in deceleration mode provides an avenue to reduce the consumption of battery power. Even if the friction coefficient is modeled, the friction model may not be able to reflect variable friction since it is difficult for the friction coefficient to be constantly predicted. Hence using an adaptation mechanism to estimate the uncertain friction coefficients can be an alternative. To develop a controller that accounts for uncertain friction, coupled dynamics of the satellite, gimbals, and wheels is developed in Chapter 4. Based on the coupled dynamics, a backstepping method is used to design adaptive control torques. The wheel deceleration mode resulting from the wheel null solution contributes to input power reduction.

Various spacecrafts use momentum devices such as momentum wheels (MWs), RWs or CMGs to maintain and/or perform precise attitude maneuvers. For these spacecrafts, the operational spin rate of the wheel must be obtained, and several wheel initialization methods have been investigated for initial acceleration [11, 31, 58]. A pitch MW method can be used during an initial attitude acquisition mode, where the wheel requires magnetorquers

to maintain its spin rate while providing attitude stabilization [11]. A pitch MW method can also be used to acquire the gyroscopic stiffness along the roll and yaw axes [31]. During the initial wheel acceleration and holding the nominal speed, the attitude determination and control system (ADCS) uses a sequential mode change of the MW controller and the magnetorquer while maintaining a nadir-pointing attitude with gravity-gradient stabilization. For initial start-up of RWs, wheel start-up and attitude stabilization can be achieved when transitioning from safe hold mode (SHM) and initial attitude acquisition mode by using four RWs with magnetoquers [58]. CMGs have also been employed in various large space missions such as Skylab, MIR, and international space station (ISS) to take advantage of the torque amplification and power saving properties of CMGs. Despite their benefits, singularities are an inherent problem for CMGs [26, 55, 59, 70, 77, 98]. Various solutions address the CMG singularity issue, and with the development of mini-CMGs [6, 9, 35, 49, 51, 60, 63, 65, 66, 68, 77], several recent space missions using CMGs have been launched or scheduled [8, 73, 75]. To achieve wheel start-up and stabilization with a CMG system, magnetorquers can be used to maintain cooperation with the ground station for desired configuration modification to accelerate the CMG wheels [73]. In general, previous space missions using CMGs use a separate feedback control loop to spin up the rotor to the required spin rate and maintain it while securing attitude stabilization using additional devices such as magnetorquers [88]. The extra degree of freedom present in VSCMGs provides an avenue to condense the initial start-up and initial attitude acquisition mode into one step. Hence, Chapter 5 is motivated by the question: *Can an additional DOF of VSCMG be used to start a system from rest?* The results in Chapter 5 focus on the development of a flywheel momentum management strategy to bring the actual flywheel momentum from zero momentum (i.e. initial start-up from rest).

To compensate for uncertain system parameters in Chapters 3 - 5, typical adaptive control methods are used. However, for complex and practical problems where accurate mathematical models may not be available, artificial intelligent method can be beneficial,

which can be used to approximate any nonlinear system within an arbitrarily small residual error [3, 36]. In particular, neural network (NN) is widely utilized to approximate uncertainties in dynamic systems [33], and NN-based control has proven to be an effective means of achieving accurate attitude control of satellites in the presence of dynamic uncertainty [10, 13, 29, 38, 61, 62, 69, 90, 93]. In [90], a NN-based controller is used to compensate for uncertainties resulting from atmospheric effects and non-rigidity which are often neglected in typical attitude control designs. Radial basis function (RBF) NNs are utilized in [93] for direct adaptive control in the presence of unmodeled effects and parametric uncertainty. In [50], Krish et al. investigate the use of back-propagation NNs to provide robust adaptive nonlinear satellite attitude control. The result in [50] illustrates the design and implementation of a neuro-controller for a nonlinear space station model. Attitude tracking and vibration stabilization of a flexible spacecraft are achieved in [38] using a RBFNN-based adaptive control design. Utilization of an additional gain technique (i.e., the Nussbaum gain technique) in [38] enabled Hu et al. to relax the sign assumption for high-frequency gain for a neural adaptive control. Although feedforward neural networks (FNNs) using multilayer perceptrons or radial basis function networks are effective to compensate for uncertainties and unmodeled disturbances, emerging research shows that recurrent neural networks (RNNs), where connections between units form a directed cycle, are superior to FNNs in both modeling of nonlinear systems and prediction of time-series states [12, 19, 39, 67]. The research in [19] illustrates the increased capability of RNNs over FNNs to contain time-varying and dynamic behavior in the presence of noise. In [67], Li et al. illustrate how a dynamical time-variant system can be effectively approximated using the internal state of a continuous-time RNN. The utilization of dynamically driven RNNs can be more efficient for identification and modeling of dynamic plants in a control-theoretic framework. The capability of RNN modeling for nonlinear dynamic systems enables a dynamical system to evolve the states corresponding to nonlinear state equations [33, 72]. Chapter 6 is motivated by the following question:

*Can RNN modeling proper to a dynamical time-variant system effectively compensate for uncertain system parameters in VSCMG system?* To address this motivating question, an adaptive RNN-based attitude controller is developed in Chapter 6 in the presence of uncertain, time-varying satellite inertia properties, actuator uncertainties, and nonlinear external disturbances.

The singularity avoidance methods used in Chapters 4 and 6 maintain torque amplification while avoiding singularities. However, to more properly react to singularity corresponding to characteristics of each singularity, it is essential to understand singularity and detect a specific type of singularity. To overcome long-standing singularity issues which have remained problematic since Margulies and Aubrun [70] established a theory to investigate CMG singularity, various CMG configurations and steering laws have been proposed [4, 14, 17, 20, 34, 53, 54, 78, 94, 103, 104]. CMG configurations can be mainly classified into roof type arrangement and pyramidal arrangement. The roof type configuration is able to avoid all internal singularity using 6 CMG units but inefficient since the radius of workspace (i.e., total angular momentum envelope) is small in spite of the redundancy of CMG units [54, 56, 57]. On the other hand, the pyramidal configuration has larger workspace than the roof type but elliptic singularity which can be escaped only by changing the magnitude of angular momentum makes it difficult to actively utilize this configuration. Hence, if a steering method for the pyramidal configuration can escape internal singularities, various missions will be able to effectively utilize CMG actuators. To resolve singularity problems has introduced a variety of steering methods. Global avoidance methods including path planning [78], preferred gimbal angle [94], and workspace restriction [53, 54] can steer a set of gimbal angles based on a priori knowledge of the singular states but such off-line calculation limits the workspace of CMG arrays [53, 54, 78, 94]. Gradient methods for which a null motion is determined to increase or decrease distance to singular states are not effective due to elliptic internal singularities [14, 34, 103]. Steering laws that allow torque errors (i.e., a singularity robust

methods) avoid singularities but sacrifices precise attitude control [6, 27, 70, 74, 97]. A hybrid steering logic for SGCMG recently developed by [64] simultaneously utilizes null motion and torque errors to cope with a specific type of singularity.

For a VSCMG system, a combination of a SGCMG system and a RW system can be geometrically considered as a singularity-free device. To utilize the torque amplification property of CMG, the singularity avoidance of the CMG system is still essential for the VSCMG system [87, 101]. Further, when the specific type of singularity is distinguished online, the CMG system can achieve precise attitude tracking performance [64]. If the specific type of singularity can be determined, the VSCMG can acquire more effective performance since the VSCMG can make the best use of the torque amplification in CMG mode and also utilize the wheel null motions (e.g., start-up, power reduction, etc.) while properly responding to each type of singularity while maintaining holding precise attitude control. Using singularity metric and the FLS classifier in Chapter 7, all of the singular surfaces inside the angular momentum envelope can be classified and escaped/avoided online.

## 1.2 Contributions

This dissertation focuses on developing a variety of multi-functional intelligent control laws for VSCMG-actuated satellites in the presence of uncertain satellite inertia, uncertain actuator inertia, and uncertain dynamic and static friction, and further a new singularity detection method for a VSCMG-actuated satellite. Using novel control laws, this research achieves attitude stabilization as well as energy storage, initial start-up, and power reduction in the presence of friction. The contributions of Chapters 3-7 are as follows.

Chapter 3, *Precision IPACS in the Presence of Dynamic Uncertainty*: The contribution of this work is the development of an IPACS for VSCMG-actuated satellites in the presence of uncertain dynamic and static friction in the VSCMG gimbals and wheels so that the controller is capable of achieving attitude tracking while simultaneously tracking a desired power profile asymptotically. In addition, the controller compensates for the

effects of uncertain, time-varying satellite inertia properties. The wheel null motions resulting from the extended DOF of VSCMGs allow the VSCMG system to accomplish a novel combined objective as precision attitude tracking and power storage (i.e., mechanical battery). The developed controller includes the uncertain dynamics of the gimbals and flywheels in the control design for improved robustness to these disturbances. The difficulties arising from dynamic friction and uncertain satellite inertia are mitigated through strategic manipulation of the closed-loop derived from a Lyapunov-based analysis. In the presence of static friction, the control design is complicated due to the control input being embedded in a discontinuous nonlinearity. This difficulty is overcome with the use of a robust control element.

Chapter 4, *Integrated Power Reduction and Adaptive Attitude Control System of a Satellite*: The contribution of this work is the development of coupled dynamics of the satellite, gimbals, and wheels including static and dynamic friction on gimbal and wheel bearings. When scaling the size of CMGs/VSCMGs, the effects of friction present in the system are significant (i.e., due to less efficient bearings and motors and the lack of available hardware components). In the presence of uncertain dynamic and static frictions in both the gimbals and the flywheels, the controller is developed by using a Lyapunov-based backstepping technique. The system is capable of achieving global asymptotic attitude tracking while simultaneously performing singularity avoidance and wheel deceleration by the null motion. In the wheel despinning mode, the wheel friction torque is beneficial for the total applied torques of the wheels. Since the wheel friction provides additional torques for the wheel dynamics, the despinning wheels contribute to power reduction without an additional torque request. Power reduction results from the wheel deceleration mode and yields both torque and power reduction. Also, the applied control torque can responsively compensate for uncertain parameters allowing the system to maintain consistent performance in the presence of dynamic uncertainty.

Chapter 5, *A New Initial Start-up Method Using Momentum Management of VSCMGs*: The contribution of this work is the development of an adaptive attitude controller for a VSCMG-actuated satellite which achieves initial start-up and initial attitude stabilization in the normal transition from SHM to initial attitude acquisition mode. Previous space missions using CMGs have used a separate feedback control loop to spin up the rotor to the required spin rate and maintain it while securing attitude stabilization using additional devices such as magnetorquers. In this chapter, the VSCMG steering law including the internal momentum management allows the flywheel to start from rest and to reach the desired speed. In the presence of satellite inertia uncertainty and actuator uncertainty, the proposed attitude controller is capable of achieving global asymptotic attitude tracking while simultaneously performing singularity avoidance and internal momentum management. The significant benefit of the developed steering law is to condense several discontinuous, separate feedback control steps such as the initial start-up and initial attitude acquisition mode into one continuous and simultaneous control step. The controller also compensates for the effects of uncertain, time-varying satellite inertia properties. The difficulties arising from uncertain satellite inertia are mitigated through a Lyapunov-based stability analysis derived controller.

Chapter 6, *A RNN-based Attitude Control Method for a VSCMG-actuated Satellite*: The contribution of this work is the development of a RNN structure while simultaneously acting as a composite VSCMG steering law which achieves attitude tracking for a VSCMG-actuated satellite in the presence of uncertainty in the satellite and actuator dynamics and unmodeled external disturbances. The internal state of a continuous-time RNN can effectively approximate a dynamical time-variant system. Since the utilization of dynamically driven RNNs can be more efficient for identification and modeling of dynamic plants than one of FNNs, the capability of RNN modeling to evolve the states corresponding to nonlinear state equations is exploited to compensate for actuator uncertainties of

VSCMGs. Simulation results indicate the RNN system properly approximate a nonlinear system within a small residual error. A Lyapunov-based stability analysis is used to prove the controller achieves attitude stabilization while compensating for the effects of uncertain time-varying satellite inertia properties, parametric uncertainty, and nonlinear external disturbance torques.

Chapter 7, *A Singularity Detection method for VSCMGs Using FLS*: Although various endeavor to resolve the long-standing problem caused by CMG singularity has been studied, there have been no CMG steering laws to escape all internal singularities (i.e., elliptic, hyperbolic, and degenerate hyperbolic) while achieving precision attitude control. In this chapter, a FLS-based singularity detection method provides an avenue to answer the troublesome issues. Since FLS copes with complex and nonlinear patterns of singularity, the FLS provides an effective singularity detection strategy. The developed singularity detection and classification method can escape/avoid internal singularities, including the degenerate hyperbolic singularity. This method is the first result that can escape all internal singularities for the pyramidal arrangement. By detecting a specific type of singularity, the VSCMG can acquire more effective performance since the VSCMG can make the best use of the torque amplification in CMG mode and the wheel null motions (e.g., start-up, power reduction, etc.) while properly responding to each type of singularity while maintaining precise attitude control.

## CHAPTER 2 SYSTEM MODEL

### 2.1 Kinematic Model

The rotational kinematics of a satellite modelled as a rigid-body can be expressed as

$$\dot{q}_v = \frac{1}{2} (q_v^\times \omega^S + q_0 \omega^S) \quad (2-1)$$

$$\dot{q}_0 = -\frac{1}{2} q_v^T \omega^S, \quad (2-2)$$

where  $\omega^S(t) \in \mathbb{R}^3$  denotes the satellite angular velocity, and  $q(t) \triangleq \{q_0(t), q_v(t)\} \in \mathbb{R} \times \mathbb{R}^3$  represents the unit quaternion describing the orientation of the satellite body-fixed frame  $\mathcal{F}_S$  with respect to the inertial reference frame  $\mathcal{I}$ , subject to the constraint

$$q_v^T q_v + q_0^2 = 1. \quad (2-3)$$

In (2-1),  $q_v^\times \forall q_v = [q_{v_1}, q_{v_2}, q_{v_3}]^T$  denotes the following skew-symmetric matrix:

$$q_v^\times = \begin{bmatrix} 0 & -q_{v_3} & q_{v_2} \\ q_{v_3} & 0 & -q_{v_1} \\ -q_{v_2} & q_{v_1} & 0 \end{bmatrix}.$$

Rotation matrices that bring  $\mathcal{I}$  onto  $\mathcal{F}_S$  and  $\mathcal{I}$  onto the desired body-fixed orientation  $\mathcal{F}_{S_d}$  are denoted by  $R(q_0, q_v) \in SO(3)$  and  $R_d(q_{0d}, q_{vd}) \in SO(3)$ , respectively, are defined as

$$R \triangleq (q_0^2 - q_v^T q_v) I_3 + 2q_v q_v^T - 2q_0 q_v^\times \quad (2-4)$$

$$R_d \triangleq (q_{0d}^2 - q_{vd}^T q_{vd}) I_3 + 2q_{vd} q_{vd}^T - 2q_{0d} q_{vd}^\times, \quad (2-5)$$

where  $I_3$  denotes the  $3 \times 3$  identity matrix, and  $q_d(t) \triangleq \{q_{0d}(t), q_{vd}(t)\} \in \mathbb{R} \times \mathbb{R}^3$  represents the desired unit quaternion that describes the orientation of  $\mathcal{F}_{S_d}$  with respect to  $\mathcal{I}$ .

### 2.2 VSCMG-actuated Satellite Model

The total angular momentum  $h_{C_s}^S(\omega^B, \omega^S, \dot{\delta}, \Omega) \in \mathbb{R}^3$  for a VSCMG-actuated satellite consisting of a bus (i.e., an infrastructure of a satellite, usually providing locations for the

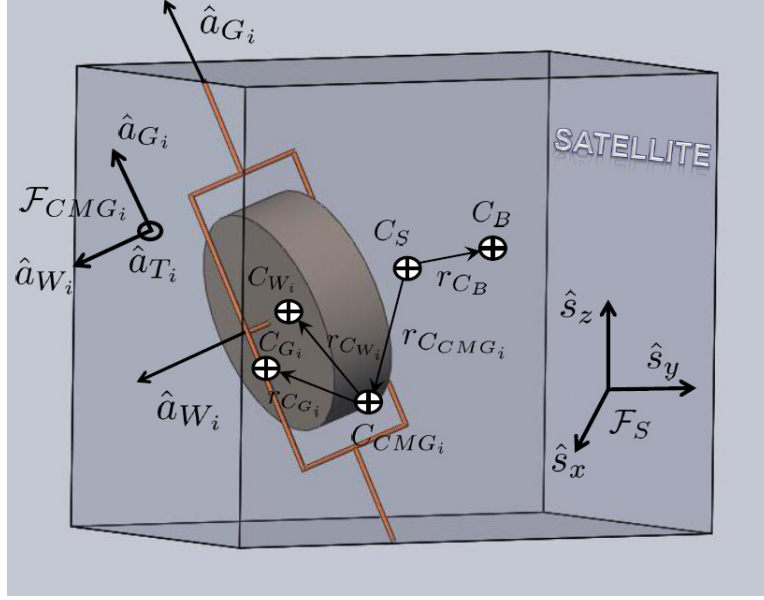


Figure 2-1. Geometry of satellite with  $i^{th}$  VSCMG.

payload) and four VSCMGs can be expressed as

$$h_{C_s}^S = J_{C_s}^B \omega^B + \sum_{i=1}^4 I_{C_s}^{CMG_i} \omega^S + \sum_{i=1}^4 h_{C_{CMG_i}}^{CMG_i/S}, \quad (2-6)$$

where sub- and superscript of each notation indicate a point of interest and a body, respectively,  $\omega^B(t), \omega^S(t) \in \mathbb{R}^3$  denote the angular velocities of the bus and the satellite,  $\delta(t), \dot{\delta}(t), \Omega(t) \in \mathbb{R}^4$  are the gimbal angle, gimbal rate, and flywheel speed, respectively.

The geometry of the dynamic model is shown in Figures 2-1 and 2-2. In (2-6),  $J_{C_s}^B(\delta) \in \mathbb{R}^{3 \times 3}$  is the moment of inertia matrix of the bus relative to the center of mass (C.M.) of the satellite ( $C_S$ ) and  $I_{C_s}^{CMG_i}(\delta) \in \mathbb{R}^{3 \times 3}$  is the  $i^{th}$  CMG unit's inertia matrix relative to  $C_S$  given by

$$\begin{aligned} J_{C_s}^B &= J_{C_B}^B + m_B [(r_{C_B}^T r_{C_B}) I_3 - r_{C_B} r_{C_B}^T], \\ I_{C_s}^{CMG_i} &= D_{CMG_i}^{CMG} I_{C_{CMG_i}}^{CMG_i} D_{CMG_i}^T + m_{CMG_i} [(r_{C_{CMG_i}}^T r_{C_{CMG_i}}) I_3 - r_{C_{CMG_i}} r_{C_{CMG_i}}^T], \end{aligned} \quad (2-7)$$

where  $J_{C_B}^B \in \mathbb{R}^{3 \times 3}$  is the moment of inertia matrix of the bus relative to the C.M. of the bus ( $C_B$ ),  $m_B \in \mathbb{R}$  is the mass of the bus,  $r_{C_B} \in \mathbb{R}^3$  is the position of  $C_B$  relative to  $C_S$ ,  $^{CMG} I_{C_{CMG_i}}^{CMG_i} \in \mathbb{R}^{3 \times 3}$  is expressed in the CMG-fixed frame  $\mathcal{F}_{CMG_i}$  and the moment of

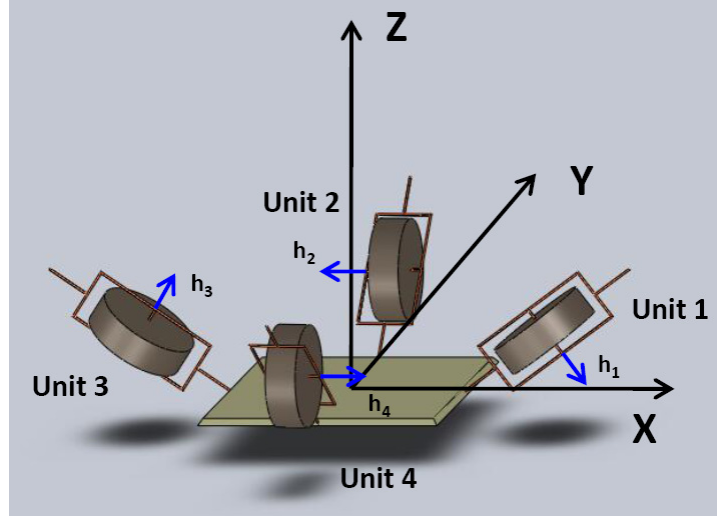


Figure 2-2. Pyramidal arrangement of 4 VSCMGs system.

inertia matrix of the  $i^{th}$  CMG relative to the C.M. of the  $i^{th}$  CMG ( $C_{CMG_i}$ ),  $m_{CMG_i} \in \mathbb{R}$  is the mass of the  $i^{th}$  CMG,  $r_{C_{CMG_i}} \in \mathbb{R}^3$  is the position of  $C_{CMG_i}$  relative to  $C_S$ , and  $D_{CMG_i}(\delta) \in \mathbb{R}^{3 \times 3}$  is the direction cosine matrix (DCM) which transforms  $\mathcal{F}_{CMG_i}$  to  $\mathcal{F}_S$ . Specifically, the moment of inertia matrix of  $i^{th}$  CMG expressed in  $\mathcal{F}_{CMG_i}$  is defined as

$${}^{CMG_i}I_{C_{CMG_i}}^{CMG_i} \triangleq I_{C_{CMG}}^{G_i} + m_{G_i} \left[ \left( r_{C_{G_i}}^T r_{C_{G_i}} \right) I_3 - r_{C_{G_i}} r_{C_{G_i}}^T \right] \\ + I_{C_{CMG}}^{W_i} + m_{W_i} \left[ \left( r_{C_{W_i}}^T r_{C_{W_i}} \right) I_3 - r_{C_{W_i}} r_{C_{W_i}}^T \right],$$

where  $I_{C_{CMG}}^{G_i}, I_{C_{CMG}}^{W_i} \in \mathbb{R}^{3 \times 3}$  are the moments of inertia matrix of each gimbal and wheel relative to  $C_{CMG_i}$ ;  $m_{G_i}, m_{W_i} \in \mathbb{R}$  are the masses of  $i^{th}$  gimbal and wheel;  $r_{C_{G_i}}, r_{C_{W_i}} \in \mathbb{R}^3$  are the positions to the respective C.M. of the  $i^{th}$  gimbal and of the  $i^{th}$  wheel from  $C_{CMG_i}$ . Also in (2-6),  $h_{C_{CMG_i}}^{CMG_i/S}(\dot{\delta}, \Omega) \in \mathbb{R}^3$  represents the angular momentum contributions from the flywheel and the gimbal and is given by

$$h_{C_{CMG_i}}^{CMG_i/S} = {}^{CMG_i}I_{C_{CMG_i}}^{CMG_i} \dot{\delta}_i \hat{a}_{G_i} + {}^{CMG_i}I_{C_{CMG_i}}^{CMG_i} \Omega_i \hat{a}_{W_i},$$

where the angular momentum of the CMG is expressed in terms of a CMG-fixed basis  $\mathcal{B} = \left\{ \hat{a}_{G_i}, \hat{a}_{W_i}, \hat{a}_{T_i} \right\}$ ;  $\hat{a}_{G_i}$  is a gimbal axis,  $\hat{a}_{W_i}$  is a spinning wheel axis, and  $\hat{a}_{T_i}$  is a transverse axis. Assuming that  ${}^{CMG_i}I_{C_{CMG_i}}^{CMG_i}$  is a principal inertia matrix, the CMG

inertia matrix can be defined as  ${}^{CMG_i}I_{CMG_i}^{CMG_i} = \text{diag} \left( \begin{bmatrix} I_{G_i}^{CMG_i} & I_{W_i} & I_{T_i}^{CMG_i} \end{bmatrix} \right)$  since  ${}^{CMG_i}I_{CMG_i}^{CMG_i} \hat{a}_{W_i} = I_{W_i} \hat{a}_{W_i}$ . In addition,  $\omega(t) = \omega^S(t) \equiv \omega^B(t)$  in (2-6) under the assumption of a rigid body satellite, where  $\omega(t)$  is expressed in  $\mathcal{F}_S$ . Using the principal inertia of the CMG system and the rigid body assumption, the total angular momentum of the satellite can be rewritten as

$$\begin{aligned} h_{C_s}^S &= \sum_{i=1}^4 \left[ (J_{C_s}^B + I_{C_s}^{CMG_i}) \omega + h_{CMG_i/S}^{CMG_i} \right] \\ &= J_{C_s}^S \omega + \sum_{i=1}^4 \left( I_{G_i}^{CMG_i} \dot{\delta}_i \hat{a}_{G_i} + I_{W_i} \Omega_i \hat{a}_{W_i} \right), \end{aligned} \quad (2-8)$$

where  $J_{C_s}^S(\delta) \omega(t) = (J_{C_s}^B + \sum_{i=1}^4 I_{C_s}^{CMG_i}(\delta)) \omega(t)$ . The inertial derivative of the total angular momentum  $h_{C_s}^S(\omega, \dot{\delta}, \Omega)$  is expressed as

$$\begin{aligned} \dot{h}_{C_s}^S &= \frac{d}{dt} (J_{C_s}^S) \omega + J_{C_s}^S \dot{\omega} + \omega \times J_{C_s}^S \omega \\ &\quad + \sum_{i=1}^4 \left[ I_{G_i}^{CMG_i} \ddot{\delta}_i \hat{a}_{G_i} + I_{W_i} \dot{\Omega}_i \hat{a}_{W_i} + I_{G_i}^{CMG_i} \dot{\delta}_i \hat{a}_{G_i} + I_{W_i} \Omega_i \dot{\hat{a}}_{W_i} \right]. \end{aligned} \quad (2-9)$$

Expressing  $\omega(t)$  in  $\mathcal{F}_{CMG_i}$  which is given by the  $i^{\text{th}}$  CMG-fixed basis  $\mathcal{B}$ , the satellite angular velocity  $\omega(t)$  can be written as

$$\begin{aligned} {}^{CMG_i} \omega &= D_{CMG_i}^T \omega = \begin{bmatrix} \hat{a}_{G_i}^T & \hat{a}_{W_i}^T & \hat{a}_{T_i}^T \end{bmatrix} \omega, \\ &= \omega_{G_i} \hat{a}_{G_i} + \omega_{W_i} \hat{a}_{W_i} + \omega_{T_i} \hat{a}_{T_i}, \end{aligned} \quad (2-10)$$

where  $\omega_{G_i}(t) = \hat{a}_{G_i}^T \omega(t)$ ,  $\omega_{W_i}(t) = \hat{a}_{W_i}^T \omega(t)$ , and  $\omega_{T_i}(t) = \hat{a}_{T_i}^T \omega(t)$ . The inertial derivatives of  $\mathcal{B}$  in (2-9) are

$$\begin{aligned} \dot{\hat{a}}_{G_i} &= \omega_{T_i} \hat{a}_{W_i} - \omega_{W_i} \hat{a}_{T_i} \\ \dot{\hat{a}}_{W_i} &= -\omega_{T_i} \hat{a}_{G_i} + (\dot{\delta} + \omega_{G_i}) \hat{a}_{T_i} \\ \dot{\hat{a}}_{T_i} &= \omega_{W_i} \hat{a}_{G_i} - (\dot{\delta} + \omega_{G_i}) \hat{a}_{W_i}. \end{aligned} \quad (2-11)$$

Substituting (2-11) into (2-9) and performing some algebraic manipulations, the inertial derivative of the total angular momentum can be represented as

$$\begin{aligned}
\dot{h}_{C_s}^S &= \frac{d}{dt} (J_{C_s}^S) \omega + J_{C_s}^S \dot{\omega} + \omega^\times J_{C_s}^S \omega \\
&+ \sum_{i=1}^4 \left( I_{G_i}^{CMG_i} \ddot{\delta}_i - I_{W_i} \Omega_i \omega_{T_i} \right) \hat{a}_{G_i} \\
&+ \sum_{i=1}^4 \left( I_{W_i} \dot{\Omega}_i + I_{G_i}^{CMG_i} \dot{\delta}_i \omega_{T_i} \right) \hat{a}_{W_i} \\
&+ \sum_{i=1}^4 \left\{ I_{W_i} \Omega_i \left( \dot{\delta}_i + \omega_{G_i} \right) - I_{G_i}^{CMG_i} \dot{\delta}_i \omega_{W_i} \right\} \hat{a}_{T_i},
\end{aligned} \tag{2-12}$$

where  $\frac{d}{dt} (J_{C_s}^S (\delta)) = \sum_{i=1}^4 \frac{\partial}{\partial \delta_i} (J_{C_s}^S (\delta)) \dot{\delta}_i (t)$  since the direction cosine matrix  $D_{CMG_i} (\delta)$  constructing the total satellite inertia  $J_{C_s}^S (\delta)$  depends on  $\delta_i (t)$ . Hence, the kinetic equation governing the motion of a rigid satellite following Euler's equation yields

$$\dot{h}_{C_s}^S = g_{C_s}^E, \tag{2-13}$$

where  $g_{C_s}^E (\omega, \dot{\omega}, \delta, \dot{\delta}, \ddot{\delta}, \Omega, \dot{\Omega}) \in \mathbb{R}^3$  is the external torque applied to the satellite. Using (2-12) and (2-13), the equation of motion for a rigid VSCMG-actuated satellite can be written as

$$\begin{aligned}
g_{C_s}^E &= \dot{J} \omega + J \dot{\omega} + \omega^\times J \omega \\
&+ C_G \left( [I_G^{CMG}]^d \ddot{\delta} - [I_W]^d [\omega_T]^d \Omega \right) \\
&+ C_W \left( [I_W]^d \dot{\Omega} + [I_G^{CMG}]^d [\omega_T]^d \dot{\delta} \right) \\
&+ C_T \left( [I_W]^d [\Omega]^d \dot{\delta} + [I_W]^d [\omega_G]^d \Omega - [I_G^{CMG}]^d [\omega_W]^d \dot{\delta} \right),
\end{aligned} \tag{2-14}$$

where the uncertain total satellite inertia matrix  $J_{C_s}^S (\delta)$ , henceforth denoted by  $J (\delta)$  for simplicity, is positive definite and symmetric such that

$$\frac{1}{2} \lambda_{\min} \{J\} \|\xi\|^2 \leq \xi^T J \xi \leq \frac{1}{2} \lambda_{\max} \{J\} \|\xi\|^2 \quad \forall \xi \in \mathbb{R}^n \tag{2-15}$$

where  $\lambda_{\min} \{J\}$ ,  $\lambda_{\max} \{J\} \in \mathbb{R}$  are the minimum and maximum principal inertias of  $J(\delta)$ , respectively. In (2-14),  $C_G, C_W(\delta), C_T(\delta) \in \mathbb{R}^{3 \times 4}$  for the CMG-fixed axes ( $\hat{a}_{G_i}, \hat{a}_{W_i}, \hat{a}_{T_i}$ ) are defined as

$$\begin{aligned}
C_G &\triangleq \begin{bmatrix} \hat{a}_{G_1} & \hat{a}_{G_2} & \hat{a}_{G_3} & \hat{a}_{G_4} \end{bmatrix} = \begin{bmatrix} \sin\beta & 0 & -\sin\beta & 0 \\ 0 & \sin\beta & 0 & -\sin\beta \\ \cos\beta & \cos\beta & \cos\beta & \cos\beta \end{bmatrix}, \\
C_W &\triangleq \begin{bmatrix} \hat{a}_{W_1} & \hat{a}_{W_2} & \hat{a}_{W_3} & \hat{a}_{W_4} \end{bmatrix} = \begin{bmatrix} -\cos\beta\sin\delta_1 & -\cos\delta_2 & \cos\beta\sin\delta_3 & \cos\delta_4 \\ \cos\delta_1 & -\sin\delta_2\cos\beta & -\cos\delta_3 & \cos\beta\sin\delta_4 \\ \sin\beta\sin\delta_1 & \sin\beta\sin\delta_2 & \sin\beta\sin\delta_3 & \sin\beta\sin\delta_4 \end{bmatrix}, \\
C_T &\triangleq \begin{bmatrix} \hat{a}_{T_1} & \hat{a}_{T_2} & \hat{a}_{T_3} & \hat{a}_{T_4} \end{bmatrix} = \begin{bmatrix} -\cos\beta\cos\delta_1 & \sin\delta_2 & \cos\beta\cos\delta_3 & -\sin\delta_4 \\ -\sin\delta_1 & -\cos\delta_2\cos\beta & \sin\delta_3 & \cos\beta\cos\delta_4 \\ \sin\beta\cos\delta_1 & \sin\beta\cos\delta_2 & \sin\beta\cos\delta_3 & \sin\beta\cos\delta_4 \end{bmatrix},
\end{aligned}$$

where  $\beta$  is a skew angle for the pyramidal arrangement of four VSCMGs, and the inertia matrices  $[I_G^{CMG}]^d, [I_W]^d \in \mathbb{R}^{4 \times 4}$  are

$$\begin{aligned}
[I_G^{CMG}]^d &\triangleq \text{diag} \left( \begin{bmatrix} I_G^{CMG_1} & I_G^{CMG_2} & I_G^{CMG_3} & I_G^{CMG_4} \end{bmatrix} \right), \\
[I_W]^d &\triangleq \text{diag} \left( \begin{bmatrix} I_{W_1} & I_{W_2} & I_{W_3} & I_{W_4} \end{bmatrix} \right),
\end{aligned}$$

where  $[I_G^{CMG}]^d$  is the unknown constant positive-definite, symmetric about its gimbal axis, gimbal inertia matrix but  $[I_W]^d$  is the known constant positive-definite, symmetric about its spin axis, flywheel inertia matrix, and the angular velocity projected to  $\mathcal{B}$  is denoted as  $[\omega_\circ(t)]^d \triangleq \text{diag} \left( \begin{bmatrix} \omega_{\circ_1}(t) & \omega_{\circ_2}(t) & \omega_{\circ_3}(t) & \omega_{\circ_4}(t) \end{bmatrix} \right)$  ( $\circ : G, W, T$ )  $\in \mathbb{R}^{4 \times 4}$ , and  $[\Omega(t)]^d$  and  $[\dot{\delta}(t)]^d$  denote diagonal matrices composed of the vector elements of measurable  $\Omega(t)$ ,  $\dot{\delta}(t) \in \mathbb{R}^4$ , respectively.

### 2.3 Singularities

A VSCMGs system is a geometrically singularity free device since it can generate control torques along an arbitrary direction. The extra DOF resulting from a variable

wheel speed (i.e., RW mode) does not allow the VSCMG to encounter a singularity. However, to make the best use of torque amplification which is a significant advantage of operating in a CMG mode, it is important to investigate singularities of the CMGs since the existence of singular states is an obstacle to generate a torque along arbitrary directions.

### 2.3.1 What is a singularity?

The term Singularity has various definitions. In the dictionary, a singularity is generally defined as the state of being singular, distinct, peculiar, uncommon or unusual. In physics, a singularity is defined as a point or region in which the quantities (e.g., gravitational force) that are used to measure the gravitational field become infinite (i.e., the point is associated with black holes). In mathematics, a singularity is the value or range of values of a function for which a derivative does not exist, and the term Singular matrix is defined as a square matrix that does not have a matrix inverse (i.e., A matrix is singular iff its determinant is 0). Of particular interest in this dissertation, however, is the definition of Singularity in a workspace or angular momentum envelope of CMGs.

### 2.3.2 Singularity of CMGs

Singularity of CMGs is defined as the case where the mapping from an input to an output space (a nonlinear, vector-valued mapping  $H(\delta) : \mathbb{R}^n \rightarrow \mathbb{R}^3$ ) is not locally onto, or equivalently a matrix does not have a full rank (i.e.,  $\text{rank}(C_T) < 3$ ), where  $\delta(t) \in \mathbb{R}^4$  is the gimbal angle vector and  $C_T(\delta)$  is a CMG Jacobian matrix. At singular states, in the three-dimensional workspace the CMGs are unable to produce a torque along an arbitrary singular direction since all admissible torque directions lie on a two-dimensional surface perpendicular to the singular direction. The specific arrangement of the gimbals affects the type and number of singularities. The CMG singularities can be classified according to the location of the total momentum vector relative to the workspace: external/saturation singularity and internal singularity.

For analyzing the singular momentum surfaces [70, 96], an arbitrary vector  $u$  is represented in terms of a satellite-fixed basis  $\mathcal{S} \triangleq \{\hat{s}_x, \hat{s}_y, \hat{s}_z\}$  as

$$u = u_x \hat{s}_x + u_y \hat{s}_y + u_z \hat{s}_z,$$

and defined as

$$U = \{u : |u| = 1, u \neq \pm \hat{a}_{G_i}, i = 1, \dots, n\},$$

where  $u = \pm \hat{a}_{G_i}$  only happens in a special configuration such as DGCMGs system or a roof-type configuration. A condition for which the CMG arrangement cannot generate any torques along the singular direction  $u$  is defined as

$$\hat{a}_{T_i} \cdot u = 0, \quad (2-16)$$

where all  $\hat{a}_{T_i}$  become coplanar (i.e.,  $\text{rank}(C_T) = 2$ ), and an arbitrary vector  $u$  is perpendicular to that plane. In the CMG-fixed frame  $\mathcal{F}_{CMG_i}$  as shown in Figure 2-1,  $\hat{a}_{G_i}$  and  $u$  spans a plane normal to  $\hat{a}_{T_i}$ , and  $\hat{a}_{W_i}$  has a maximal or minimal projection onto the singularity vector  $u$  (i.e.,  $\hat{a}_{W_i} \cdot u > 0$  or  $\hat{a}_{W_i} \cdot u < 0$ ). The singularity condition of (2-16) can be rewritten as

$$\begin{aligned} \hat{a}_{T_i} &= \epsilon_i \frac{\hat{a}_{G_i} \times u}{|\hat{a}_{G_i} \times u|}, \\ \hat{a}_{W_i} &= \hat{a}_{T_i} \times \hat{a}_{G_i} = \epsilon_i \frac{(\hat{a}_{G_i} \times u) \times \hat{a}_{G_i}}{|\hat{a}_{G_i} \times u|}, i = 1, \dots, n, \end{aligned}$$

where  $\epsilon_i \triangleq \text{sign}(\hat{a}_{W_i} \cdot u)$ . Hence, the singular momentum vector is expressed as [54, 70, 96]

$$H(u) = \sum_{i=1}^n \hat{a}_{W_i} = \sum_{i=1}^n \epsilon_i \frac{(\hat{a}_{G_i} \times u) \times \hat{a}_{G_i}}{|\hat{a}_{G_i} \times u|}. \quad (2-17)$$

Figure 2-3 shows the total angular momentum envelope considering the singular momentum vector of (2-17) for a pyramidal arrangement with 4 CMG units. The angular momentum envelope in Figure 2-3 includes two types of singularities denoted as external and internal singularities which are smoothly connected.

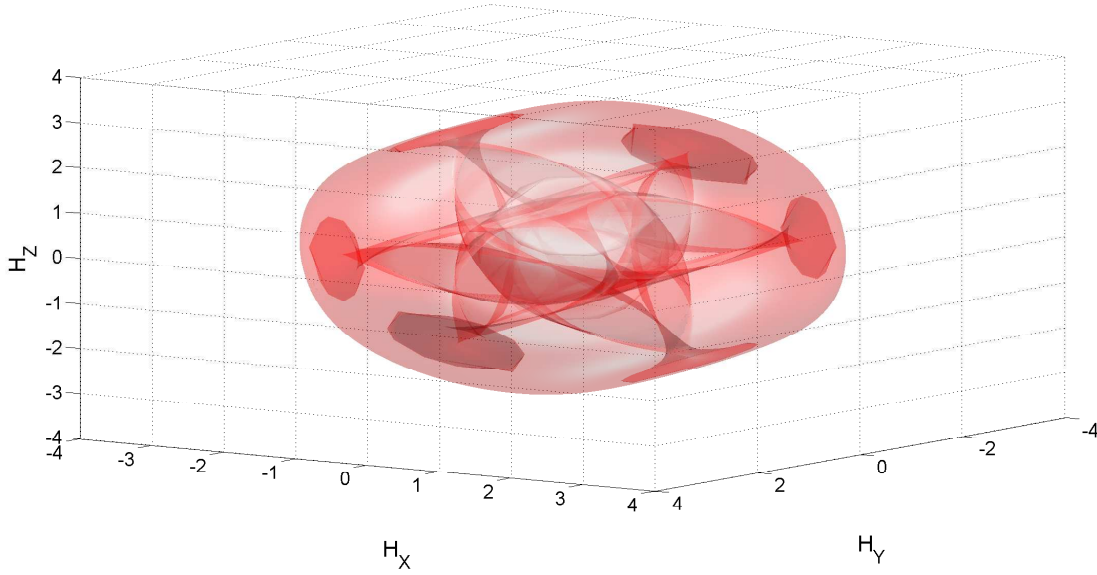


Figure 2-3. Total angular momentum envelope of CMGs

### 2.3.2.1 External singularity

The gimbal angles for which the total angular momentum reaches the envelope of Figure 2-3 become singular since the CMGs are unable to produce a torque outward the envelope. This is because a CMG system changes only the direction but not the magnitude of the angular momentum vector and therefore in external singularity the CMG system experiences a maximum workspace and does not have additional angular momentum for the singular direction. In other words, external/saturation singularities are associated with the maximum projection of the total angular momentum along a certain direction. The criteria for this type of singularity can be expressed as

$$\text{rank}(C_T) < 3, \hat{a}_{w_i} \cdot u > 0 \quad \forall i = 1, 2, 3, 4.$$

External singularities can be addressed in the design process since they can be easily predicted from sizing of the CMG actuators and mission profile.

### 2.3.2.2 Internal singularity

Internal singularity is defined as a case where the total angular momentum vector for any singular state is inside the angular momentum envelope as shown by Figure 2-3.

The internal singularity occurs at a specific combination of gimbal angles which makes the CMG Jacobian singular and at this singularity the torque vectors lie on the same plane perpendicular to the singular direction vector. Internal singularities can be classified according to the possibility of the null motion into two types: elliptic singularity and hyperbolic singularity. The null motion is defined as a motion that changes gimbal angles without producing any torque. Using null motion, the CMG system can be reconfigured in a continuous manner so that the CMG Jacobian becomes nonsingular. The singularity that can be escaped by null motion is termed hyperbolic singularity. However, the case where a set of gimbal angles for the angular momentum envelope has an isolated point is termed elliptic singularity. Elliptic singularities cannot be escaped by null motion. A test for possibility of null motion is specifically discussed in Chapter 7. Although null motion is possible at hyperbolic singularity, the mere existence of null motion does not guarantee escape from the hyperbolic singularity. There are degenerate solutions which do not affect the rank of the CMG Jacobian. This means that the degenerate hyperbolic singularities cannot be escaped through null motion [5, 6, 55, 64, 96]. A singularity detection strategy which can handle all internal singularities is introduced in Chapter 7.

CHAPTER 3  
PRECISION IPACS IN THE PRESENCE OF DYNAMIC UNCERTAINTY

In this chapter, an adaptive robust attitude controller is developed, which compensates for uncertain, time-varying inertia and unknown friction in the VSCMG gimbals and wheels while simultaneously providing asymptotic power tracking. The inclusion of friction effects in the VSCMG gimbals and wheels creates significant complications in the control development. The dynamic friction effects manifest themselves as non-square, time-varying, input-multiplicative uncertainty in the tracking error dynamics. The static friction effects in the dynamic model result in the gimbal angular rate control input being embedded inside of a discontinuous nonlinearity (i.e., the standard signum function). A robust control method is used to mitigate the disturbance resulting from the static friction, and an adaptive control law is used to compensate for the dynamic friction and inertia uncertainties. Lyapunov-based stability analyses are provided, which prove attitude tracking and power tracking in the presence of the aforementioned VSCMG anomalies and satellite inertia uncertainty. Numerical simulations are provided to illustrate the performance of the controllers for simultaneous attitude control and energy storage.

### 3.1 Dynamic Model for IPACS in the Presence of Dynamic Uncertainty

The dynamic model in (2-14) can be expressed for IPACS considering friction as

$$\begin{aligned}
 T = & \dot{J}\omega + J\dot{\omega} + \omega \times J\omega \\
 & + C_G \left( [I_G^{CMG}]^d \ddot{\delta} - [I_W]^d [\omega_T]^d \Omega \right) \\
 & + C_W \left( [I_W]^d \dot{\Omega} + [I_G^{CMG}]^d [\omega_T]^d \dot{\delta} \right) \\
 & + C_T \left( [I_W]^d [\Omega]^d \dot{\delta} + [I_W]^d [\omega_G]^d \Omega - [I_G^{CMG}]^d [\omega_W]^d \dot{\delta} \right).
 \end{aligned} \tag{3-1}$$

In (3-1),  $\tau_f(t) \in \mathbb{R}^4$  denotes the torque generated by the flywheels and the torque vector  $T(\delta, \dot{\delta}, \Omega) \in \mathbb{R}^3$  in (3-1) is defined as

$$T = -C_T \left( F_{dg} \dot{\delta} + F_{sg} \operatorname{sgn}(\dot{\delta}) \right) - C_W (F_{dw} \Omega + F_{sw} \operatorname{sgn}(\Omega)). \tag{3-2}$$

In (3-2),  $F_{dg}, F_{sg} \in \mathbb{R}^{4 \times 4}$  and  $F_{dw}, F_{sw} \in \mathbb{R}^{4 \times 4}$  are diagonal matrices containing the uncertain dynamic and static friction coefficients for the gimbals and wheels, respectively, and  $\text{sgn}(\dot{\delta}(t)) \in \mathbb{R}^4$  denotes a vector form of the standard  $\text{sgn}(\cdot)$  function where the  $\text{sgn}(\cdot)$  is applied to each element of  $\dot{\delta}(t)$ .

## 3.2 Control Objectives

### 3.2.1 Attitude Control Objective

The attitude control objective is to develop a flywheel acceleration and gimbal rate control law to enable the attitude of  $\mathcal{F}$  to track the attitude of  $\mathcal{F}_d$ . To quantify the objective, an attitude tracking error denoted by  $\tilde{R}(e_v, e_0) \in \mathbb{R}^{3 \times 3}$  is defined that brings  $\mathcal{F}_d$  onto  $\mathcal{F}$  as

$$\tilde{R} \triangleq RR_d^T = (e_0^2 - e_v^T e_v) I_3 + 2e_v e_v^T - 2e_0 e_v^\times, \quad (3-3)$$

where  $R(q_v, q_0)$  and  $R_d(q_{vd}, q_{0d})$  were defined in (2-4) and (2-5), respectively, and the quaternion tracking error  $e(t) \triangleq \{e_0(t), e_v(t)\} \in \mathbb{R} \times \mathbb{R}^3$  is defined as

$$e_0 \triangleq q_0 q_{0d} + q_v^T q_{vd} \quad (3-4)$$

$$e_v \triangleq q_{0d} q_v - q_0 q_{vd} + q_v^\times q_{vd}. \quad (3-5)$$

Based on (3-3), the attitude control objective can be stated as

$$\tilde{R}(e_v(t), e_0(t)) \rightarrow I_3 \quad \text{as} \quad t \rightarrow \infty. \quad (3-6)$$

Based on the tracking error formulation, the angular velocity of  $\mathcal{F}$  with respect to  $\mathcal{F}_d$  expressed in  $\mathcal{F}$ , denoted by  $\tilde{\omega}(t) \in \mathbb{R}^3$ , is defined as

$$\tilde{\omega} \triangleq \omega - \tilde{R}\omega_d. \quad (3-7)$$

From the definitions of the quaternion tracking error variables, the following constraint can be developed [16]:

$$e_v^T e_v + e_0^2 = 1, \quad (3-8)$$

where

$$0 \leq \|e_v(t)\| \leq 1 \quad 0 \leq |e_0(t)| \leq 1, \quad (3-9)$$

where  $\|\cdot\|$  represents the standard Euclidean norm. From (6-7),

$$\|e_v(t)\| \rightarrow 0 \Rightarrow |e_0(t)| \rightarrow 1 \quad (3-10)$$

and hence, (3-3) can be used to conclude that if (3-10) is satisfied, then the control objective in (3-6) will be achieved.

### 3.2.2 Power Tracking Objective

The kinetic energy  $E(t) \in \mathbb{R}$  stored in the flywheels of a VSCMG can be expressed as [24]

$$E(t) = \frac{1}{2} \Omega^T(t) I_W \Omega(t). \quad (3-11)$$

The power tracking control objective is to develop a flywheel acceleration control law to enable the actual VSCMG power to track a desired power profile  $P_d(t) \in \mathbb{R}$  while simultaneously tracking a desired time-varying attitude. The desired power profile can be related to a desired kinetic energy profile  $E_d(t) \in \mathbb{R}$  as

$$E_d(t) = \int_0^t P_d(\sigma) d\sigma, \quad (3-12)$$

where the desired kinetic energy and power profiles are assumed to be bounded. To quantify the energy tracking objective, a kinetic energy tracking error  $\eta_E(t) \in \mathbb{R}$  is defined as

$$\eta_E = E_d - E. \quad (3-13)$$

Based on (3-13), the power tracking control objective can be stated as

$$\eta_E \rightarrow 0 \quad \text{as} \quad t \rightarrow \infty. \quad (3-14)$$

### 3.3 Adaptive IPACS

In this section, an adaptive IPACS is developed that forces a satellite to track a desired attitude trajectory while simultaneously providing asymptotic energy/power tracking. In Section 3.3.1, an adaptive attitude controller is developed for a VSCMG-actuated satellite in the presence of gimbal and wheel friction. In Section 3.3.2, a power management system is developed which operates in tandem with the attitude controller.

#### 3.3.1 Adaptive Attitude Control Development

To facilitate the controller design, an auxiliary signal  $r(t) \in \mathbb{R}^3$  is defined as [24]

$$r \triangleq \omega - \tilde{R}\omega_d + \alpha e_v, \quad (3-15)$$

where  $\alpha \in \mathbb{R}^{3 \times 3}$  is a constant, positive definite, diagonal control gain matrix. After substituting (3-15) into (3-7), the angular velocity tracking error can be expressed as

$$\tilde{\omega} = r - \alpha e_v. \quad (3-16)$$

Motivation for the design of  $r(t)$  is obtained from the subsequent Lyapunov-based stability analysis and the fact that (3-3) - (3-5) can be used to determine the open-loop quaternion tracking error as

$$\dot{e}_v = \frac{1}{2} (e_v^\times + e_0 I_3) \tilde{\omega} \quad \dot{e}_0 = -\frac{1}{2} e_v^T \tilde{\omega}. \quad (3-17)$$

After taking the time derivative of (3-15) and multiplying both sides of the resulting expression by  $J(\delta)$ , the following expression can be obtained:

$$J\dot{r} = J\dot{\omega} + J\omega^\times \tilde{R}\omega_d - J\dot{\tilde{R}}\omega_d + \frac{1}{2} J\alpha (e_v^\times + e_0 I_3) \tilde{\omega}, \quad (3-18)$$

where the fact that

$$\dot{\tilde{R}} = -\omega^\times \tilde{R}$$

was utilized. Under the standard assumption that the gimbal acceleration term  $C_G [I_G^{CMG}]^d \delta \ddot{\delta}(t)$  is negligible [26, 83, 89], (3-1), (3-2), (3-15), and (3-17) can be used to express (3-18) as

$$\begin{aligned} J\dot{r} = & \Upsilon_1 \dot{\delta} + \Upsilon_2 \dot{\Omega} + Y_1 \theta_1 - \frac{1}{2} \dot{J} r \\ & - C_T F_{sg} \operatorname{sgn}(\dot{\delta}) - C_W F_{sw} \operatorname{sgn}(\Omega), \end{aligned} \quad (3-19)$$

where the uncertain matrix  $\Upsilon_1(e_v, e_0, r, \delta, \Omega) \in \mathbb{R}^{3 \times 4}$  is defined via the parameterization

$$\begin{aligned} \Upsilon_1 \dot{\delta} \triangleq & -\frac{\partial J}{\partial \delta} \dot{\delta} \left( \frac{1}{2} r + \tilde{R} \omega_d - \alpha e_v \right) - C_T F_{dg} \dot{\delta} \\ & - C_W [I_G^{CMG}]^d [\omega_T]^d \dot{\delta} - C_T \left( [I_W]^d [\Omega]^d - [I_G^{CMG}]^d [\omega_W]^d \right) \dot{\delta}, \end{aligned} \quad (3-20)$$

and the uncertain matrix  $\Upsilon_2(\delta) \in \mathbb{R}^{3 \times 4}$  is defined as

$$\Upsilon_2 \triangleq -C_W [I_W]^d. \quad (3-21)$$

Also in (3-19),  $Y_1(e_v, e_0, r, \omega, \omega_d, \dot{\omega}_d, \delta, \Omega) \theta_1$  is defined via the parameterization

$$\begin{aligned} Y_1 \theta_1 \triangleq & -C_W F_{dw} \Omega - C_G [I_W]^d [\omega_T]^d \Omega - C_T [I_W]^d [\omega_G]^d \Omega \\ & - \omega^\times J \omega + J \omega^\times \tilde{R} \omega_d - J \tilde{R} \dot{\omega}_d + \frac{1}{2} J \alpha (e_v^\times + e_0 I) \tilde{\omega}. \end{aligned} \quad (3-22)$$

In (3-22),  $Y_1(\cdot) \in \mathbb{R}^{3 \times p_1}$  is a measurable regression matrix, and  $\theta_1 \in \mathbb{R}^{p_1}$  is a vector of unknown constants. In (3-19), the auxiliary matrices  $\Upsilon_1(\cdot)$  and  $\Upsilon_2(\cdot)$  contain only linearly parameterizable uncertainty, so the terms are grouped as

$$\Upsilon_1 \dot{\delta} + \Upsilon_2 \dot{\Omega} \triangleq Y_2 \theta_2, \quad (3-23)$$

where  $Y_2(e_v, e_0, r, \omega, \omega_d, \delta, \dot{\delta}, \Omega, \dot{\Omega}) \in \mathbb{R}^{3 \times p_2}$  is a measurable regression matrix, and  $\theta_2 \in \mathbb{R}^{p_2}$  is a vector of unknown constants. Some of the control design challenges for the open-loop system in (3-19) are that the control input  $\dot{\delta}(t)$  is premultiplied by a non-square, unknown time-varying matrix  $\Upsilon_1(\cdot)$ , and the gimbal rate control input  $\dot{\delta}(t)$  is embedded inside of a discontinuous nonlinearity (i.e.,  $C_T F_{sg} \operatorname{sgn}(\dot{\delta})$ ). To address the fact that the control input is premultiplied by a non-square, unknown time-varying matrix, estimates of the

uncertainty in (3-23), denoted by  $\hat{\Upsilon}_1(t) \in \mathbb{R}^{3 \times 4}$  and  $\hat{\Upsilon}_2(t) \in \mathbb{R}^{3 \times 4}$ , are defined as

$$\hat{\Upsilon}_1 \dot{\delta} + \hat{\Upsilon}_2 \dot{\Omega} \triangleq Y_2 \hat{\theta}_2, \quad (3-24)$$

where  $\hat{\theta}_2(t) \in \mathbb{R}^{p_2}$  is a subsequently designed estimate for the parametric uncertainty in  $\Upsilon_1(\cdot)$  and  $\Upsilon_2(\cdot)$ . Based on (3-23) and (3-24), (3-19) can be rewritten as

$$\begin{aligned} Jr &= \hat{\Upsilon}_1 \dot{\delta} + \hat{\Upsilon}_2 \dot{\Omega} + Y_1 \theta_1 + Y_2 \tilde{\theta}_2 - \frac{1}{2} Jr \\ &\quad - C_T F_{sg} \operatorname{sgn}(\dot{\delta}) - C_W F_{sw} \operatorname{sgn}(\Omega), \end{aligned} \quad (3-25)$$

where the notation  $\tilde{\theta}_2(t) \in \mathbb{R}^{p_2}$  is defined as

$$\tilde{\theta}_2 = \theta_2 - \hat{\theta}_2. \quad (3-26)$$

Based on the expression in (3-25) and the subsequent stability analysis, the flywheel acceleration control input is designed as

$$\dot{\Omega} = -\hat{\Upsilon}_2^+ u_c - \left( I_4 - \hat{\Upsilon}_2^+ \hat{\Upsilon}_2 \right) g, \quad (3-27)$$

where  $g(t)$  is an auxiliary control signal designed to achieve the subsequent power tracking objective [24]. In (3-27), the auxiliary control input  $u_c(t)$  is designed as

$$u_c = Y_1 \hat{\theta}_1 + e_v, \quad (3-28)$$

and the gimbal rate control input is designed as

$$\dot{\delta} = -\hat{\Upsilon}_1^+ (k + k_n) r, \quad (3-29)$$

where  $k, k_n \in \mathbb{R}$  denote positive control gains. Since the matrices  $\hat{\Upsilon}_1(t)$  and  $\hat{\Upsilon}_2(t)$  are non-square, the pseudo-inverses  $\hat{\Upsilon}_i^+ \in \mathbb{R}^{n \times 3} \forall i = 1, 2$  are defined so that  $\hat{\Upsilon}_i \hat{\Upsilon}_i^+ = I_3$ , and the matrix  $I_n - \hat{\Upsilon}_i^+ \hat{\Upsilon}_i$ , which projects vectors onto the null space of  $\hat{\Upsilon}_i$ , satisfies the

following properties:

$$\begin{aligned}
(I_n - \hat{Y}_i^+ \hat{Y}_i) (I_n - \hat{Y}_i^+ \hat{Y}_i) &= I_n - \hat{Y}_i^+ \hat{Y}_i \\
\hat{Y}_i (I_n - \hat{Y}_i^+ \hat{Y}_i) &= 0 \\
(I_n - \hat{Y}_i^+ \hat{Y}_i)^T &= (I_n - \hat{Y}_i^+ \hat{Y}_i) \\
(I_n - \hat{Y}_i^+ \hat{Y}_i) \hat{Y}_i^+ &= 0.
\end{aligned} \tag{3-30}$$

After substituting (3-27)-(3-29) into (3-25), the following closed-loop dynamics for  $r(t)$  can be obtained:

$$\begin{aligned}
J\dot{r} &= -\frac{1}{2}\dot{J}r + Y_1\tilde{\theta}_1 + Y_2\tilde{\theta}_2 - kr - k_n r \\
&\quad - C_T F_{sg} \operatorname{sgn}(\dot{\delta}) - C_W F_{sw} \operatorname{sgn}(\Omega) - e_v,
\end{aligned} \tag{3-31}$$

where the notation  $\tilde{\theta}_1(t) \in \mathbb{R}^{p_1}$  is defined as

$$\tilde{\theta}_1 = \theta_1 - \hat{\theta}_1. \tag{3-32}$$

Based on (3-25) and the subsequent stability analysis, the parameter estimates  $\hat{\theta}_1(t)$  and  $\hat{\theta}_2(t)$  are designed as

$$\dot{\hat{\theta}}_1 = \operatorname{proj}(\Gamma_1 Y_1^T r) \quad \dot{\hat{\theta}}_2 = \operatorname{proj}(\Gamma_2 Y_2^T r), \tag{3-33}$$

where  $\Gamma_1 \in \mathbb{R}^{p_1 \times p_1}$  and  $\Gamma_2 \in \mathbb{R}^{p_2 \times p_2}$  denote constant, positive-definite, diagonal adaptation gain matrices, and  $\operatorname{proj}(\cdot)$  denotes a projection algorithm utilized to guarantee that the  $i^{\text{th}}$  element of  $\hat{\theta}_1(t)$  and  $\hat{\theta}_2(t)$  can be bounded as

$$\underline{\theta}_{1i} \leq \hat{\theta}_{1i} \leq \bar{\theta}_{1i} \quad \underline{\theta}_{2i} \leq \hat{\theta}_{2i} \leq \bar{\theta}_{2i}, \tag{3-34}$$

where  $\underline{\theta}_{1i}, \bar{\theta}_{1i} \in \mathbb{R}$  and  $\underline{\theta}_{2i}, \bar{\theta}_{2i} \in \mathbb{R}$  denote known, constant lower and upper bounds for each element of  $\hat{\theta}_1(t)$  and  $\hat{\theta}_2(t)$ , respectively.

### 3.3.2 Adaptive Power Tracking Control Development

Based on (3-12) and (3-13), the power tracking error can be quantified as

$$\dot{\eta}_E = P_d - \dot{E}. \quad (3-35)$$

To develop the closed-loop dynamics for the power tracking error, the time derivative of (3-11) is substituted into (3-35) for  $\dot{E}(t)$  as

$$\dot{\eta}_E = P_d - \Upsilon_3 \dot{\Omega}, \quad (3-36)$$

where the uncertain vector  $\Upsilon_3(\Omega) \in \mathbb{R}^{1 \times 4}$  is defined as

$$\Upsilon_3 \triangleq \Omega^T I_W. \quad (3-37)$$

Since the uncertainty in (3-36) is linearly parameterizable, the following parameterization can be developed:

$$\Upsilon_3 \dot{\Omega} \triangleq Y_3 \theta_3, \quad (3-38)$$

where  $Y_3(\Omega, \dot{\Omega}) \in \mathbb{R}^{1 \times p_3}$  is a measurable regression matrix, and  $\theta_3 \in \mathbb{R}^{p_3}$  is a vector of unknown constants. To address the fact that the control input  $\dot{\Omega}(t)$  is premultiplied by an unknown time-varying matrix, an estimate of the uncertainty in (3-38), denoted by  $\hat{\Upsilon}_3(t) \in \mathbb{R}^{1 \times 4}$  is defined as

$$\hat{\Upsilon}_3 \dot{\Omega} \triangleq Y_3 \hat{\theta}_3, \quad (3-39)$$

where  $\hat{\theta}_3(t) \in \mathbb{R}^{p_3}$  is a subsequently designed estimate for the parametric uncertainty in  $\Upsilon_3(\Omega)$ . Based on (3-38) and (3-39), (3-36) can be rewritten as

$$\dot{\eta}_E = P_d - Y_3 \tilde{\theta}_3 - \hat{\Upsilon}_3 \dot{\Omega}, \quad (3-40)$$

where the notation  $\tilde{\theta}_3(t)$  is defined as

$$\tilde{\theta}_3 \triangleq \theta_3 - \hat{\theta}_3. \quad (3-41)$$

From (3-40) and the subsequent stability analysis, the parameter estimate  $\hat{\theta}_3(t)$  is designed as

$$\dot{\hat{\theta}}_3 = \text{proj}(-\Gamma_3 Y_3^T \eta_E), \quad (3-42)$$

where  $\Gamma_3 \in \mathbb{R}^{p_3 \times p_3}$  denotes a constant, positive-definite, diagonal adaptation gain matrix, and  $\text{proj}(\cdot)$  denotes a projection algorithm utilized to guarantee that the  $i^{\text{th}}$  element of  $\hat{\theta}_3(t)$  can be bounded as

$$\underline{\theta}_{3i} \leq \hat{\theta}_{3i} \leq \bar{\theta}_{3i}, \quad (3-43)$$

where  $\underline{\theta}_{3i}, \bar{\theta}_{3i} \in \mathbb{R}$  denote known, constant lower and upper bounds for each element of  $\hat{\theta}_3(t)$ , respectively. After substituting (3-27) into (3-40), the following expression can be obtained

$$\dot{\eta}_E = P_d - Y_3 \tilde{\theta}_3 + \hat{Y}_3 \hat{Y}_2^+ u_c + \hat{Y}_3 (I_4 - \hat{Y}_2^+ \hat{Y}_2) g. \quad (3-44)$$

Given (3-44),  $g(t)$  is designed to satisfy the following relationship

$$\hat{Y}_3 (I_4 - \hat{Y}_2^+ \hat{Y}_2) g = -P_d - \hat{Y}_3 \hat{Y}_2^+ u_c - k_E \eta_E, \quad (3-45)$$

where  $k_E \in \mathbb{R}$  is a positive constant control gain. Based on the Moore-Penrose pseudo-inverse properties introduced in (3-30), the minimum norm solution of (3-45) is given as

$$g = (I_4 - \hat{Y}_2^+ \hat{Y}_2) \hat{Y}_3^T \left[ \hat{Y}_3 (I_4 - \hat{Y}_2^+ \hat{Y}_2) \hat{Y}_3^T \right]^{-1} \cdot (-P_d - \hat{Y}_3 \hat{Y}_2^+ u_c - k_E \eta_E). \quad (3-46)$$

The result in (3-46) indicates that simultaneous attitude and power tracking is possible anytime  $(I_4 - \hat{Y}_2^+ \hat{Y}_2) \hat{Y}_3^T \neq 0$ . Since  $(I_4 - \hat{Y}_2^+ \hat{Y}_2) \neq 0 \forall \hat{Y}_2(t)$ , the simultaneous attitude and power tracking objective can be achieved as long as the following two conditions are

satisfied simultaneously:

$$\begin{aligned}\hat{\Upsilon}_3^T(t) &\neq 0 \\ \hat{\Upsilon}_3^T(t) &\notin \mathcal{N}\left(I_4 - \hat{\Upsilon}_2^+ \hat{\Upsilon}_2\right),\end{aligned}$$

where  $\mathcal{N}\left(I_4 - \hat{\Upsilon}_2^+ \hat{\Upsilon}_2\right)$  denotes the null space of the matrix  $I_4 - \hat{\Upsilon}_2^+ \hat{\Upsilon}_2$ . Since  $\hat{\Upsilon}_3(t)$  contains the adaptive elements of  $\hat{\theta}_3(t)$ , the projection function in (3-42) can be selected to expand the domain within which the simultaneous objective is possible. After substituting (3-46) into (3-44) for  $g(t)$ , the following closed-loop error system can be obtained:

$$\dot{\eta}_E = -k_E \eta_E - Y_3 \tilde{\theta}_3. \quad (3-47)$$

### 3.3.3 Stability Analysis

**Theorem 2-1:** The flywheel control input of (3-27), (3-28) and (3-46) along with the adaptive update laws given in (4-27) and the gimbal rate control input of (3-29) ensure globally uniformly ultimately bounded (GUUB) attitude tracking in the sense that

$$\|e_v(t)\| \leq \varepsilon_0 \exp(-\varepsilon_1 t) + \varepsilon_2, \quad (3-48)$$

where  $\varepsilon_0, \varepsilon_1, \varepsilon_2 \in \mathbb{R}$  denote positive bounding constants and asymptotic energy/power tracking in the sense that

$$\eta_E(t) \rightarrow 0 \quad \text{as} \quad t \rightarrow \infty. \quad (3-49)$$

*Proof:* To prove the asymptotic power tracking result, let  $V_E(\eta_E, \tilde{\theta}_3, t) \in \mathbb{R}$  be a nonnegative function defined as

$$V_E \triangleq \frac{1}{2} \eta_E^2 + \frac{1}{2} \tilde{\theta}_3^T \Gamma_3^{-1} \tilde{\theta}_3. \quad (3-50)$$

After using (3-42) and (3-47), the time derivative of  $V_E(t)$  can be expressed as

$$\dot{V}_E = -k_E \eta_E^2. \quad (3-51)$$

Based on (3-50) and (3-51),  $\eta_E(t) \in \mathcal{L}_\infty \cap \mathcal{L}_2$ . The assumption that  $\theta_3 \in \mathcal{L}_\infty$  can be used along with (3-43), to show that  $\tilde{\theta}_3(t) \in \mathcal{L}_\infty$ . Given that  $\eta_E(t) \in \mathcal{L}_\infty$ , (6-8), (3-27), (3-28), (3-34), and (3-46) can be used to show that  $\dot{\Omega}(t) \in \mathcal{L}_\infty$ . Since  $\dot{\Omega}(t) \in \mathcal{L}_\infty$ , (3-39) can be used along with (3-43) to conclude that  $Y_3(t) \in \mathcal{L}_\infty$ . Given that  $\eta_E(t), \tilde{\theta}_3(t), Y_3(t) \in \mathcal{L}_\infty$ , (3-47) can be used to conclude that  $\dot{\eta}_E(t) \in \mathcal{L}_\infty$  (i.e.,  $\eta_E(t)$  is uniformly continuous). Barbalat's Lemma can now be used to show that  $\eta_E(t) \rightarrow 0$  as  $t \rightarrow \infty$ .

To prove the GUUB attitude tracking result, consider the nonnegative function  $V(e_v, e_0, r, \tilde{\theta}_1, \tilde{\theta}_2, t) \in \mathbb{R}$  defined as

$$V \triangleq e_v^T e_v + (1 - e_0)^2 + \frac{1}{2} r^T J r + \frac{1}{2} \tilde{\theta}_1^T \Gamma_1^{-1} \tilde{\theta}_1 + \frac{1}{2} \tilde{\theta}_2^T \Gamma_2^{-1} \tilde{\theta}_2. \quad (3-52)$$

By using the bounds given in (2-15), (6-8), and (3-34),  $V(t)$  can be upper and lower bound as

$$\lambda_1 \|z\|^2 + c_1 \leq V(t) \leq \lambda_2 \|z\|^2 + c_2, \quad (3-53)$$

where  $\lambda_1, \lambda_2, c_1, c_2 \in \mathbb{R}$  are known positive bounding constants, and  $z(t) \in \mathbb{R}^6$  is defined as

$$z \triangleq \begin{bmatrix} e_v^T & r^T \end{bmatrix}^T. \quad (3-54)$$

From (3-17), (3-26), (3-31), and (3-32), the time derivative of  $V(t)$  can be expressed as

$$\begin{aligned} \dot{V} &= e_v^T (e_v^\times + e_0 I_3) \tilde{\omega} + (1 - e_0) e_v^T \tilde{\omega} + r^T \left( Y_1 \tilde{\theta}_1 + Y_2 \tilde{\theta}_2 - k r - k_n r - e_v \right. \\ &\quad \left. - C_T F_{sg} \operatorname{sgn}(\dot{\delta}) - C_W F_{sw} \operatorname{sgn}(\Omega) \right) - \tilde{\theta}_1^T \Gamma_1^{-1} \dot{\tilde{\theta}}_1 - \tilde{\theta}_2^T \Gamma_2^{-1} \dot{\tilde{\theta}}_2. \end{aligned} \quad (3-55)$$

By using (3-16), (4-27), and exploiting the fact that

$$e_v^T e_v^\times \tilde{\omega} = 0,$$

the expression in (3-55) can be upper bounded as

$$\dot{V} \leq -\lambda_3 \|z\|^2 - k_n \|r\|^2 + (\zeta_0 \|F_{sg}\|_{i_\infty} + \zeta_1 \|F_{sw}\|_{i_\infty}) \|r\|, \quad (3-56)$$

where  $\lambda_3 = \lambda_{\min} \{\alpha, k\} \in \mathbb{R}$ . After completing the squares, (3-56) can be written as

$$\dot{V}(t) \leq -\lambda_3 \|z\|^2 + \frac{\beta^2}{4k_n}, \quad (3-57)$$

where  $\beta \triangleq \zeta_0 \|F_{sg}\|_{i_\infty} + \zeta_1 \|F_{sw}\|_{i_\infty}$ . Since the inequality in (3-53) can be utilized to lower bound  $\|z(t)\|^2$  as

$$\|z\|^2 \geq \frac{1}{\lambda_2} V(t) - \frac{c_2}{\lambda_2}, \quad (3-58)$$

the inequality in (3-57) can be expressed as

$$\dot{V}(t) \leq -\frac{\lambda_3}{\lambda_2} V(t) + \varepsilon, \quad (3-59)$$

where  $\varepsilon \in \mathbb{R}$  is a positive constant that is defined as

$$\varepsilon = \frac{\beta^2}{4k_n} + \frac{\lambda_3 c_2}{\lambda_2}. \quad (3-60)$$

The linear differential inequality in (3-59) can be solved as

$$V(t) \leq V(0) \exp\left(-\frac{\lambda_3}{\lambda_2} t\right) + \varepsilon \frac{\lambda_2}{\lambda_3} \left[1 - \exp\left(-\frac{\lambda_3}{\lambda_2} t\right)\right]. \quad (3-61)$$

The expressions in (3-52) and (3-61) can be used to conclude that  $r(t) \in \mathcal{L}_\infty$ . Thus, from (6-8), (3-16), and (3-54),  $\tilde{\omega}(t), z(t) \in \mathcal{L}_\infty$ , and (3-15) can be used to conclude that  $\omega(t) \in \mathcal{L}_\infty$ . Equation (3-17) then shows that  $\dot{e}_v(t), \dot{e}_0(t) \in \mathcal{L}_\infty$ . Hence, (3-22), (3-24), (3-27)-(3-29), (3-34), (3-46), and (3-49) can be used along with the assumption that  $E_d(t), P_d(t) \in \mathcal{L}_\infty$  to prove that the control inputs  $\dot{\delta}(t), \dot{\Omega}(t) \in \mathcal{L}_\infty$ . Standard signal chasing arguments can then be utilized to prove that all remaining signals remain bounded during closed-loop operation. The inequalities in (3-53) can now be used along with (3-60) and (3-61) to conclude that

$$\|z\|^2 \leq \left(\frac{\lambda_2 \|z(0)\|^2 + c_2}{\lambda_1}\right) \exp\left\{-\frac{\lambda_3}{\lambda_2} t\right\} + \left(\frac{\lambda_2 \beta^2}{4k_n \lambda_3 \lambda_1} + \frac{c_2 - c_1}{\lambda_1}\right). \quad (3-62)$$

The result in (3-48) can now be directly obtained from (3-62).

### 3.4 Simulation Study

To test the performance of the proposed IPACS, the dynamic parameters of the UF CMG test bed were used to create a numerical simulation. While the UF CMG does not have variable wheel speed capabilities, a realistic numerical simulation environment was created as a stepping stone to actual experimental validation of the proposed control law. To that end, using the physical parameters of the UF CMG test bed to create the VSCMG model, the controller performance was tested in a simulation environment containing measurement noise and time delays. Moreover, to ensure that the simulation demonstrates the capability of the controller to perform satisfactorily in practical implementation, the controller parameters were tuned such that the control objective is achieved using actuator commands that are within practical saturation and rate limits.

Using the dynamic equations of motion in terms of the VSCMG test bed in (3-1)-(3-2) and the VSCMG test bed inertia matrix  $J_{vscmg}(\delta) \in \mathbb{R}^{3 \times 3}$  is defined using the parallel axis theorem as

$$J_{vscmg} \triangleq J_0 + \sum_{i=1}^4 [{}^B J_{gi} + m_{cmgi} (r_i^T r_i I_3 - r_i r_i^T)]. \quad (3-63)$$

In (3-63), the VSCMG parameters  $J_0 \triangleq J_{vscmg}(0) = \text{diag}\{6.10 \times 10^{-2}, 6.10 \times 10^{-2}, 7.64 \times 10^{-2}\} \text{ kg} \cdot \text{m}^2$ ,  $m_{cmgi} = 0.265 \text{ kg}$ ,  $r_i \in \mathbb{R}^3 \forall i = 1, 2, 3, 4$  are defined as

$$r_1 \triangleq \begin{bmatrix} 0.1591 & 0 & 0.1000 \end{bmatrix}^T m \quad (3-64)$$

$$r_2 \triangleq \begin{bmatrix} 0 & 0.1591 & 0.1000 \end{bmatrix}^T m \quad (3-65)$$

$$r_3 \triangleq \begin{bmatrix} -0.1591 & 0 & 0.1000 \end{bmatrix}^T m \quad (3-66)$$

$$r_4 \triangleq \begin{bmatrix} 0 & -0.1591 & 0.1000 \end{bmatrix}^T m, \quad (3-67)$$

${}^B J_{gi}(\delta) \in \mathbb{R}^{3 \times 3} \forall i = 1, 2, 3, 4$  denotes the inertia matrix of the  $i^{\text{th}}$  gimbal as expressed in the CMG body-fixed frame defined as

$${}^B J_{gi} \triangleq [C_{Bgi}] [{}^{gi} J_{gi}] [C_{Bgi}]^T, \quad (3-68)$$

and  $I_n$  denotes the  $n \times n$  identity matrix. The actual values for the parameters  $J_0$ ,  $I_{ws}$ ,  $I_{cg}$ ,  $F_{dg}$ ,  $F_{dw}$ ,  $F_{sg}$ ,  $F_{sw}$ ,  $m_{cmgi}$ , and  ${}^{g^i}J_{gi} \forall i = 1, 2, 3, 4$  are used to generate the plant model in the simulation, but they are not used in the control law. The adaptive control law compensates for these uncertain parameters. In (3-68), the coordinate transformation matrix  $C_{Bgi} \in SO(3) \forall i = 1, 2, 3, 4$  relates the  $i^{th}$  gimbal-fixed frame to the VSCMG body-fixed frame, and  ${}^{g^i}J_{gi} = \text{diag} \left\{ 2.80 \times 10^{-3} \quad 4.89 \times 10^{-4} \quad 2.49 \times 10^{-3} \right\} \text{ kg} \cdot \text{m}^2 \forall i = 1, 2, 3, 4$  represents the inertia matrix of the  $i^{th}$  gimbal as expressed in the  $i^{th}$  gimbal-fixed frame. Also in (3-1),  $I_G^{CMG} = 2.80 \times 10^{-3} I_4 \text{ kg} \cdot \text{m}^2$ , and  $I_W = 6.95 \times 10^{-4} I_4 \text{ kg} \cdot \text{m}^2$ . The skew angle of the VSCMG pyramid is  $\beta = 54.74 \text{ deg}$ .

The objective is to regulate a satellite's attitude to the desired quaternion defined by

$$q_d = \begin{bmatrix} 1 & 0 & 0 & 0 \end{bmatrix}^T \quad (3-69)$$

with the initial quaternion orientation of the satellite given by

$$q(0) = \begin{bmatrix} 0.4 & -0.3 & 0.8 & 0.4 \end{bmatrix}^T .$$

The adaptive estimates were initialized to arbitrary values in the simulation to test a case when limited knowledge of the parameters is available. The initial values for the adaptive

estimates were selected as follows.

$$\begin{aligned}
\hat{\theta}_1(0) &= [6 \times 10^{-2}, 6 \times 10^{-2}, 9 \times 10^{-2}, 7.5 \times 10^{-3}, \\
&\quad 1.2 \times 10^{-3}, 6 \times 10^{-3}, 3 \times 10^{-4}, 3 \times 10^{-4}, \\
&\quad 3 \times 10^{-4}, 3 \times 10^{-4}, 0.3, 0.3, 0.3, 0.3, \\
&\quad 1.04 \times 10^{-3}, 1.04 \times 10^{-3}, 1.04 \times 10^{-3}, \\
&\quad 1.04 \times 10^{-3}] \\
\hat{\theta}_2(0) &= [1.2 \times 10^{-3}, 6.0 \times 10^{-3}, 1.5 \times 10^{-2}, \\
&\quad 1.5 \times 10^{-2}, 1.5 \times 10^{-2}, 1.5 \times 10^{-2}, \\
&\quad 1.04 \times 10^{-3}, 1.04 \times 10^{-3}, 1.04 \times 10^{-3}, \\
&\quad 1.04 \times 10^{-3}, 3 \times 10^{-3}, 3 \times 10^{-3}, 3 \times 10^{-3}, \\
&\quad 3 \times 10^{-3}] \\
\hat{\theta}_3(0) &= [2.78 \times 10^{-3}, 2.78 \times 10^{-3}, 2.78 \times 10^{-3}, \\
&\quad 2.78 \times 10^{-3}],
\end{aligned}$$

and the gimbal angles (*rad*) and flywheel speeds (*rad/s*) were initialized as

$$\begin{aligned}
\delta(0) &= \begin{bmatrix} 1 & 1 & 1 & 1 \end{bmatrix}^T \\
\Omega(0) &= \begin{bmatrix} 10 & 10 & 10 & 10 \end{bmatrix}^T,
\end{aligned}$$

respectively.

The friction matrices  $F_{dg}$ ,  $F_{dw}$ ,  $F_{sg}$ , and  $F_{sw}$  for the simulated VSCMG are (e.g., see [66])

$$\begin{aligned}
F_{dg} &= 2 \times 10^{-2} I_4 & F_{sg} &= 4 \times 10^{-2} I_4 \\
F_{dw} &= 2 \times 10^{-4} I_4 & F_{sw} &= 4 \times 10^{-4} I_4.
\end{aligned} \tag{3-70}$$

To test the scenario when a sudden increase in the friction occurs, an instantaneous jump (i.e., step function) of  $10^{-2}$  in the  $F_{dg}$ ,  $F_{dw}$ ,  $F_{sg}$ , and  $F_{sw}$  parameters is programmed to occur 1 second into the simulation. Additionally, a sudden increase of 10% in the friction parameters is programmed to occur after the first period of power tracking at 6,000 sec<sup>1</sup>. To improve the realism of the simulation environment, Gaussian distributed random number noise of 10% was added to all sensor measurements in the simulation, and a fixed time step of  $10^{-2}$  sec was used.

Figures 3-1 - 3-16 show the simulation results of the closed-loop system. Figure 3-1 shows the quaternion tracking error during closed-loop operation for the entire duration (15,000 sec) of the numerical simulation. To show the initial transient response, Figure 3-2 shows a plot of the first 200 sec of the quaternion tracking error plot. Figure 3-3 highlights the quaternion tracking error response during the sudden friction increase at 6,000 sec. Figures 3-4 and 3-6 show the power and energy tracking achieved during closed-loop controller operation. Figure 3-4 shows the power and energy profiles and the corresponding closed-loop system response for the entire duration of the simulation, and Figure 3-5 shows the first 10 sec to highlight the initial transient response. Figure 3-6 highlights the power and energy tracking error responses during the step increase in friction occurring at 6000 sec. Figures 3-7 - 3-9 show the control input gimbal rates  $\dot{\delta}(t)$  and wheel accelerations  $\dot{\Omega}(t)$  during closed loop operation. The spikes shown in the control input responses  $\dot{\delta}(t)$  and  $\dot{\Omega}(t)$  occur at instants where the desired power profile instantaneously changes sign from negative to positive (see Figure 3-4). Although the spikes appear to exceed practical rate limitations of the actuators, this is due to the resolution of Figure 3-7. The effect of the sudden friction increase on the control

---

<sup>1</sup> In a realistic situation, the gimbal friction would most likely increase gradually over time (e.g., due to bearing degradation, corrosion, etc.), so the instantaneous increase in friction in the simulation tests a worst case scenario.

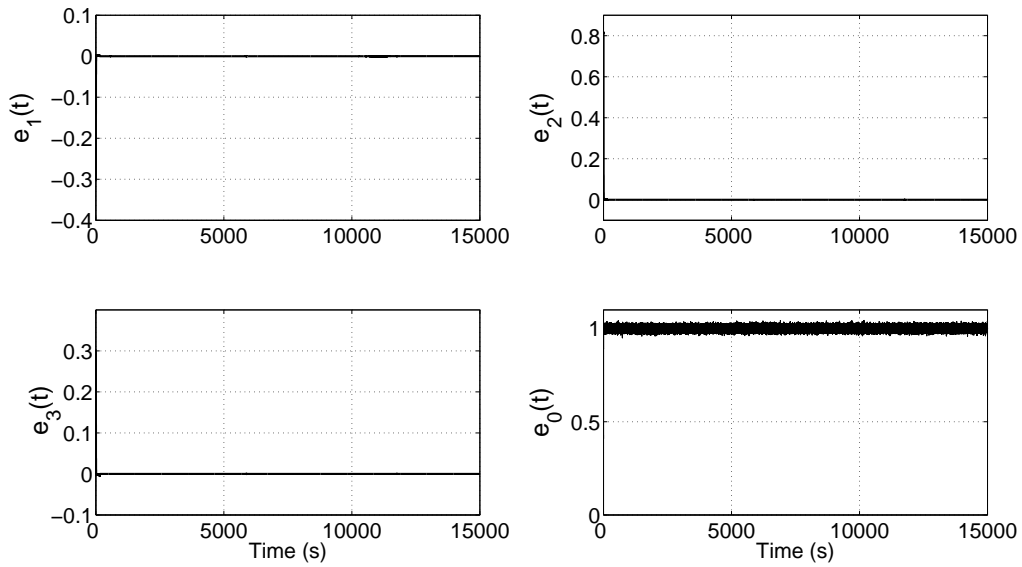


Figure 3-1. Quaternion tracking error  $e(t)$  during closed-loop operation.

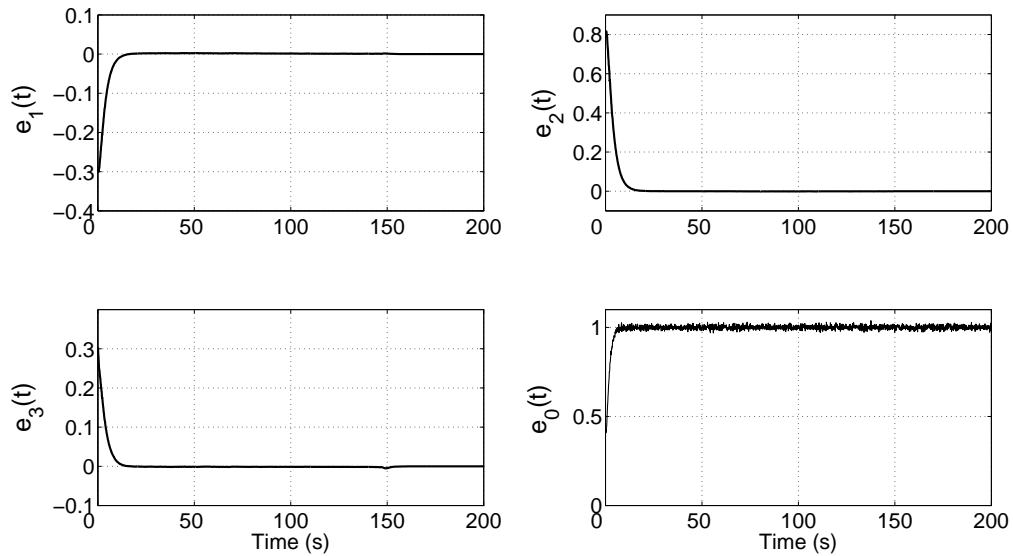


Figure 3-2. Transient response of the quaternion tracking error  $e(t)$ .



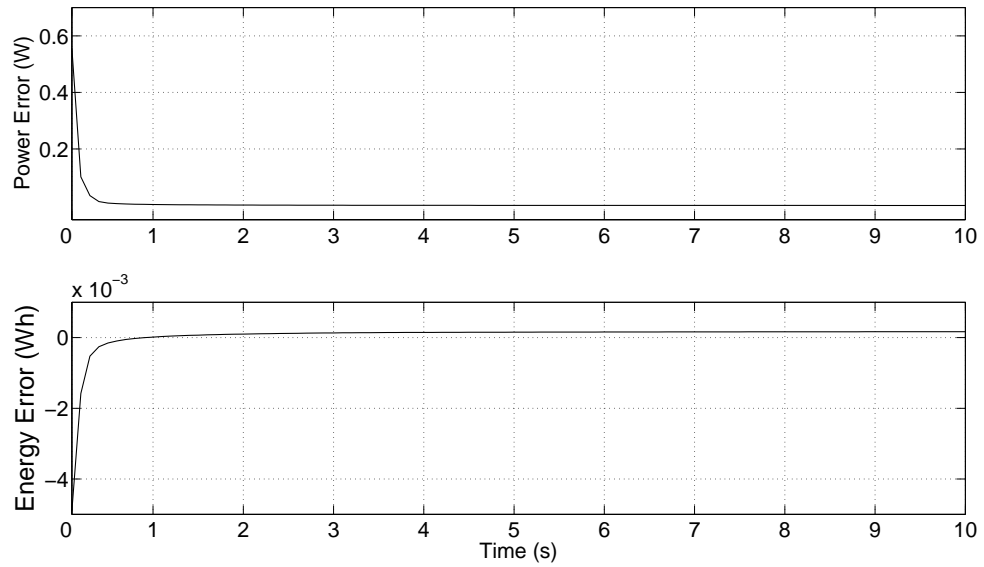


Figure 3-5. Transient power and energy tracking error.

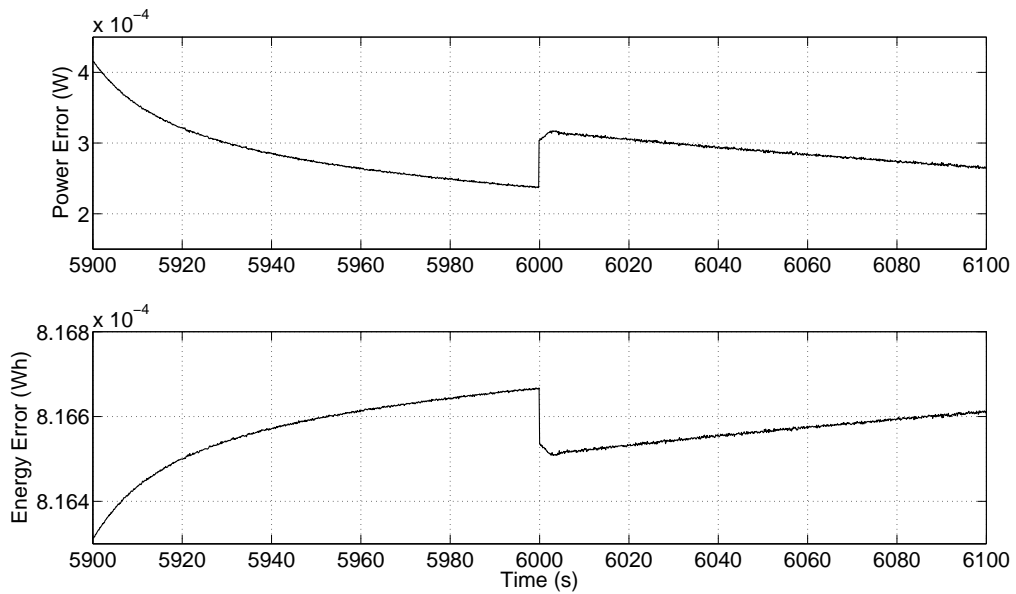


Figure 3-6. Power and energy tracking error response during sudden friction increase at 6,000 sec.

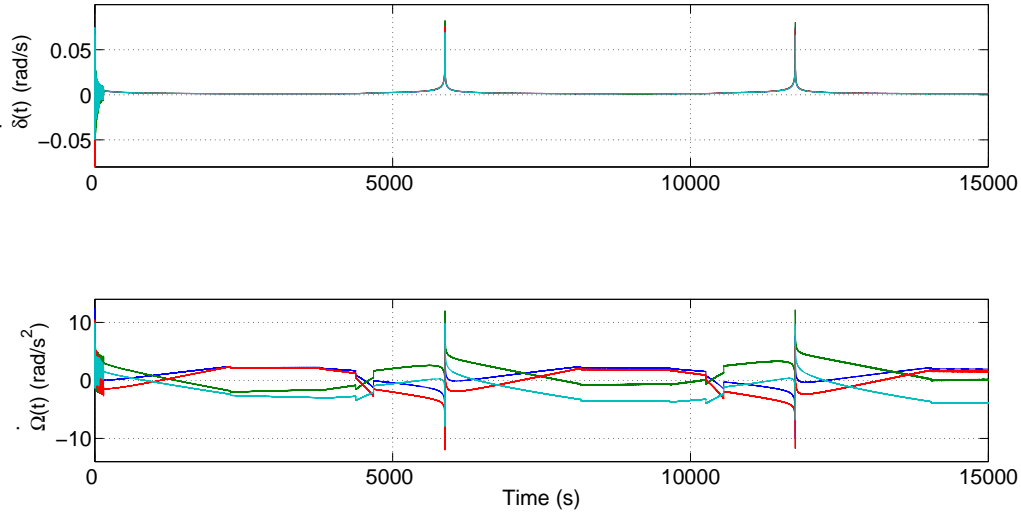


Figure 3-7. Control input gimbal rates  $\dot{\delta}(t)$  and wheel accelerations  $\dot{\Omega}(t)$ .

input responses is shown in Figure 3-9. The commanded control inputs remain within reasonable rates throughout controller operation. The wheel speeds used during closed-loop operation are shown in Figure 3-10. The maximum wheel speed commanded was approximately 9,500 *rpm*, which is a reasonable value for practical implementation. The time variation of the adaptive parameter estimates is shown in Figures 3-11 - 3-16. Some of the parameter estimates did not vary much during closed-loop operation, but the estimates remained bounded for the duration of the numerical simulation. Figure 3-11 shows the elements of the adaptive parameter vectors  $\hat{\theta}_1(t)$ ,  $\hat{\theta}_2(t)$ , and  $\hat{\theta}_3(t)$  for the entire duration of closed-loop controller operation. Figures 3-12, 3-14, and 3-16 show the transient response of the adaptive parameter estimates during the first 10 seconds of closed-loop operation. Figure 3-12 depicts the vector elements of  $\hat{\theta}_1(t)$ , Figure 3-14 depicts the elements of  $\hat{\theta}_2(t)$ , and Figure 3-16 depicts  $\hat{\theta}_3(t)$ . Figures 3-13 and 3-15 highlight the responses of  $\hat{\theta}_1(t)$  and  $\hat{\theta}_2(t)$  during the sudden increase in friction at 6,000 sec. Since different vector elements of  $\hat{\theta}_1(t)$  and  $\hat{\theta}_2(t)$  had different initial conditions and amounts of variation, the plots in Figures 3-12 - 3-15 were divided into multiple windows for clarity.

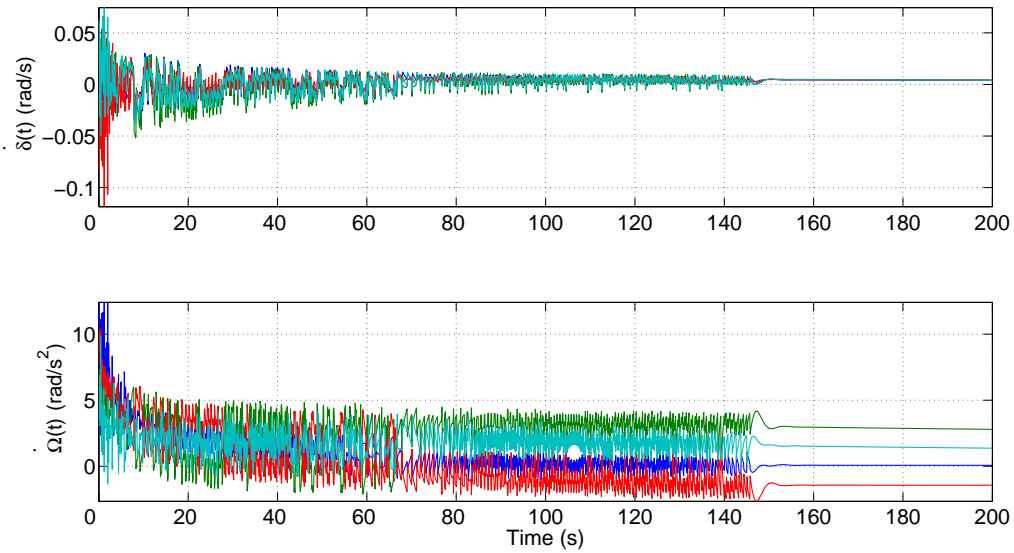


Figure 3-8. Transient response of the control input gimbal rates  $\dot{\delta}(t)$  and wheel accelerations  $\dot{\Omega}(t)$ .

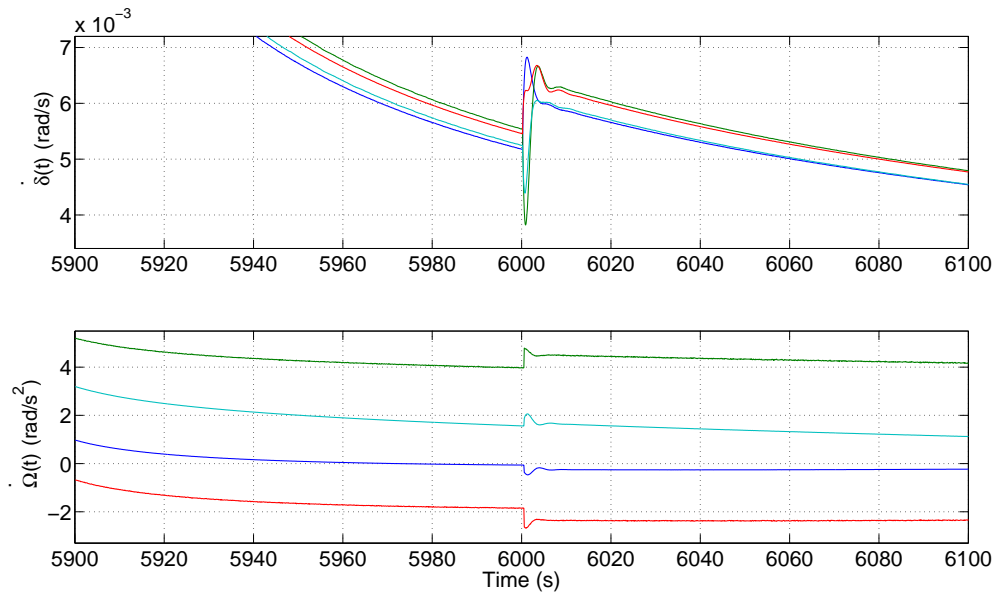


Figure 3-9. Response of the control input gimbal rates  $\dot{\delta}(t)$  and wheel accelerations  $\dot{\Omega}(t)$  during sudden increase of friction parameters at 6,000 sec.

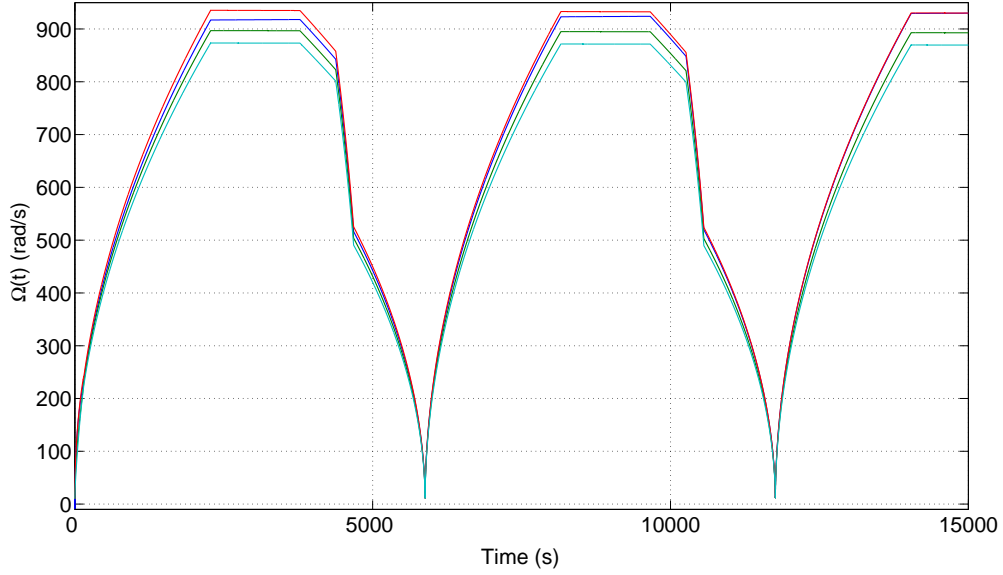


Figure 3-10. Wheel speeds  $\Omega(t)$  during closed-loop controller operation.

Some of the parameter estimates vary by small magnitudes on the order of  $10^{-4}$ . However, after utilizing equations (3-1), (3-2), (3-22), (3-23), (3-27) - (3-29), and (3-38), it can be shown that the equivalent control torque resulting from the feedforward terms  $\hat{\theta}_1(t)$ ,  $\hat{\theta}_2(t)$ , and  $\hat{\theta}_3(t)$  all have similar magnitudes, which is of the same order of magnitude as that of the feedback control terms.

### 3.5 Summary

In this chapter, an IPACS design method for a VSCMG-actuated satellite is presented. In the presence of uncertain dynamic and static friction in the VSCMG gimbals and wheels, the controller is capable of achieving GUUB attitude tracking while simultaneously tracking a desired power profile asymptotically. In addition, the controller compensates for the effects of uncertain, time-varying satellite inertia properties. The difficulties arising from dynamic friction and uncertain satellite inertia are mitigated through innovative development of the error system along with a Lyapunov-based adaptive law. In the presence of static friction, the control design is complicated due to the control input being embedded in a discontinuous nonlinearity. This difficulty is overcome with the

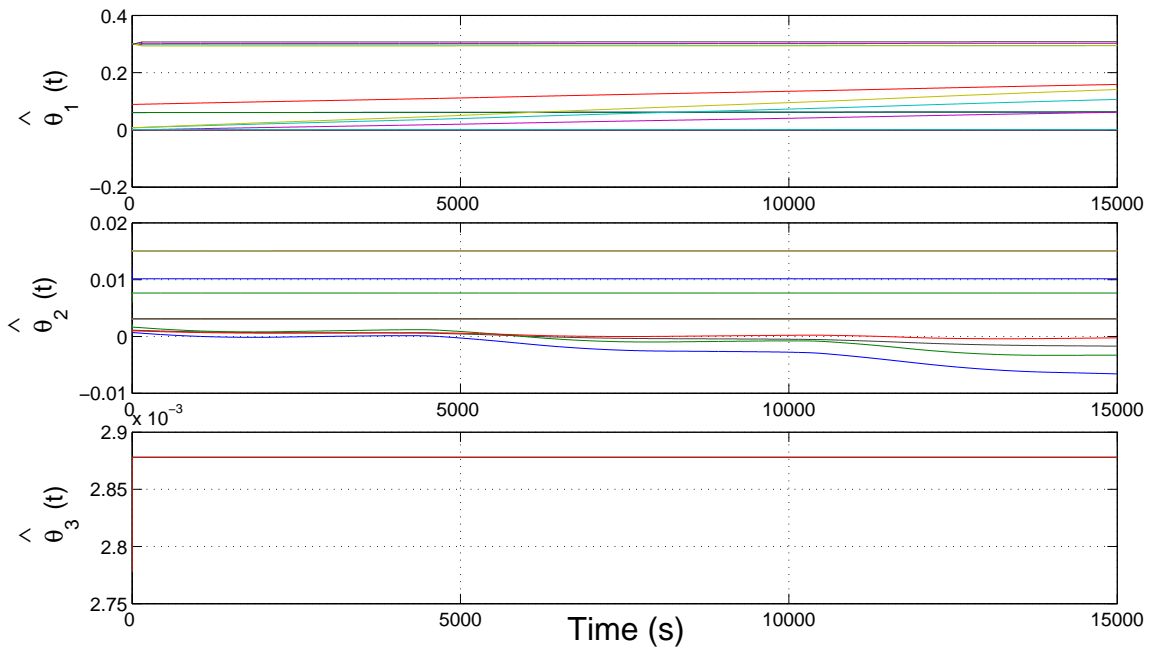


Figure 3-11. Adaptive parameter estimates  $\hat{\theta}_1(t)$ ,  $\hat{\theta}_2(t)$ , and  $\hat{\theta}_3(t)$  during closed-loop operation.

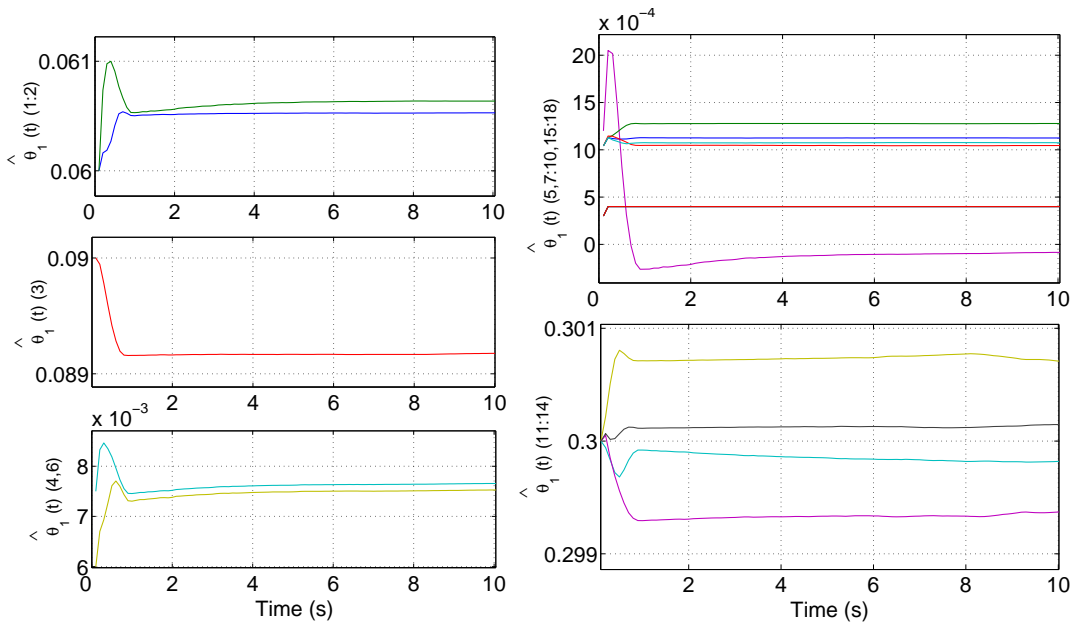


Figure 3-12. Initial transient response of the vector elements of the adaptive estimate  $\hat{\theta}_1(t)$ .

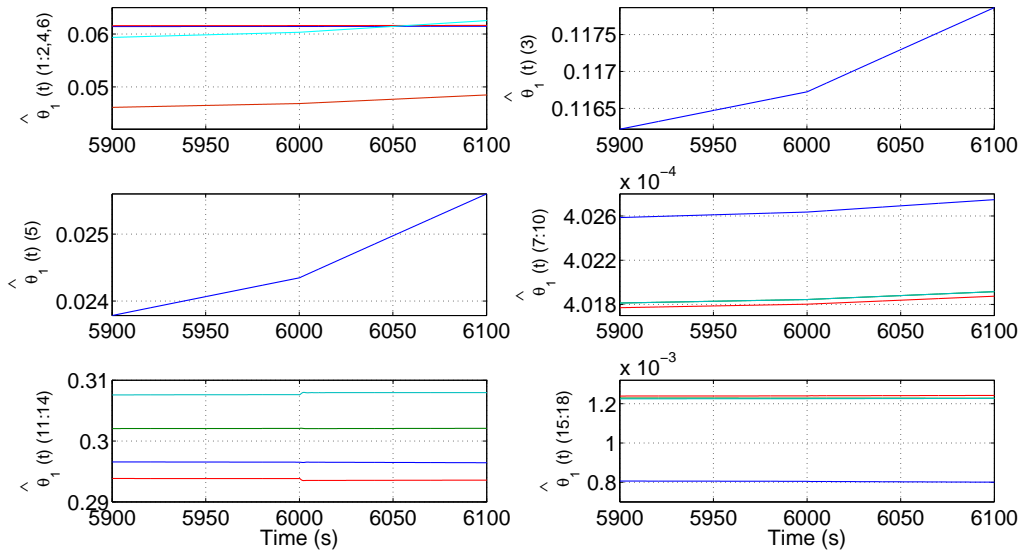


Figure 3-13. Response of the vector elements of the adaptive estimate  $\hat{\theta}_1(t)$  during the sudden friction increase at 6,000 sec.

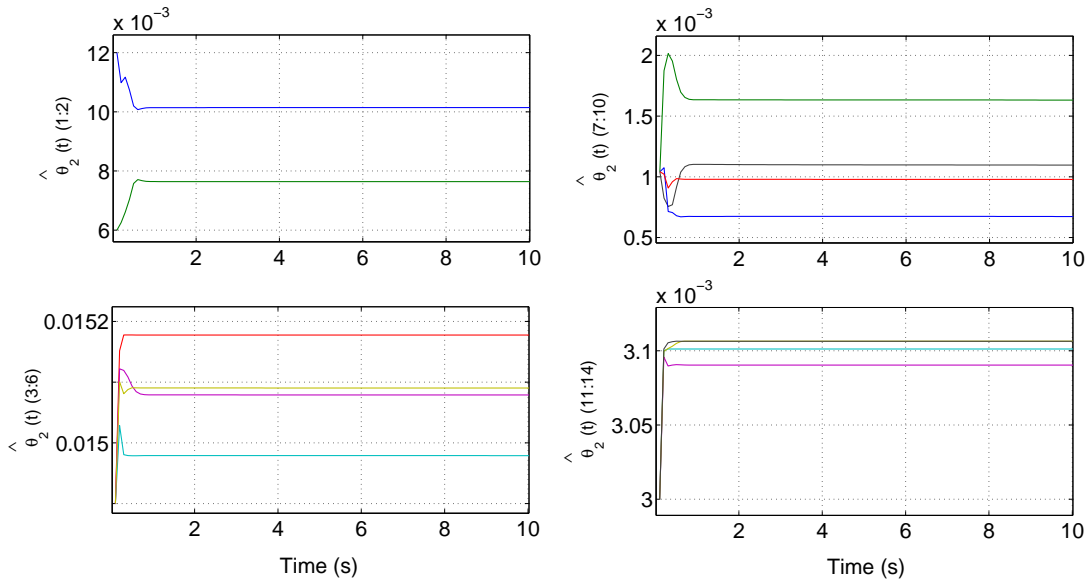


Figure 3-14. Initial transient response of the vector elements of the adaptive estimate  $\hat{\theta}_2(t)$ .

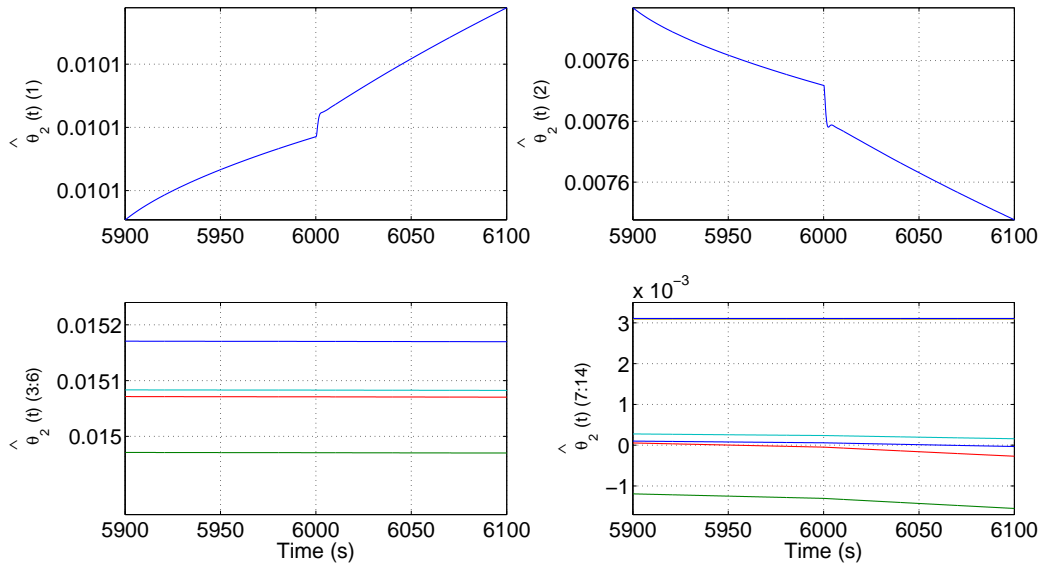


Figure 3-15. Response of the vector elements of the adaptive estimate  $\hat{\theta}_2(t)$  during the sudden friction increase at 6,000 sec.

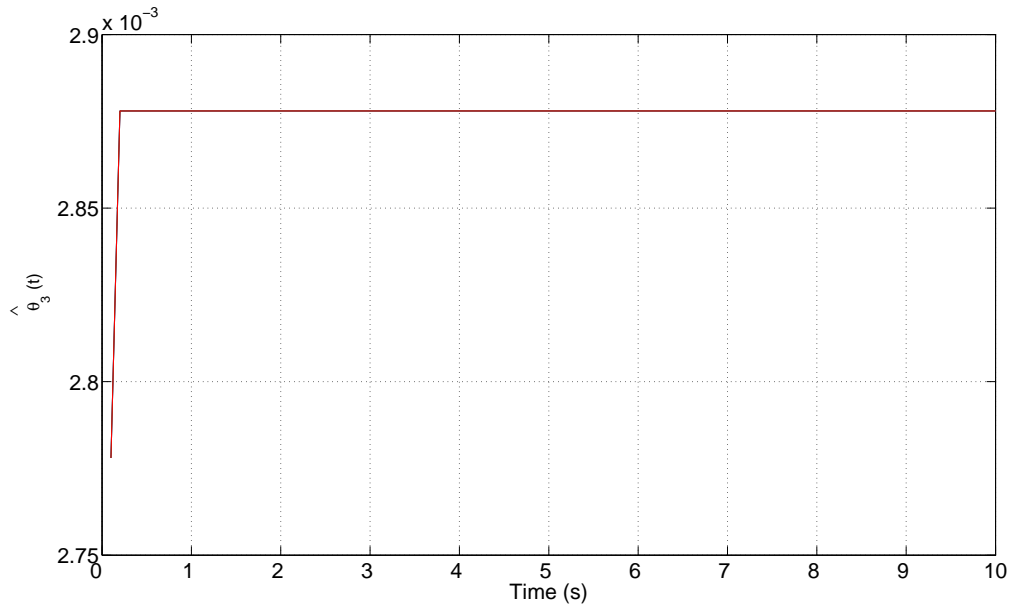


Figure 3-16. Initial transient response of the adaptive estimate  $\hat{\theta}_3(t)$ .

use of a robust control element. The attitude and power tracking results are proven via Lyapunov stability analysis and demonstrated through numerical simulations.

## CHAPTER 4 INTEGRATED POWER REDUCTION AND ADAPTIVE ATTITUDE CONTROL SYSTEM OF A SATELLITE

In this chapter, an attitude controller is developed to adaptively estimate actuator friction where attitude control torques are generated by means of a pyramidal arrangement of four single gimbal VSCMGs. To develop the controller from coupled dynamics composed of the satellite, gimbals, and wheels, a backstepping method is exploited. Input power reduction results from a wheel deceleration mode induced by null solution in addition to internal friction of the flywheels. Internal friction reduces the potential input torque to be produced by the flywheels since the friction in deceleration can play a role as additional torque generation to the resultant torque which consists of the applied control torque and friction. The developed VSCMG steering law is a function of the gimbal rates and the flywheel velocities which are weighted by the singularity measure [97] to actively exploit the additional degree of freedom afforded by the VSCMGs [55, 89, 100]. In a stationary state after completing an arbitrary attitude maneuver, the wheel speeds can potentially be reduced. A benefit of the controller is that power reduction can be achieved when the wheels decelerate while the gimbals null motion simultaneously performs the gimbal reconfiguration for singularity avoidance. The singularity avoidance method reduces/eliminates the amount of time that the VSCMG has to operate in RW mode when the CMG Jacobian becomes singular in impassable/passable singular surface through the use of null motion [55, 64, 96, 100]. Numerical simulations demonstrate the performance of the adaptive VSCMG steering law to indicate the input power reduction for control of VSCMGs in the presence of friction and the efficacy of singularity avoidance with reduced reaction wheel modes.

### 4.1 Coupled Dynamics

#### 4.1.1 Dynamics for VSCMGs

The gimbal and flywheel of a VSCMG assembly (Figure 2-1) have a center of mass (CM),  $C_{G_i}$  and  $C_{W_i}$ , respectively. By placing the CMG assembly inside a satellite, the

angular momentum  $h_{C_{CMG_i}}^{CMG_i}(\omega, \dot{\delta}_i, \Omega_i) \in \mathbb{R}^3$  of the  $i^{th}$  CMG with respect to its CM,  $C_{CMG_i}$  is written as

$$h_{C_{CMG_i}}^{CMG_i} = I_{C_{CMG_i}}^{CMG_i} \omega + h_{C_{CMG_i}}^{CMG_i/S}, \quad (4-1)$$

where the sub- and superscript notation indicate a point of interest and a body, respectively,  $\omega(t) \in \mathbb{R}^3$  denotes the angular velocity of the satellite,  $\delta_i(t), \dot{\delta}_i(t), \Omega_i(t) \in \mathbb{R}$  are the gimbal angle, the gimbal rate, and the flywheel velocity of the  $i^{th}$  CMG, and  $I_{C_{CMG_i}}^{CMG_i} \in \mathbb{R}^{3 \times 3}$  is the moment of inertia tensor of the  $i^{th}$  CMG relative to  $C_{CMG_i}$ . Specifically, the moment of inertia tensor of the  $i^{th}$  CMG is

$$I_{C_{CMG_i}}^{CMG_i} = I_{C_{CMG}}^{G_i} + m_{G_i} \left[ \left( r_{C_{G_i}}^T r_{C_{G_i}} \right) I_3 - r_{C_{G_i}} r_{C_{G_i}}^T \right] + I_{C_{CMG}}^{W_i} + m_{W_i} \left[ \left( r_{C_{W_i}}^T r_{C_{W_i}} \right) I_3 - r_{C_{W_i}} r_{C_{W_i}}^T \right],$$

where  $I_{C_{CMG}}^{G_i}, I_{C_{CMG}}^{W_i} \in \mathbb{R}^{3 \times 3}$  are the moments of inertia tensor of each gimbal and wheel relative to  $C_{CMG_i}$ , and  $m_{G_i}, m_{W_i} \in \mathbb{R}$  are masses of the  $i^{th}$  gimbal and wheel, where  $r_{C_{G_i}}, r_{C_{W_i}} \in \mathbb{R}^3$  are the positions of the CM for  $C_{G_i}$  and  $C_{W_i}$  with respect to  $C_{CMG_i}$ . Also in (4-1),  $h_{C_{CMG_i}}^{CMG_i/S}(\dot{\delta}_i, \Omega_i)$  represents the angular momentum contributions from the flywheel and the gimbal and is given by

$$h_{C_{CMG_i}}^{CMG_i/S} = I_{C_{CMG_i}}^{CMG_i} \dot{\delta}_i \hat{a}_{G_i} + I_{C_{CMG_i}}^{CMG_i} \Omega_i \hat{a}_{W_i}, \quad (4-2)$$

where the angular momentum of the CMG is expressed in terms of a CMG-fixed basis  $\mathcal{B} = \left\{ \hat{a}_{G_i}, \hat{a}_{W_i}, \hat{a}_{T_i} \right\}$ ;  $\hat{a}_{G_i}$  is a gimbal axis,  $\hat{a}_{W_i}$  is a spinning wheel axis, and  $\hat{a}_{T_i}$  is a transverse axis. To obtain the kinetic equation governing the motion of the  $i^{th}$  CMG, the time derivative of (4-1) yields

$$\dot{h}_{C_{CMG_i}}^{CMG_i} = I_{C_{CMG_i}}^{CMG_i} \dot{\omega} + \frac{d}{dt} \left( I_{C_{CMG_i}}^{CMG_i} \right) \omega + \dot{h}_{C_{CMG_i}}^{CMG_i/S} = g^{CMG_i}, \quad (4-3)$$

where  $g^{CMG_i}(t) = \tau^{CMG_i}(t) - g_{Friction}^{CMG_i}(\dot{\delta}_i, \Omega_i) \in \mathbb{R}^3$  represents the applied gimbal and/or flywheel motor torques  $\tau^{CMG_i}(t)$  and the associated friction torques  $g_{Friction}^{CMG_i}(\dot{\delta}_i, \Omega_i)$ .

Given a CMG-fixed frame  $\mathcal{F}_{CMG_i}$ , the transport theorem indicates that

$$\begin{aligned} \dot{h}_{CMG_i}^{CMG_i} &= I_{CMG_i}^{CMG_i} \left( \dot{\omega} + \ddot{\delta}\hat{a}_{G_i} + \dot{\Omega}_i\hat{a}_{W_i} \right) + \left( \omega + \delta\hat{a}_{G_i} \right)^\times h_{G_i} \\ &\quad + \left( \omega + \delta\hat{a}_{G_i} + \Omega_i\hat{a}_{W_i} \right)^\times h_{W_i}, \end{aligned} \quad (4-4)$$

where  $h_{G_i} \triangleq I_{CMG_i}^{CMG_i} \left( \omega + \delta\hat{a}_{G_i} \right)$ , and  $h_{W_i} \triangleq I_{CMG_i}^{CMG_i} \Omega_i\hat{a}_{W_i} \in \mathbb{R}^3$ . Considering a coordinate system with origin  $C_{CMG_i}$  and basis  $\mathcal{B}$  fixed in each CMG unit, (4-4) is expressed as

$$\begin{aligned} {}^{CMG_i} \dot{h}_{CMG_i}^{CMG_i} &= {}^{CMG_i} I_{CMG_i}^{CMG_i} \left( D_{CMG_i}^T \dot{\omega} + \ddot{\delta}\hat{a}_{G_i} + \dot{\Omega}_i\hat{a}_{W_i} \right) \\ &\quad + \left( D_{CMG_i}^T \omega + \delta\hat{a}_{G_i} \right)^\times h_{G_i} + \left( D_{CMG_i}^T \omega + \delta\hat{a}_{G_i} + \Omega_i\hat{a}_{W_i} \right)^\times h_{W_i}, \end{aligned}$$

where  ${}^{CMG_i} I_{CMG_i}^{CMG_i} \in \mathbb{R}^{3 \times 3}$  is the moment of inertia matrix of the  $i^{th}$  CMG expressed in the CMG-fixed frame  $\mathcal{F}_{CMG_i}$ , and assuming that  ${}^{CMG_i} I_{CMG_i}^{CMG_i}$  is a principal inertia matrix, the CMG inertia matrix can be defined as  ${}^{CMG_i} I_{CMG_i}^{CMG_i} = \text{diag} \left( \left[ \begin{array}{ccc} I_{G_i}^{CMG_i} & I_{W_i} & I_{T_i}^{CMG_i} \end{array} \right] \right)$  since  ${}^{CMG_i} I_{CMG_i}^{CMG_i} \hat{a}_{W_i} = I_{W_i} \hat{a}_{W_i}$  so that  $h_{W_i} \triangleq I_{W_i} \Omega_i \hat{a}_{W_i}$ , and  $D_{CMG_i}^T(\delta_i) \in \mathbb{R}^{3 \times 3}$  is the direction cosine matrix which transforms  $\mathcal{F}_S$  to  $\mathcal{F}_{CMG_i}$ . The gimbal motor torque and bearing friction contributions are obtained from

$$\begin{aligned} {}^{CMG_i} \dot{h}_{CMG_i}^{CMG_i} \cdot \hat{a}_{G_i} &= \hat{a}_{G_i} \cdot \left[ {}^{CMG_i} I_{CMG_i}^{CMG_i} \left( D_{CMG_i}^T \dot{\omega} + \ddot{\delta}\hat{a}_{G_i} \right) \right] + \hat{a}_{G_i} \cdot \left[ \left( D_{CMG_i}^T \omega + \delta\hat{a}_{G_i} \right)^\times h_{W_i} \right] \\ &= \tau_{Gimbal_{motor}}^{CMG_i} - g_{Gimbal_{Friction}}^{CMG_i}, \end{aligned} \quad (4-5)$$

where  $\tau_{Gimbal_{motor}}^{CMG_i}(t)$ ,  $g_{Gimbal_{Friction}}^{CMG_i}(\delta_i) \in \mathbb{R}$  are the applied torque and friction torque of the  $i^{th}$  gimbal. Similarly, the flywheel contributions can be expressed as

$$\begin{aligned} {}^{CMG_i} \dot{h}_{CMG_i}^{CMG_i} \cdot \hat{a}_{W_i} &= \hat{a}_{W_i} \cdot \left[ {}^{CMG_i} I_{CMG_i}^{CMG_i} \left( D_{CMG_i}^T \dot{\omega} + \ddot{\delta}\hat{a}_{G_i} \right) \right] \\ &\quad + \hat{a}_{W_i} \cdot \left[ \left( \omega + \delta\hat{a}_{G_i} \right)^\times h_{G_i} \right] + \hat{a}_{W_i} \cdot {}^{CMG_i} I_{CMG_i}^{CMG_i} \dot{\Omega}_i \hat{a}_{W_i} \\ &= \tau_{Wheel_{motor}}^{CMG_i} - g_{Wheel_{Friction}}^{CMG_i}, \end{aligned} \quad (4-6)$$

where  $\tau_{Wheel_{motor}}^{CMG_i}(t)$ ,  $g_{Wheel_{Friction}}^{CMG_i}(\Omega_i) \in \mathbb{R}$  are the applied torque and friction torque of the  $i^{th}$  wheel. The equations of motion of the gimbal and flywheel in matrix form can be

expressed as

$$\begin{aligned}\ddot{\delta} &= \left([I_G^{CMG}]^d\right)^{-1} \left[A + [I_W]^d [\Omega]^d [\omega_\Delta] + \tau_{Gimbal_{motor}}^{CMG} - g_{Gimbal_{Friction}}^{CMG}\right] \\ \dot{\Omega} &= \left([I_W]^d\right)^{-1} \left[B + \tau_{Wheel_{motor}}^{CMG} - g_{Wheel_{Friction}}^{CMG}\right],\end{aligned}\quad (4-7)$$

where  $A(\omega, \dot{\omega}, \delta), B(\omega, \dot{\omega}, \delta, \dot{\delta}) \in \mathbb{R}^4$  are residual terms obtained by algebraic manipulations of (4-5) and (4-6), and  $[\omega_\Delta(\delta_i)] \in \mathbb{R}^4$  is a vector resulting from  $\hat{a}_{G_i} \cdot \{D_{CMG_i}^T(\delta_i)\omega(t)\}^\times \hat{a}_{W_i}$ ; the inertia matrices  $[I_G^{CMG}]^d, [I_W]^d \in \mathbb{R}^{4 \times 4}$  are  $[I_G^{CMG}]^d \triangleq \text{diag}([I_G^{CMG_1} \quad I_G^{CMG_2} \quad I_G^{CMG_3} \quad I_G^{CMG_4}])$ ,  $[I_W]^d \triangleq \text{diag}([I_{W_1} \quad I_{W_2} \quad I_{W_3} \quad I_{W_4}])$ , where  $[I_G^{CMG}]^d$  is the unknown gimbal inertia matrix, and  $[I_W]^d$  is the known flywheel inertia matrix; the satellite angular velocity  $\omega(t)$  projected to  $\mathcal{B}$  is denoted as  $[\omega_\circ(t)]^d \triangleq \text{diag}([[\omega_{\circ_1}(t) \quad \omega_{\circ_2}(t) \quad \omega_{\circ_3}(t) \quad \omega_{\circ_4}(t)]])$  ( $\circ: G, W, T \in \mathbb{R}^{4 \times 4}$ ) and  $[\cdot]^d$  denotes a diagonal matrix expressed by components of each VSCMG; and  $\dot{\delta}(t), \Omega(t) \in \mathbb{R}^4$  are gimbal rate and flywheel velocity vectors, respectively. In (4-7),  $\tau_{Gimbal_{motor}}^{CMG}(t), \tau_{Wheel_{motor}}^{CMG}(t) \in \mathbb{R}^4$  are the applied control torques, and the friction vectors  $g_{Gimbal_{Friction}}^{CMG}(\dot{\delta}), g_{Wheel_{Friction}}^{CMG}(\Omega) \in \mathbb{R}^4$  are

$$\begin{aligned}g_{Gimbal_{Friction}}^{CMG} &\triangleq F_{dg}\dot{\delta} + F_{sg}\text{sgn}(\dot{\delta}) \\ g_{Wheel_{Friction}}^{CMG} &\triangleq F_{dw}\Omega + F_{sw}\text{sgn}(\Omega),\end{aligned}\quad (4-8)$$

where  $F_{dg}, F_{sg} \in \mathbb{R}^{4 \times 4}$  and  $F_{dw}, F_{sw} \in \mathbb{R}^{4 \times 4}$  are diagonal matrices containing the uncertain dynamic and static friction coefficients for the gimbals and wheels, respectively, and  $\text{sgn}(\cdot) \in \mathbb{R}^4$  denotes a vector form of the standard signum function where the  $\text{sgn}(\cdot)$  is applied to each element of  $\dot{\delta}(t)$  and  $\Omega(t)$ .

#### 4.1.2 Dynamics for a satellite actuated by VSCMGs

The total angular momentum  $H_t(\omega, \dot{\delta}, \Omega) \in \mathbb{R}^3$  of a rigid VSCMG-actuated satellite can be written as

$$H_t = J\omega + C_G [I_G^{CMG}]^d \dot{\delta} + C_W [I_W]^d \Omega \quad (4-9)$$

where the angular momentum of the CMG is expressed in terms of a CMG-fixed basis  $\mathcal{B} = \left\{ \hat{a}_{G_i}, \hat{a}_{W_i}, \hat{a}_{T_i}, \right\}$ ; and  $C_G, C_W(\delta), C_T(\delta) \in \mathbb{R}^{3 \times 4}$  are defined as  $C_G \triangleq \begin{bmatrix} \hat{a}_{G_1} & \hat{a}_{G_2} & \hat{a}_{G_3} & \hat{a}_{G_4} \end{bmatrix}, C_W \triangleq \begin{bmatrix} \hat{a}_{W_1} & \hat{a}_{W_2} & \hat{a}_{W_3} & \hat{a}_{W_4} \end{bmatrix}, C_T \triangleq \begin{bmatrix} \hat{a}_{T_1} & \hat{a}_{T_2} \\ \hat{a}_{T_3} & \hat{a}_{T_4} \end{bmatrix}$ . In (4-9), the uncertain total satellite inertia matrix  $J(\delta) \in \mathbb{R}^{3 \times 3}$  is positive definite and symmetric such that

$$\frac{1}{2} \lambda_{\min} \{J\} \|\xi\|^2 \leq \xi^T J \xi \leq \frac{1}{2} \lambda_{\max} \{J\} \|\xi\|^2 \quad \forall \xi \in \mathbb{R}^n$$

where  $\lambda_{\min} \{J\}, \lambda_{\max} \{J\} \in \mathbb{R}$  are the minimum and maximum principal inertias of  $J(\delta)$  and  $\delta(t) \in \mathbb{R}^4$  is the gimbal angle. The equation of motion for a rigid VSCMG-actuated satellite can be written as

$$\begin{aligned} g_{C_s}^E &= \dot{J}\omega + J\dot{\omega} + \omega^\times J\omega \\ &+ C_G \left( [I_G^{CMG}]^d \ddot{\delta} - [I_W]^d [\omega_T]^d \Omega \right) \\ &+ C_W \left( [I_W]^d \dot{\Omega} + [I_G^{CMG}]^d [\omega_T]^d \dot{\delta} \right) \\ &+ C_T \left( [I_W]^d [\Omega]^d \dot{\delta} + [I_W]^d [\omega_G]^d \Omega - [I_G^{CMG}]^d [\omega_W]^d \dot{\delta} \right), \end{aligned} \quad (4-10)$$

where  $g_{C_s}^E(\omega, \dot{\omega}, \delta, \dot{\delta}, \ddot{\delta}, \Omega, \dot{\Omega}) \in \mathbb{R}^3$  is the external torque applied to the satellite,  $\ddot{\delta}(t), \dot{\Omega}(t) \in \mathbb{R}^4$  are the gimbal acceleration and flywheel acceleration, and  $[\Omega(t)]^d$  and  $[\dot{\delta}(t)]^d$  denote diagonal matrices composed of the vector elements of  $\Omega(t), \dot{\delta}(t) \in \mathbb{R}^4$ , respectively. Based on (4-7) and (4-10), the coupled dynamic equations for a VSCMG-actuated satellite can be represented as

$$\begin{aligned} \ddot{\delta} &= \left( [I_G^{CMG}]^d \right)^{-1} \left[ A + [I_W]^d [\Omega]^d [\omega_\Delta] + \tau_{Gimbal_{motor}}^{CMG} - g_{Gimbal_{Friction}}^{CMG} \right] \\ \dot{\Omega} &= \left( [I_W]^d \right)^{-1} \left[ B + \tau_{Wheel_{motor}}^{CMG} - g_{Wheel_{Friction}}^{CMG} \right] \\ \dot{\omega} &= -J^{-1} \left[ \frac{d}{dt} (J) \omega + \omega^\times J \omega + C_G \left( [I_G^{CMG}]^d \ddot{\delta} - [I_W]^d [\omega_T]^d \Omega \right) \right. \\ &\quad \left. + C_W \left( [I_W]^d \dot{\Omega} + [I_G^{CMG}]^d [\omega_T]^d \dot{\delta} \right) \right. \\ &\quad \left. + C_T \left( [I_W]^d [\Omega]^d \dot{\delta} + [I_W]^d [\omega_G]^d \Omega - [I_G^{CMG}]^d [\omega_W]^d \dot{\delta} \right) \right]. \end{aligned} \quad (4-11)$$

## 4.2 Attitude Control Objective

The attitude control objective is to develop a gimbal rate and flywheel velocity control law to enable the attitude of  $\mathcal{F}_S$  to track the attitude of  $\mathcal{F}_{S_d}$ . The objective is quantified in 3.2.1 in Chapter 3.

## 4.3 Attitude Control Development

To facilitate the design of a composite VSCMG steering law, an auxiliary signal  $r(t) \in \mathbb{R}^3$  is defined as [23]

$$r \triangleq \omega - \tilde{R}\omega_d + \alpha e_v, \quad (4-12)$$

where  $\alpha \in \mathbb{R}$  is a constant control gain. Using (3-7) and (4-12), the angular velocity tracking error can be expressed as

$$\tilde{\omega} = r - \alpha e_v. \quad (4-13)$$

In the absence of external disturbances, the satellite dynamics of (4-10) can be used to rewrite the open-loop error dynamics for  $r(t)$  as

$$J\dot{r} = G + D\dot{\delta} + H\Omega - \frac{1}{2}Jr, \quad (4-14)$$

where the auxiliary terms  $G(e_0, e_v, \omega, \omega_d, \dot{\omega}_d, \delta) \in \mathbb{R}^3$ ,  $D(e_0, e_v, \omega, \omega_d, r, \delta, \Omega) \in \mathbb{R}^{3 \times 4}$ , and  $H(\omega, \delta) \in \mathbb{R}^{3 \times 4}$  are defined as

$$\begin{aligned} G &\triangleq -\omega^\times J\omega + J\omega^\times \tilde{R}\omega_d - J\tilde{R}\dot{\omega}_d + \frac{1}{2}J\alpha(e_v^\times + e_0 I_3)\tilde{\omega}, \\ D &\triangleq -C_W [I_G^{CMG}]^d [\omega_T]^d + C_T [I_G^{CMG}]^d [\omega_W]^d - \frac{\partial J}{\partial \delta} \left( \frac{1}{2}r + \tilde{R}\omega_d - \alpha e_v \right) \\ &\quad - C_T [I_W]^d [\Omega]^d, \\ H &\triangleq C_G [I_W]^d [\omega_T]^d - C_T [I_W]^d [\omega_G]^d, \end{aligned}$$

and the terms  $C_G [I_G^{CMG}]^d \ddot{\delta}(t)$  and  $C_W(\delta) [I_W]^d \dot{\Omega}(t)$  are assumed to be negligible [26, 83, 89]. After some algebraic manipulation, the error dynamics in (4-14) are

$$\begin{aligned} J\dot{r} &= G + D\dot{\delta}_d + H\Omega_d + D\tilde{\delta} + H\tilde{\Omega} - \frac{1}{2}\dot{J}r \\ &= G + Q\eta_d + D\tilde{\delta} + H\tilde{\Omega} - \frac{1}{2}\dot{J}r, \end{aligned} \quad (4-15)$$

where  $Q(e_0, e_v, r, \omega, \delta, \Omega) \triangleq \begin{bmatrix} D(e_0, e_v, r, \omega, \delta, \Omega) & H(\omega, \delta) \end{bmatrix} \in \mathbb{R}^{3 \times 8}$ ,  $\eta_d(t) \triangleq \begin{bmatrix} \dot{\delta}_d^T & \Omega_d^T \end{bmatrix}^T \in \mathbb{R}^8$ , and the backstepping errors  $\tilde{\delta}(t), \tilde{\Omega}(t) \in \mathbb{R}^4$  are defined as

$$\tilde{\delta} \triangleq \delta - \delta_d, \quad \tilde{\Omega} \triangleq \Omega - \Omega_d. \quad (4-16)$$

Based on the error dynamics of (4-15), the auxiliary backstepping input  $Q(e_0, e_v, r, \omega, \delta, \Omega) \eta_d(t)$  is designed as

$$Q\eta_d = -G - k_1 r - e_v, \quad (4-17)$$

where  $k_1 \in \mathbb{R}$  is a positive constant gain. Substituting (4-17) into (4-15), the closed-loop error dynamics for  $r(t)$  can be determined as

$$J\dot{r} = D\tilde{\delta} + H\tilde{\Omega} - \frac{1}{2}\dot{J}r - k_1 r - e_v. \quad (4-18)$$

In addition to attitude control, the control development also targets reduced power consumption during flywheel despinning. The flywheel can achieve deceleration by null motion control. To facilitate the development of a null motion controller, the new composite VSCMG steering law in (4-17) is expressed as

$$\begin{aligned} \eta_d &= -Q_w^+(G + k_1 r + e_v) - (I_8 - Q_w^+Q) S\sigma \\ &= \begin{bmatrix} -R_1 - N_1 \bar{s}_g k_\gamma \frac{\partial \gamma}{\partial \delta} \\ -R_2 - N_2 \bar{s}_w g \end{bmatrix}, \end{aligned} \quad (4-19)$$

where  $Q_w^+(e_0, e_v, r, \omega, \delta, \Omega) \triangleq W(\delta) Q^T(\cdot) \{Q(\cdot) W(\delta) Q^T(\cdot)\}^{-1}$ , and  $W(\delta) \in \mathbb{R}^{8 \times 8}$  denotes a mode weight matrix that determines whether the VSCMGs system operates in a CMG

mode or a RW mode, and  $S(\delta) \in \mathbb{R}^{8 \times 8}$  is a null motion weight [45, 46] to arbitrate the null motion  $\sigma(t) \in \mathbb{R}^{8 \times 1}$  of the gimbal and flywheel defined as

$$\sigma \triangleq \begin{bmatrix} k_\gamma \frac{\partial \gamma}{\partial \delta} \\ g \end{bmatrix}, \quad (4-20)$$

where the null motion  $\sigma(t)$  generates gimbal reconfiguration and wheel deceleration,  $k_\gamma \in \mathbb{R}$  denotes a positive constant, and  $g(t)$  is an auxiliary control signal to track the desired flywheel speed trajectory. In the partitioned steering law of (4-19),  $R_i(e_0, e_v, r, \omega, \delta, \Omega) = [Q_w^+(\cdot) \{G(e_0, e_v, r, \omega, \delta) + k_1 r(t) + e_v(t)\}]_i$  indicates components of each  $\mathbb{R}^4$  term,  $N_i(e_0, e_v, r, \omega, \delta, \Omega) \in \mathbb{R}^{4 \times 8}$  is the projector onto  $\mathcal{N}(Q)$ , and  $\bar{s}_g(\delta), \bar{s}_w(\delta) \in \mathbb{R}^{8 \times 4}$  are composed of components  $s_g, s_w \in \mathbb{R}^{4 \times 4}$  of null motion weight  $S(\delta)$ , defined as

$$\bar{s}_g \triangleq \begin{bmatrix} s_g & 0_{4 \times 4} \end{bmatrix}^T \quad \bar{s}_w \triangleq \begin{bmatrix} 0_{4 \times 4} & s_w \end{bmatrix}^T.$$

The mode weight matrix  $W(\delta) \in \mathbb{R}^{8 \times 8}$  is designed as [87, 89, 101]

$$W \triangleq \begin{bmatrix} W_\delta I_{4 \times 4} & 0_{4 \times 4} \\ 0_{4 \times 4} & W_\Omega I_{4 \times 4} \end{bmatrix}, \quad (4-21)$$

where  $W_\Omega(\delta)$  is defined as

$$W_\Omega \triangleq W_{\Omega 0} \exp(\lambda_1 f),$$

where  $\lambda_1, W_{\Omega 0}, W_\delta \in \mathbb{R}$  are positive constants, and the singularity measuring objective function  $f(\delta)$  is

$$f = -\det(C_T C_T^T). \quad (4-22)$$

The control input  $g(t)$  of (4-20) is designed as

$$g = -[N_2 \bar{s}_w]^{-1} (R_2 + \Omega_f), \quad (4-23)$$

where  $\Omega_f(t) \in \mathbb{R}^4$  is a desired, given flywheel deceleration trajectory. In a stationary state after completing an arbitrary attitude maneuver, the wheels do not need to maintain

high speeds. Decelerating the wheels can reduce the potential for wheel speed saturation, but typical strategies require battery power to decelerate the wheels while maintaining a desired attitude. The auxiliary control input  $g(t)$  results from an internal momentum management strategy that enables internal friction to be used along with null space motion as a power reduction method to decelerate the flywheels while maintaining a desired attitude.

**Remark 4.1.** *The bracketed term in (4-23) is invertible, and simultaneous attitude and wheel deceleration is possible when  $N_2(\cdot) \bar{s}_w(\delta) = (I_8 - Q_w^+(\cdot) Q(\cdot))_{4 \times 8} \bar{s}_w(\delta) \neq 0_{4 \times 4}$ . Since  $(I_8 - Q_w^+(\cdot) Q(\cdot))_{4 \times 8}$  is nonzero for all  $Q(\cdot)$ ,  $N_2(\cdot) \neq 0_{4 \times 8}$  and simultaneous attitude and wheel deceleration can be achieved provided*

$$\bar{s}_w \neq 0 \text{ and } \bar{s}_w \notin \mathcal{N}(N_2),$$

where  $\mathcal{N}(N_2(\cdot))$  denotes the null space of the matrix  $N_2(\cdot)$ . Hence,  $\bar{s}_w(\delta) \notin \mathcal{N}(N_2)$  except when  $\bar{s}_w(\delta) = 0_{8 \times 4}$ , which means the CMG's Jacobian itself is singular, which does not occur unless it is initially singular. Accordingly, as long as the system does not start in a singular configuration, the control input  $g(t)$  exists and simultaneous attitude and wheel deceleration can be achieved.

The composite steering law in (4-19) has an extra degree of freedom resulting from the variable speed flywheel, enabling the VSCMG system to escape an elliptic singularity and a gimbal lock singularity [89, 100]. Since the steering law of (4-19) is produced by four VSCMG units, (4-19) is also a solution to an underdetermined system containing four gimbal rates and four flywheel velocities as unknowns [55, 89, 100]. In (4-19), the term  $(I_8 - Q_w^+(\cdot) Q(\cdot)) S(\delta) \sigma(t)$  generates the VSCMG null motion for singularity avoidance and wheel deceleration. The singularity avoidance method reduces/eliminates the usage of RW mode in continuous manner when encountering elliptic/hyperbolic singularity. Since  $Q(\cdot)$  is nonsquare, the pseudo-inverse  $Q_w^+(\cdot) \in \mathbb{R}^{8 \times 3}$  is defined so that  $Q(\cdot) Q_w^+(\cdot) = I_3$ , and the matrix  $I_8 - Q_w^+(\cdot) Q(\cdot)$ , which projects vectors onto the null space of  $Q(\cdot)$ , satisfies

the properties

$$(I_8 - Q_w^+ Q) (I_8 - Q_w^+ Q) = I_8 - Q_w^+ Q \quad (4-24a)$$

$$Q (I_8 - Q_w^+ Q) = 0_{3 \times 8}. \quad (4-24b)$$

The composite VSCMG steering law in (4-19) provides a desired gimbal and flywheel velocity. Since the actual control inputs are gimbal and flywheel torques, a backstepping approach is used to design  $\tau_{Gimbal_{motor}}^{CMG}(t)$  and  $\tau_{Wheel_{motor}}^{CMG}(t)$  by examining the open-loop error system for the mismatch between the desired and actual gimbal and flywheel velocities, denoted by the backstepping errors  $\tilde{\delta}(t)$ ,  $\tilde{\Omega}(t)$ . Specifically, after using (4-7) and (4-17) and performing some algebraic manipulation, the open-loop error system for  $\tilde{\delta}(t)$ ,  $\tilde{\Omega}(t)$  is

$$\begin{aligned} \dot{\tilde{\delta}} &= \left( [I_G^{CMG}]^d \right)^{-1} \left[ A + [I_W]^d [\Omega]^d [\omega_\Delta] + \tau_{Gimbal_{motor}}^{CMG} - g_{Gimbal_{Friction}}^{CMG} \right] + D^+ \left( \dot{D} \tilde{\delta}_d + \dot{G} + k_1 \dot{r} \right) \\ \dot{\tilde{\Omega}} &= \left( [I_W]^d \right)^{-1} \left[ B + \tau_{Wheel_{motor}}^{CMG} - g_{Wheel_{Friction}}^{CMG} \right] + H^+ \left( \dot{H} \Omega_d + \dot{e}_v \right), \end{aligned} \quad (4-25)$$

where

$$\begin{aligned} \dot{G} &\triangleq -\dot{\omega}^\times J \omega - \omega^\times \left( \dot{J} \omega + J \dot{\omega} \right) + \left( \dot{J} \omega + J \dot{\omega} \right)^\times \tilde{R} \omega_d + J \omega^\times \left( \dot{\tilde{R}} \omega_d + \tilde{R} \dot{\omega}_d \right) \\ &\quad - \dot{J} \tilde{R} \dot{\omega}_d - J \tilde{R} \ddot{\omega}_d - J \tilde{R} \ddot{\omega}_d + \frac{1}{2} \alpha \left[ \left( \dot{J} e_v + J \dot{e}_v \right)^\times \tilde{\omega} + J e_v^\times \dot{\tilde{\omega}} \right. \\ &\quad \left. + \left( \dot{J} e_0 I_3 + J \dot{e}_0 I_3 \right) \tilde{\omega} + J e_0 I_3 \dot{\tilde{\omega}} \right], \\ \dot{D} &\triangleq -C_T \left[ \dot{\delta} \right]^d [I_G^{CMG}]^d [\omega_T]^d - C_W [I_G^{CMG}]^d [\dot{\omega}_T]^d \\ &\quad - C_W \left[ \dot{\delta} \right]^d [I_G^{CMG}]^d [\omega_W]^d + C_T [I_G^{CMG}]^d [\dot{\omega}_W]^d \\ &\quad - \frac{\partial^2 J}{\partial \delta^2} \dot{\delta} \left( \frac{1}{2} r + \tilde{R} \omega_d - \alpha e_v \right) - \frac{\partial J}{\partial \delta} \left( \frac{1}{2} \dot{r} + \dot{\tilde{R}} \omega_d + \tilde{R} \dot{\omega}_d - \alpha \dot{e}_v \right) \\ &\quad + C_W \left[ \dot{\delta} \right]^d [I_W]^d [\Omega]^d - C_T [I_W]^d \left[ \dot{\Omega} \right]^d, \\ \dot{H} &\triangleq C_G [I_W]^d [\dot{\omega}_T]^d - \frac{\partial}{\partial \delta} (C_T) \dot{\delta} [I_W]^d [\omega_G]^d - C_T [I_W]^d [\dot{\omega}_G]^d. \end{aligned}$$

The internal frictions  $g_{GimbalFriction}^{CMG}(\dot{\delta})$  and  $g_{WheelFriction}^{CMG}(\Omega)$  in (4-25) are parameterized in terms of known regression matrices  $Y_1(\dot{\delta}), Y_2(\Omega) \in \mathbb{R}^{4 \times 8}$  and vectors of eight unknown constants  $\theta_1, \theta_2 \in \mathbb{R}^8$  as

$$Y_1 \theta_1 \triangleq F_{dg} \dot{\delta} + F_{sg} \text{sgn}(\dot{\delta}) \quad Y_2 \theta_2 \triangleq F_{dw} \Omega + F_{sw} \text{sgn}(\Omega).$$

Based on the open-loop error dynamics of (4-25), the applied control torques  $\tau_{GimbalMotor}^{CMG}(t)$  and  $\tau_{WheelMotor}^{CMG}(t)$  are designed as

$$\begin{aligned} \tau_{GimbalMotor}^{CMG} &= -A - [I_W]^d [\Omega]^d [\omega_\Delta] + Y_1 \hat{\theta}_1 - [I_G^{CMG}]^d \left\{ D^+ \left( \dot{D} \delta_d + \dot{G} + k_1 \dot{r} \right) \right\} \\ &\quad - [I_G^{CMG}]^d D^T r - k_2 [I_G^{CMG}]^d \tilde{\delta} \\ \tau_{WheelMotor}^{CMG} &= -B + Y_2 \hat{\theta}_2 - [I_W]^d \left\{ H^+ \left( \dot{H} \Omega_d + \dot{e}_v \right) \right\} - [I_W]^d H^T r - k_3 [I_W]^d \tilde{\Omega}, \end{aligned} \quad (4-26)$$

where  $k_2, k_3 \in \mathbb{R}$  are positive constant gains, and  $\hat{\theta}_1(t), \hat{\theta}_2(t) \in \mathbb{R}^8$  are estimates for the parametric uncertainty  $F_{dg}, F_{sg}, F_{dw}$ , and  $F_{sw}$ . The parameter update laws for  $\hat{\theta}_1(t), \hat{\theta}_2(t)$  are designed as

$$\begin{aligned} \dot{\hat{\theta}}_1 &= -\Gamma_1 Y_1^T \left( [I_G^{CMG}]^d \right)^{-1} \tilde{\delta} \\ \dot{\hat{\theta}}_2 &= -\Gamma_2 Y_2^T \left( [I_W]^d \right)^{-1} \tilde{\Omega}, \end{aligned} \quad (4-27)$$

where  $\Gamma_1, \Gamma_2 \in \mathbb{R}^{8 \times 8}$  denote constant, positive-definite, diagonal adaptation gain matrices. After substituting the control torques of (4-26) into (4-25), the closed-loop error dynamics for  $\tilde{\delta}(t), \tilde{\Omega}(t)$  are

$$\begin{aligned} \dot{\tilde{\delta}} &= -D^T r - k_2 \tilde{\delta} - \left( [I_G^{CMG}]^d \right)^{-1} Y_1 \tilde{\theta}_1 \\ \dot{\tilde{\Omega}} &= -H^T r - k_3 \tilde{\Omega} - \left( [I_W]^d \right)^{-1} Y_2 \tilde{\theta}_2, \end{aligned} \quad (4-28)$$

where  $\tilde{\theta}_1(t), \tilde{\theta}_2(t) \in \mathbb{R}^8$  are defined as

$$\tilde{\theta}_1 \triangleq \theta_1 - \hat{\theta}_1, \quad \tilde{\theta}_2 \triangleq \theta_2 - \hat{\theta}_2. \quad (4-29)$$

### 4.3.1 Stability Analysis

**Theorem 4.1.** *The weighted steering law (4-19) including the gimbal rate and the flywheel velocity, and the applied control torques (4-26) along with the adaptive update laws given in (4-27) ensure global asymptotic attitude tracking in the sense that*

$$\|e_v(t)\| \rightarrow 0 \quad \text{as} \quad t \rightarrow \infty. \quad (4-30)$$

*Proof:* To prove the attitude tracking result, let  $\mathcal{D} \subset \mathbb{R}^{31}$  be a domain containing  $\rho(e_v, e_0, r, \tilde{\delta}, \tilde{\Omega}, \tilde{\theta}_1, \tilde{\theta}_2) = 0_{31}$ , where  $\rho(e_v, e_0, r, \tilde{\delta}, \tilde{\Omega}, \tilde{\theta}_1, \tilde{\theta}_2) \in \mathbb{R}^{31}$  is defined as

$$\rho \triangleq \begin{bmatrix} e_v^T & e_0 & r^T & \tilde{\delta}^T & \tilde{\Omega}^T & \tilde{\theta}_1 & \tilde{\theta}_2 \end{bmatrix}^T.$$

Let  $V(\rho) : \mathcal{D} \times [0, \infty) \rightarrow \mathbb{R}$  denote a continuously differentiable, positive definite function defined as

$$V = e_v^T e_v + (1 - e_0)^2 + \frac{1}{2} r^T J r + \frac{1}{2} \tilde{\delta}^T \tilde{\delta} + \frac{1}{2} \tilde{\Omega}^T \tilde{\Omega} + \frac{1}{2} \tilde{\theta}_1^T \Gamma_1^{-1} \tilde{\theta}_1 + \frac{1}{2} \tilde{\theta}_2^T \Gamma_2^{-1} \tilde{\theta}_2, \quad (4-31)$$

After differentiating (4-31) and using (4-11), (3-17), (4-18), and (4-28), the resulting expression is given as

$$\begin{aligned} \dot{V} &= e_v^T (e_v^\times + e_0 I_3) \tilde{\omega} + (1 - e_0) e_v^T \tilde{\omega} + r^T \left( D \tilde{\delta} + H \tilde{\Omega} - \frac{1}{2} \dot{J} r - k_1 r - e_v \right) \\ &\quad + \tilde{\delta}^T \left( -D^T r - k_2 \tilde{\delta} - \left( [I_G^{CMG}]^d \right)^{-1} Y_1 \tilde{\theta}_1 \right) + \tilde{\Omega}^T \left( -H^T r - k_3 \tilde{\Omega} - \left( [I_W]^d \right)^{-1} Y_2 \tilde{\theta}_2 \right) \\ &\quad - \tilde{\theta}_1^T \Gamma_1^{-1} \dot{\tilde{\theta}}_1 - \tilde{\theta}_2^T \Gamma_2^{-1} \dot{\tilde{\theta}}_2. \end{aligned} \quad (4-32)$$

After performing some algebraic manipulations, and using (4-13), (4-27) and exploiting the fact that  $e_v^T e_v^\times \tilde{\omega} = 0$ , the expression in (4-32) can be upper bounded as

$$\dot{V} \leq -\lambda \|z\|^2, \quad (4-33)$$

where  $\lambda = \lambda_{\min} \{ \alpha, k_1, k_2, k_3 \} \in \mathbb{R}$  and  $z(e_v, r, \tilde{\delta}, \tilde{\Omega}) \in \mathbb{R}^{14}$  is defined as

$$z \triangleq \begin{bmatrix} e_v^T & r^T & \tilde{\delta}^T & \tilde{\Omega}^T \end{bmatrix}^T. \quad (4-34)$$

From (4-31) and (4-33),  $r(e_v, e_0, \omega), e_v(t), \tilde{\delta}(t), \tilde{\Omega}(t), \hat{\theta}_1(t), \hat{\theta}_2(t) \in \mathcal{L}_\infty$ . Thus, from (6-8), (4-13), and (4-34),  $e_v(t), e_0(t), \tilde{\omega}(t), z(e_v, r, \tilde{\delta}, \tilde{\Omega}) \in \mathcal{L}_\infty$ , and (4-12) can be used to conclude that  $\omega(t) \in \mathcal{L}_\infty$ . The open-loop quaternion tracking error in (3-17) can be used to conclude that  $\dot{e}_v(t), \dot{e}_0(t) \in \mathcal{L}_\infty$ . The fact that  $\delta(t)$ -dependent functions result from direction cosine matrices indicates that the functions contain  $\delta(t)$  within bounded trigonometric functions. Since  $e_v(t), e_0(t), r(e_v, e_0, \omega), \omega(t), \Omega(t) \in \mathcal{L}_\infty$ , (4-19) can be used to show that  $\dot{\delta}_d(t), \Omega_d \in \mathcal{L}_\infty$ . Through (4-16) and  $\tilde{\delta}(t), \dot{\delta}_d(t), \tilde{\Omega}(t), \Omega_d(t) \in \mathcal{L}_\infty$ , then  $\dot{\delta}(t), \Omega(t) \in \mathcal{L}_\infty$ . The fact that  $r(e_v, e_0, \omega), e_v(t), e_0(t), \omega(t), \Omega(t), \tilde{\delta}(t), \tilde{\Omega}(t), \dot{\delta}(t) \in \mathcal{L}_\infty$  can be used with (4-18) to conclude that  $\dot{r}(e_v, e_0, r, \dot{\delta}, \tilde{\delta}, \tilde{\Omega}) \in \mathcal{L}_\infty$ . The time derivative of (4-12) shows that  $\dot{\omega}(t) \in \mathcal{L}_\infty$  with  $\omega(t), e_v(t), \dot{e}_v(t), e_0(t), \omega_d(t), \dot{\omega}_d(t) \in \mathcal{L}_\infty$ . From (4-29),  $\hat{\theta}_1(t), \hat{\theta}_2(t) \in \mathcal{L}_\infty$ . In (4-26),  $\tau_{Wheel_{motor}}^{CMG}(t) \in \mathcal{L}_\infty$  based on the fact that  $\omega(t), \dot{\omega}(t), \dot{\delta}(t), \Omega_d(t), \tilde{\Omega}(t), r(e_v, e_0, \omega), \dot{e}_v(t), \hat{\theta}_2(t) \in \mathcal{L}_\infty$ . From the fact that  $\omega(t), \dot{\omega}(t), \dot{\delta}(t), \Omega(t), \tau_{Wheel_{motor}}^{CMG}(t) \in \mathcal{L}_\infty$ , (4-7) indicates that  $\dot{\Omega}(t) \in \mathcal{L}_\infty$ . In (4-26),  $\tau_{Gimbal_{motor}}^{CMG}(t) \in \mathcal{L}_\infty$  based on the fact that  $\omega(t), \dot{\omega}(t), \dot{\delta}(t), \dot{\delta}_d(t), \tilde{\delta}(t), \Omega(t), \dot{\Omega}(t), r(e_v, e_0, \omega), \dot{r}(e_v, e_0, r, \dot{\delta}, \tilde{\delta}, \tilde{\Omega}), e_v(t), \dot{e}_v(t), \hat{\theta}_1(t) \in \mathcal{L}_\infty$ . Under (4-7) and the fact that  $\omega(t), \dot{\omega}(t), \dot{\delta}(t), \Omega(t), \tau_{Gimbal_{motor}}^{CMG}(t) \in \mathcal{L}_\infty, \ddot{\delta}(t) \in \mathcal{L}_\infty$ . From (4-7) and (4-28), it is said that  $\ddot{\delta}(t), \ddot{\Omega}(t) \in \mathcal{L}_\infty$ . Standard signal chasing arguments can then be utilized to prove that all remaining signals are bounded during closed-loop operation. The fact that  $e_v(t), r(e_v, e_0, \omega), \dot{e}_v(t), \dot{r}(e_v, e_0, r, \dot{\delta}, \tilde{\delta}, \tilde{\Omega}), \tilde{\delta}(t), \tilde{\Omega}(t), \dot{\delta}(t), \dot{\Omega}(t) \in \mathcal{L}_\infty$  is sufficient to show that  $e_v(t), r(e_v, e_0, \omega), \tilde{\delta}(t)$ , and  $\tilde{\Omega}(t)$  are uniformly continuous. Since  $e_v(t), r(t), \tilde{\delta}(t)$ , and  $\tilde{\Omega}(t)$  are uniformly continuous,  $e_v(t), r(e_v, e_0, \omega), \tilde{\delta}(t), \tilde{\Omega}(t) \in \mathcal{L}_\infty \cap \mathcal{L}_2$  from (4-33), Barbalat's Lemma can be used to prove  $e_v(t), r(e_v, e_0, \omega), \tilde{\delta}(t), \tilde{\Omega}(t) \rightarrow 0$  as  $t \rightarrow \infty$ . ■

## 4.4 Simulation Study

### 4.4.1 Simulation Setup

Numeric simulations are presented to examine the performance of the developed controller. Parameters used for the satellite are based on a high fidelity model and are given in Table 4-1. The desired angular velocity trajectories  $\omega_d(t)$  are  $\omega_d(t) = \begin{bmatrix} 0.05 \sin(2\pi t/3000) & 0 & 0 \end{bmatrix} (rad/sec)$  and the desired decreasing flywheel speed trajectory for each wheel is designed

$$\Omega_f = (\Omega_{in} - \Omega_{fi}) \exp(-ct) + \Omega_{fi}, \quad (4-35)$$

where  $c$  is a coefficient that can determine a degree of deceleration,  $\Omega_{in}$  is an initial desired flywheel speed and is set as  $50 \text{ rad/s}$  ( $\approx 500 \text{ rpm}$ ), and  $\Omega_{fi}$  is a final desired flywheel speed and is set as  $10 \text{ rad/s}$  ( $\approx 100 \text{ rpm}$ ). The initial conditions are given in Table 4-2.

Physical Parameter	Value
$J(0) (kg \cdot m^2)$	$diag \{ 6.10 \times 10^{-2} \quad 6.10 \times 10^{-2} \quad 7.64 \times 10^{-2} \}$
$m_{cmg} (kg)$	0.165
$I_G (kg \cdot m^2)$	$2.80 \times 10^{-3} I_4$
$I_W (kg \cdot m^2)$	$6.95 \times 10^{-4} I_4$
$skewangle (^\circ)$	54.74

Table 4-1. Physical parameters for the VSCMG simulation.

Initial Parameter	Value
$q(0)$	$[ 0.1 \quad 0.3 \quad 0.8 \quad 0.4 ]$
$\omega(0) (rad/s)$	0
$\hat{\theta}_1(0), \hat{\theta}_2(0)$	0.02, 0
$\delta(0) (rad)$	$[ -1.3352 \quad 0 \quad -1.3352 \quad 0 ]$
$\Omega(0) (rad/s)$	50

Table 4-2. Initial parameters for the VSCMG simulation.

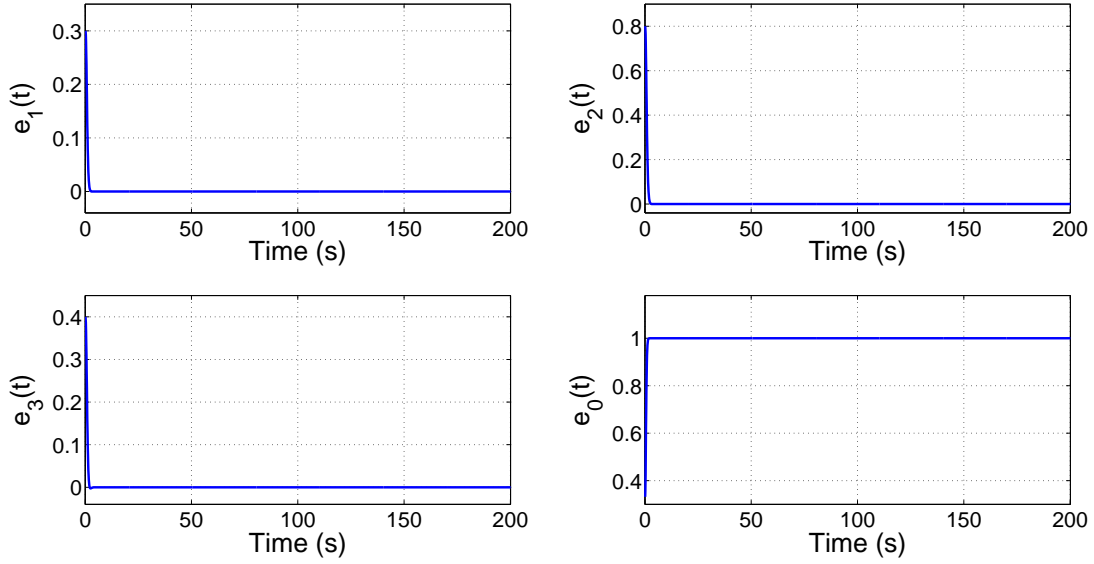


Figure 4-1. Quaternion tracking error  $e(t)$  during closed-loop operation.

#### 4.4.2 Simulation Results

Figures 4-1 - 4-11 show the simulation results of the closed-loop system to achieve the control objective denoted in (3-6) during a 200s simulation period. Figure 4-1 shows the quaternion tracking error results during the entire 200s. Figure 4-2 shows the actual gimbal rates  $\dot{\delta}(t)$  and the actual wheel velocities  $\Omega(t)$ . Figure 4-4 depicts  $f$ ,  $S$ ,  $W$ , which indicate the singularity measure, the null motion weight, and the mode weight, respectively. Based on the singularity measure,  $f$ ,  $S$  and  $W$  generate specific values to properly perform their dual tasks for the VSCMG. For a normal environment, the mode weight  $W$  allows the VSCMG to be a conventional CMG so that it can take advantage of a torque amplification as  $W_{\delta}$  has a bigger value than  $W_{\Omega}$  as seen by Figure 4-4. Only when encountering a singularity above an acceptable level,  $W_{\Omega}$  becomes bigger than  $W_{\delta}$ . Additional solutions provided by the VSCMG as an underdetermined system brings about additional null solutions which enable wheel deceleration. Hence, to use both null motion benefits such as gimbal reconfiguration and wheel deceleration, the null motion weight  $S$  is introduced. Corresponding to the variation of  $f$ ,  $s_g$  generates proper gimbal reconfiguration and  $s_w$  allows steady wheel deceleration depicted in Figure 4-5. For the

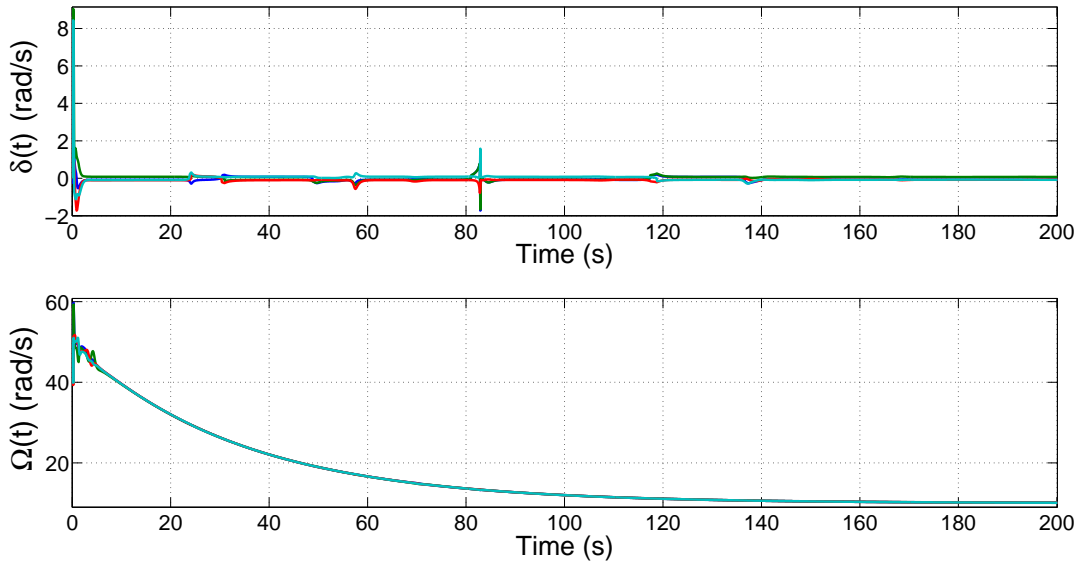


Figure 4-2. Actual control input gimbal rates  $\dot{\delta}(t)$  and flywheel speeds  $\Omega(t)$ .

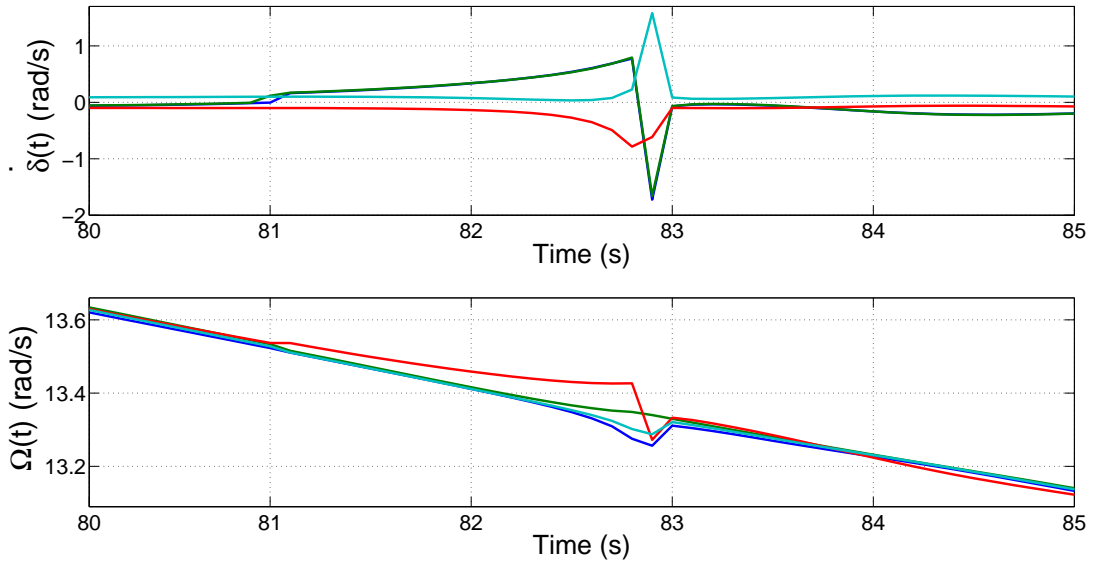


Figure 4-3. Close-up of actual control input gimbal rates  $\dot{\delta}(t)$  and wheel speeds  $\Omega(t)$  when encountering extreme singularity.

null motions, the role of null motion weight  $S$  shown in Figure 4-4 becomes remarkable because the  $S$  can inhibit the wheel deceleration when the CMGs Jacobian approaches singularity so that the flywheel can work in RW mode. Although  $S$  cannot distinguish between different singularities, the weight matrix can adjust the intervention of the flywheel when approaching a singularity. Hence, the composite weighted steering law in (4-19) can cope with an elliptic singularity while maintaining precision attitude control since the steering law generates the required torque in RW mode to pass through or escape an internal singularity differently from the singularity escape methods for CMGs that require added torque [6, 27, 64, 77, 95, 97]. This observation indicates a benefit that results from the extra controllable degree of freedom of the VSCMG. Specifically,  $s_w$  depicted in Figure 4-4 allows wheel deceleration when in normal operation and restricts the wheel deceleration when approaching a singularity. Thus, in most regions gimbal reconfiguration is responsible for singularity avoidance by exploiting gimbal rate null solution. The null motion weight  $S$  serves as a switch that acts as an alternative to cope with both elliptic and hyperbolic singularities while achieving wheel deceleration. The extreme singularity encounter during 80 – 85s shown in Figure 4-4 causes the wheel torque generation to escape the singularity as seen in Figure 4-3. Such singularity escape is considered as an advantage resulting from an extra DOF of the VSCMGs but not possible in the conventional CMG. The time variation of the adaptive parameter estimates is shown in Figures 4-6 and 4-7 which shows the elements of the adaptive parameter vectors  $\hat{\theta}_1(t)$  and  $\hat{\theta}_2(t)$ . In Figures 4-8 and 4-10, the friction torque consisting of the dynamic friction and the static friction denoted in (4-8) have a steady impact on the entire system. The absolute value of the gimbal torque in Figure 4-9 indicates consistent performance despite the uncertain friction effects. The wheel torque in Figure 4-11 induced by the wheel deceleration shows the input power reduction effect in that the wheels have more torques added by both the dynamic and static friction. Such effect can yield total power reduction by attitude control system (ACS).

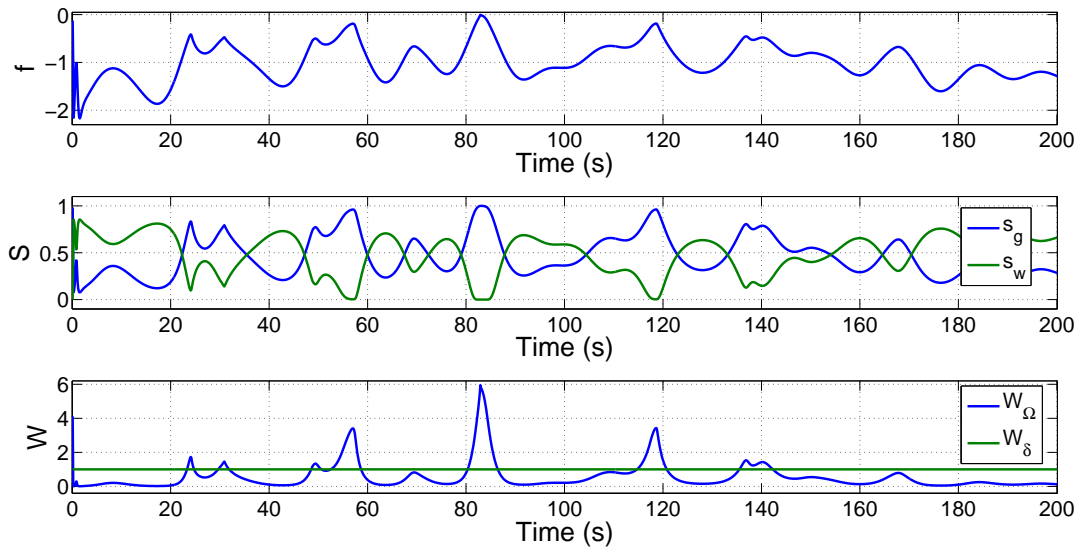


Figure 4-4. Singularity measure function  $f(\delta)$ , null motion switch  $S(\delta)$ , and weight function  $W(\delta)$ .

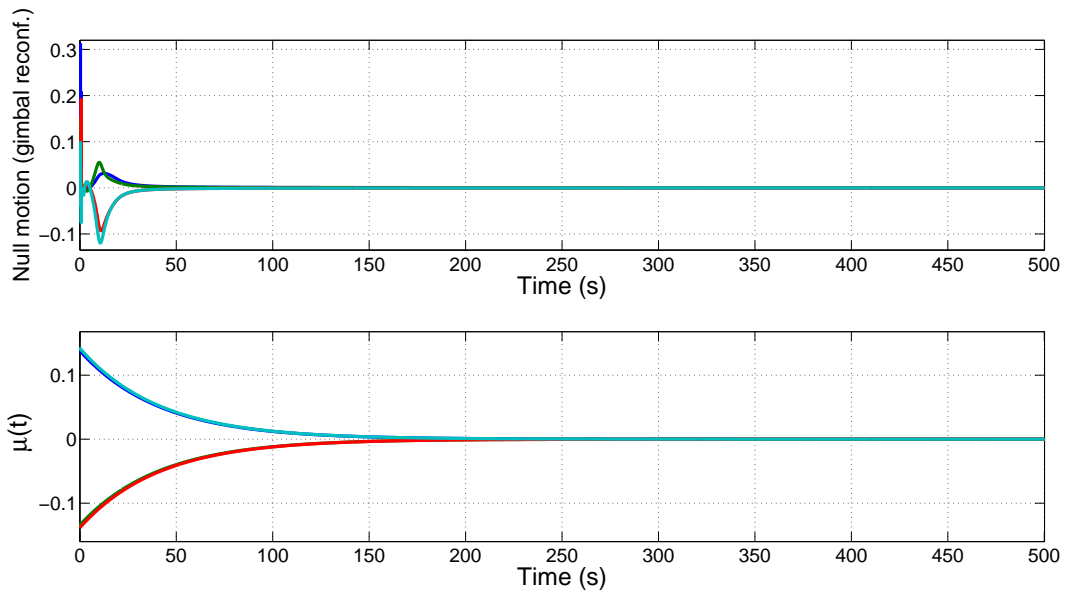


Figure 4-5. Null motion: gimbal reconfiguration and wheel deceleration error  $\mu(t)$ .

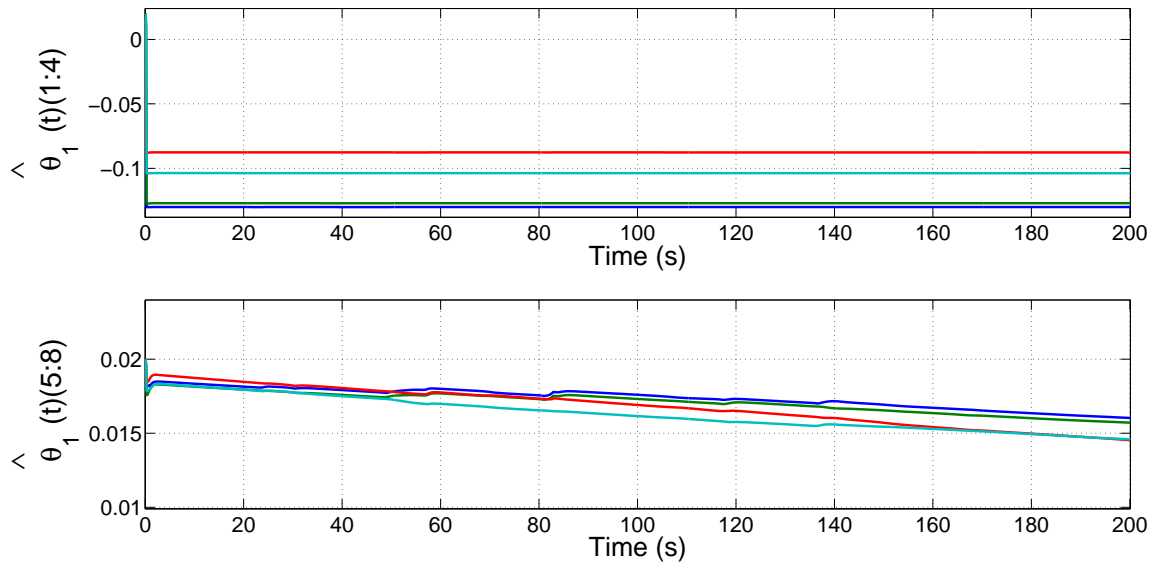


Figure 4-6. Adaptive parameter estimates  $\hat{\theta}_1(t)$  during closed-loop operation.  
 The notation  $\hat{\theta}_1(t)(x)$  denotes the  $x$ -element of  $\hat{\theta}_1(t)$ .

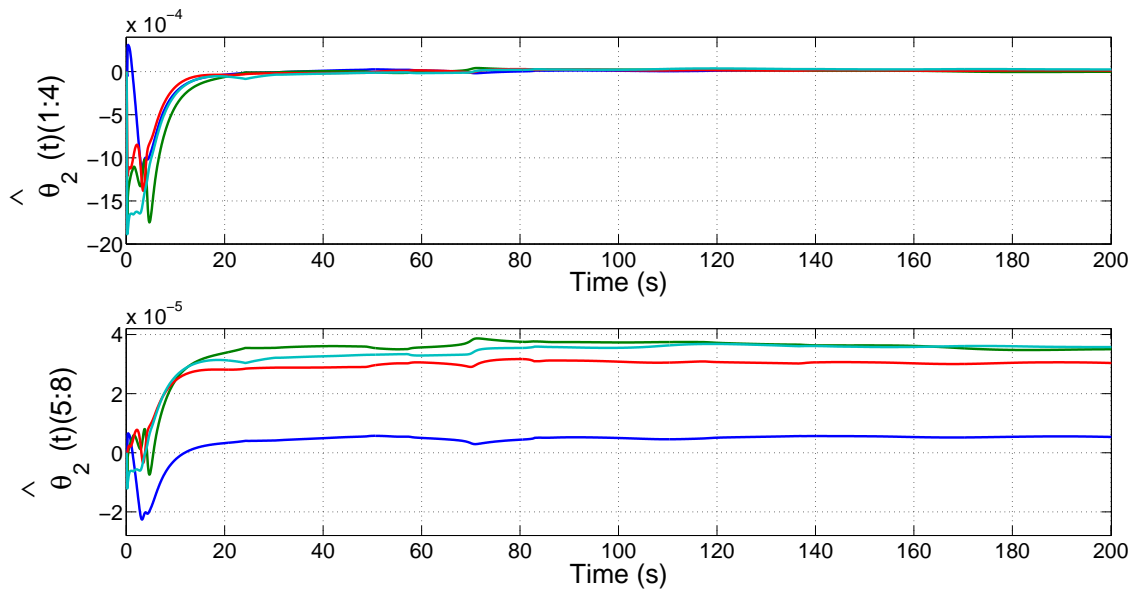


Figure 4-7. Adaptive parameter estimates  $\hat{\theta}_2(t)$  during closed-loop operation.  
 The notation  $\hat{\theta}_2(t)(x)$  denotes the  $x$ -element of  $\hat{\theta}_2(t)$ .

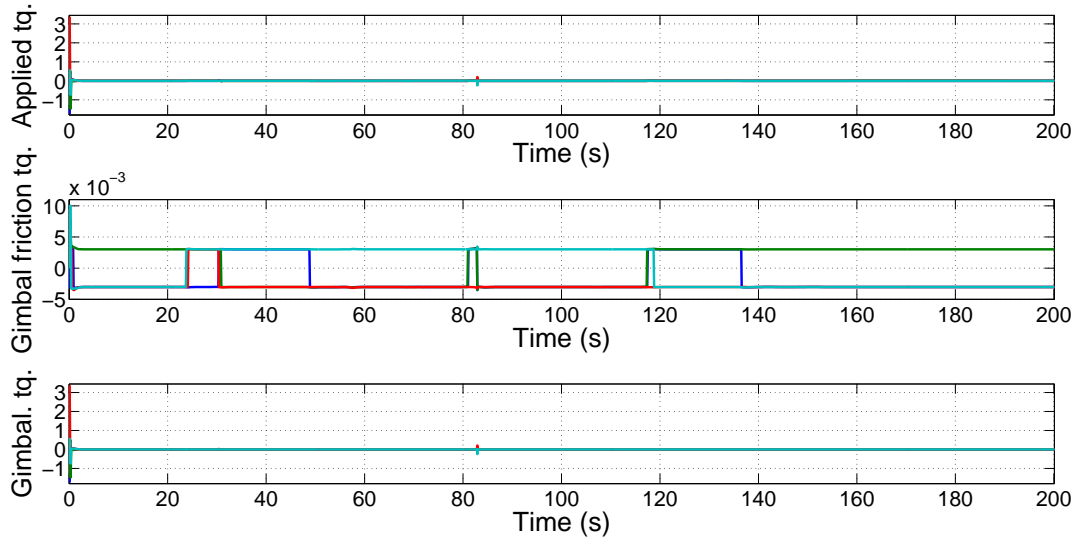


Figure 4-8. Applied gimbal torque, gimbal friction torque, and total gimbal torque during closed-loop controller operation.

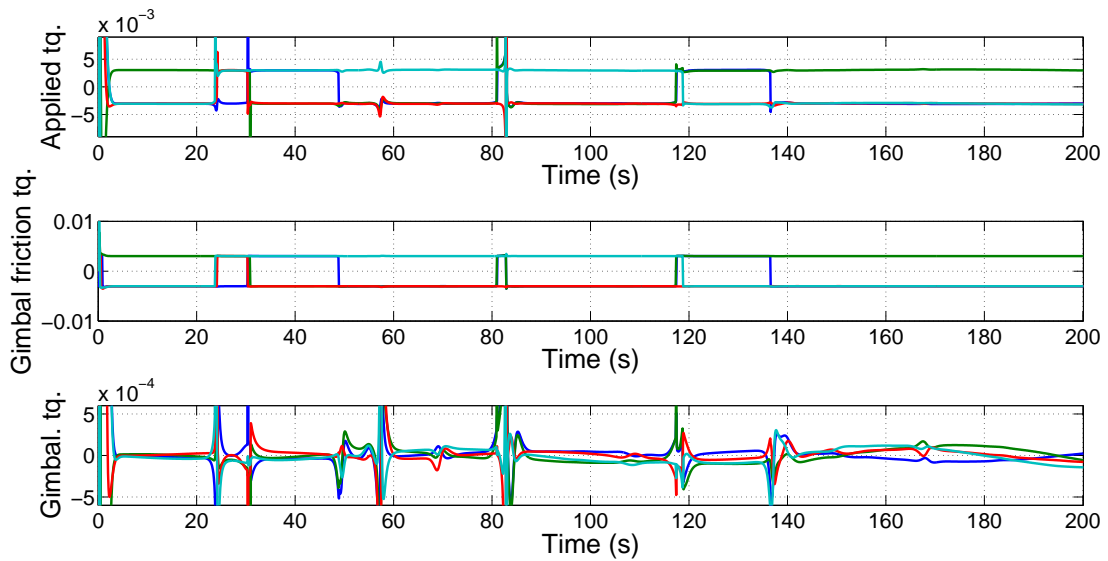


Figure 4-9. Close-up of applied gimbal torque, gimbal friction torque, and total gimbal torque during the entire closed-loop operation.

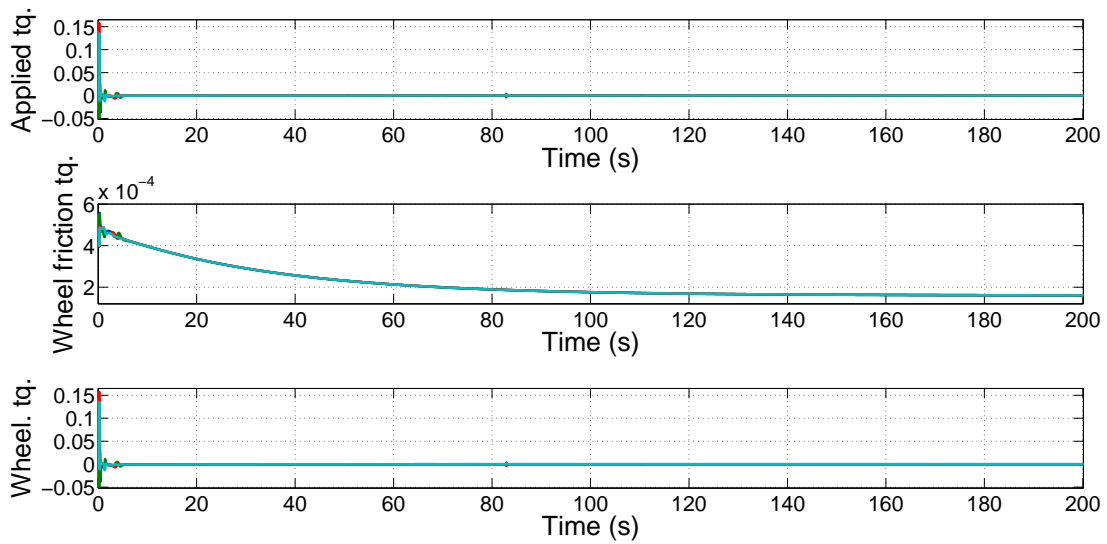


Figure 4-10. Applied wheel torque, wheel friction torque, and total wheel torque during closed-loop controller operation.

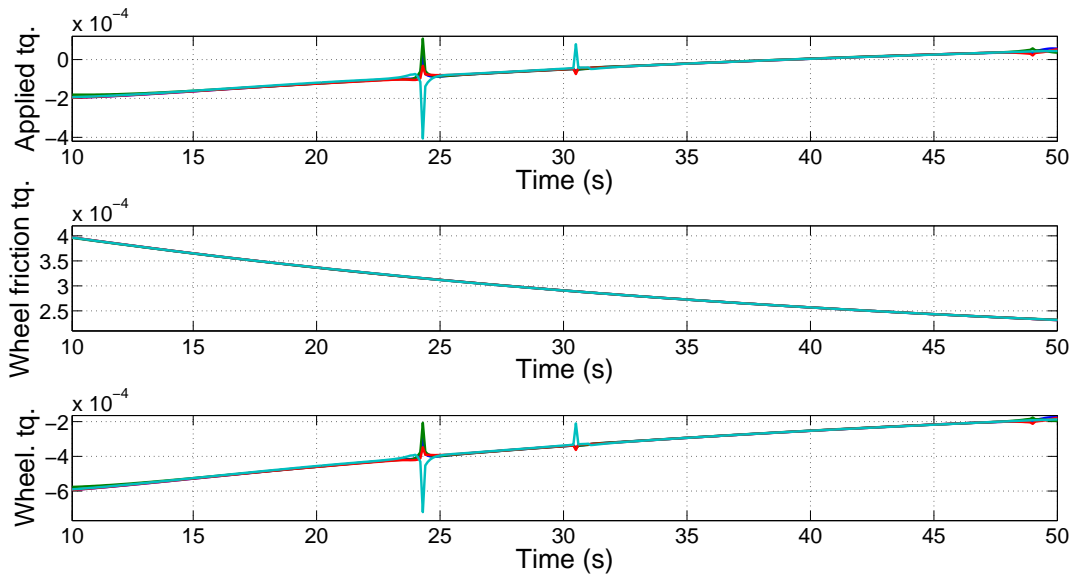


Figure 4-11. Close-up of applied wheel torque, wheel friction torque, and total wheel torque during closed-loop operation providing input power reduction.

## 4.5 Summary

In this chapter, a backstepping method is used to develop the controller from a cascade dynamics connection for a VSCMG-actuated satellite. In the presence of uncertain dynamic and static frictions in both the gimbals and the flywheels, the controller is capable of achieving global asymptotic attitude tracking while simultaneously performing singularity avoidance and wheel deceleration. Simulations show that the applied torques of the wheels containing friction contribute to power reduction in that the friction enables the wheel to obtain more torques without an additional torque request. Such benefit is induced by the deceleration mode resulting from the null motion and can give the actuator both torque and power reduction effect. Also, the applied control torque can responsively realize more realistic torque considering friction loss in practical use and such consideration can allow the system to maintain consistent performance in the presence of dynamic uncertainty.

CHAPTER 5  
A NEW INITIAL START-UP METHOD USING INTERNAL MOMENTUM  
MANAGEMENT OF VSCMGs

An adaptive controller is developed in this chapter that use internal momentum management and singularity avoidance while simultaneously yielding attitude control. The null solution of the closed-loop flywheel control input achieves internal momentum management so that the flywheel starts from rest and reaches the desired wheel speed without a separate feedback control loop. The closed-loop VSCMGs steering law yields simultaneous asymptotic attitude tracking, exponential internal momentum tracking, and singularity avoidance. The singularity avoidance method reduces/eliminates the amount of time that the VSCMG has to operate in RW mode when the CMG Jacobian becomes singular through the use of null motion. The controller is developed for a satellite with an uncertain, state-dependent inertia along with an uncertain inertia in the VSCMG actuators. Numerical simulations illustrate the performance of the developed adaptive controller as a VSCMGs steering law.

## 5.1 Control Objectives

### 5.1.1 Attitude Control Objective

The attitude control objective is to develop a flywheel acceleration and gimbal rate control law to enable the attitude of  $\mathcal{F}_S$  to track the attitude of  $\mathcal{F}_{S_d}$ . The objective is quantified in 3.2.1 in Chapter 3.

### 5.1.2 Flywheel Angular Momentum Management Objective

The angular momentum  $h(\Omega) \in \mathbb{R}^4$  generated by the flywheels of the four VSCMGs can be expressed as

$$h = [I_W]^d \Omega. \tag{5-1}$$

The flywheel angular momentum management objective is to develop an internal momentum tracking control law resulting from the null solution of the flywheel control input so that the actual angular momentum tracks a desired constant angular momentum  $h_d \in \mathbb{R}^4$ , while simultaneously tracking a desired time-varying attitude. To quantify the momentum

management objective, an angular momentum tracking error  $\mu(\Omega) \in \mathbb{R}^4$  is defined as

$$\mu \triangleq h_d - h, \quad (5-2)$$

where the desired angular momentum is defined as  $h_d \triangleq [I_W]^d \Omega_d$ .

## 5.2 Controller Development

### 5.2.1 Adaptive Attitude Control Development

To facilitate the control design, an auxiliary signal  $r(\omega, e_0, e_v) \in \mathbb{R}^3$  is defined as [23]

$$r \triangleq \omega - \tilde{R}\omega_d + \alpha e_v, \quad (5-3)$$

where  $\alpha \in \mathbb{R}^{3 \times 3}$  is a constant, positive definite, diagonal control gain matrix. After substituting (5-3) into (3-7), the angular velocity tracking error can be expressed as

$$\tilde{\omega} = r - \alpha e_v. \quad (5-4)$$

Taking the time derivative of (5-3) and multiplying both sides of the resulting expression by  $J(\delta)$  yields

$$J\dot{r} = J\dot{\omega} + J\omega^\times \tilde{R}\omega_d - J\tilde{R}\dot{\omega}_d + \frac{1}{2}J\alpha(e_v^\times + e_0 I_3)\tilde{\omega}, \quad (5-5)$$

where the fact that

$$\dot{\tilde{R}} = -\omega^\times \tilde{R}$$

was utilized. After substituting (2-14) into (5-5), the open-loop error dynamics for  $r(\omega, e_0, e_v)$  can be written as

$$J\dot{r} = -Q\dot{\eta} + Y_1\theta_1 - \frac{1}{2}Jr + C_G [I_W]^d [\omega_T]^d \Omega - C_T [I_W]^d [\omega_G]^d \Omega, \quad (5-6)$$

under the standard assumption that the gimbal acceleration term  $C_G [I_G^{CMG}]^d \ddot{\delta}(t)$  is negligible [26, 83, 89]. In (5–6),  $Q(e_0, e_v, r, \omega, \delta, \Omega) \in \mathbb{R}^{3 \times 8}$  is defined as

$$Q \triangleq \begin{bmatrix} C_W [I_W]^d & C_W [I_G^{CMG}]^d [\omega_T]^d + C_T \left( [I_W]^d [\Omega]^d \right. \\ \left. - [I_G^{CMG}]^d [\omega_W]^d \right) + \frac{\partial J}{\partial \delta} \left( \frac{1}{2} r + \tilde{R} \omega_d - \alpha e_v \right) \end{bmatrix},$$

$\dot{\eta} = \begin{bmatrix} \dot{\Omega}^T & \dot{\delta}^T \end{bmatrix}^T \in \mathbb{R}^{8 \times 1}$  is a composite control input consisting of the flywheel accelerations and the gimbal rates, and  $Y_1(e_0, e_v, r, \omega, \delta) \theta_1$  represents linearly parametrizable uncertainty in terms of a measurable regression matrix  $Y_1(e_0, e_v, r, \omega, \delta) \in \mathbb{R}^{3 \times p_1}$  and a vector of  $p_1$  unknown constants  $\theta_1 \in \mathbb{R}^{p_1}$  defined as

$$Y_1 \theta_1 \triangleq -\omega \times J \omega + J \omega^\times \tilde{R} \omega_d - J \tilde{R} \dot{\omega}_d + \frac{1}{2} J \alpha (e_v^\times + e_0 I_3) \tilde{\omega}. \quad (5-7)$$

To compensate for the linearly parametrizable uncertainty present in  $Q(e_0, e_v, r, \omega, \delta, \Omega)$ , another regression matrix denoted by  $Y_2(e_0, e_v, r, \omega, \delta, \Omega, \dot{\delta}, \dot{\Omega}) \in \mathbb{R}^{3 \times p_2}$  and a vector of  $p_2$  unknown constants  $\theta_2 \in \mathbb{R}^{p_2}$  are defined as

$$Y_2 \theta_2 \triangleq -Q \dot{\eta}. \quad (5-8)$$

To address the fact that the control input  $\dot{\eta}(t)$  is premultiplied by the nonsquare, state-dependent uncertain matrix  $Q(e_0, e_v, r, \omega, \delta, \Omega)$ , an estimate of the uncertainty in (5–8),  $\hat{Q}(t) \in \mathbb{R}^{3 \times 8}$  is defined as

$$Y_2 \hat{\theta}_2 \triangleq -\hat{Q} \dot{\eta}, \quad (5-9)$$

where  $\hat{\theta}_2(t) \in \mathbb{R}^{p_2}$  is a subsequently designed estimate for the parametric uncertainty in  $Q(e_0, e_v, r, \omega, \delta, \Omega)$ . Based on (5–8) and (5–9), the expression in (5–6) can be written as

$$J \dot{r} = Y_2 \tilde{\theta}_2 - \hat{Q} \dot{\eta} + Y_1 \theta_1 - \frac{1}{2} J r + C_G [I_W]^d [\omega_T]^d \Omega - C_T [I_W]^d [\omega_G]^d \Omega, \quad (5-10)$$

where the notation  $\tilde{\theta}_2(t) \in \mathbb{R}^{p_2}$  is defined as

$$\tilde{\theta}_2 \triangleq \theta_2 - \hat{\theta}_2. \quad (5-11)$$

Based on the open-loop error dynamics of (5–10), the composite weighted VSCMG steering law is designed as

$$\dot{\eta} = \hat{Q}_w^+ \left( Y_1 \hat{\theta}_1 + kr + e_v + C_G [I_W]^d [\omega_T]^d \Omega - C_T [I_W]^d [\omega_G]^d \Omega \right) + \left( I_8 - \hat{Q}_w^+ \hat{Q} \right) S \sigma, \quad (5-12)$$

where  $k \in \mathbb{R}$  denotes a positive control gain,  $\hat{Q}_w^+(\delta, t) = W(\delta) \hat{Q}^T(t) \left( \hat{Q}(t) W(\delta) \hat{Q}^T(t) \right)^{-1}$ , and  $W(\delta) \in \mathbb{R}^{8 \times 8}$  denotes a weight matrix that determines if the VSCMGs system uses a CMG mode or a RW mode. Specifically,  $W(\delta)$  is designed as [87, 89, 101]

$$W \triangleq \begin{bmatrix} W_\Omega I_{4 \times 4} & 0_{4 \times 4} \\ 0_{4 \times 4} & W_\delta I_{4 \times 4} \end{bmatrix}, \quad (5-13)$$

where  $W_\Omega(\delta) \in \mathbb{R}$  is defined as

$$W_\Omega \triangleq W_{\Omega 0} \exp(\lambda_1 f),$$

$\lambda_1, W_{\Omega 0}, W_\delta \in \mathbb{R}$  are positive constants, and the objective function  $f(\delta)$  measuring the singularity is defined as

$$f \triangleq -\det(C_T C_T^T). \quad (5-14)$$

The control input in (5–12) has an extra degree of freedom resulting from the variable speed flywheel, and thus enables the VSCMG system to escape a gimbal lock singularity [89]. Since the control input in (5–12) is produced by VSCMG units, (5–12) is also a solution to an underdetermined system containing flywheel accelerations and gimbal rates as unknowns [55, 89, 100]. The term  $\left( I_8 - \hat{Q}_w^+(\delta, t) \hat{Q}(t) \right) S(\delta) \sigma(t)$  in (5–12) generates the VSCMG null motion for internal momentum management and singularity avoidance. Since the matrices  $\hat{Q}_w^+(\delta, t)$  and  $\hat{Q}(t)$  are nonsquare, the pseudo-inverse  $\hat{Q}_w^+(\delta, t) \in \mathbb{R}^{8 \times 3}$  is defined so that  $\hat{Q}(t) \hat{Q}_w^+(\delta, t) = I_3$ , and the matrix  $I_8 - \hat{Q}_w^+(\delta, t) \hat{Q}(t)$ , which projects

vectors onto the null space of  $\hat{Q}(t)$ , satisfies the properties

$$\left(I_8 - \hat{Q}_w^+ \hat{Q}\right) \left(I_8 - \hat{Q}_w^+ \hat{Q}\right) = I_8 - \hat{Q}_w^+ \hat{Q} \quad (5-15)$$

$$\hat{Q} \left(I_8 - \hat{Q}_w^+ \hat{Q}\right) = 0. \quad (5-16)$$

To generate null motion for momentum tracking and gimbal reconfiguration, the null motion  $\sigma(t) \in \mathbb{R}^8$  is defined as

$$\sigma \triangleq \begin{bmatrix} k_w g^T & k_\gamma \frac{\partial \gamma}{\partial \delta}^T \end{bmatrix}^T, \quad (5-17)$$

where  $k_w, k_\gamma \in \mathbb{R}$  denote positive constants,  $g(t) \in \mathbb{R}^4$  is a subsequently designed auxiliary control signal to track the desired flywheel angular momentum, and the second row allows the null motion to perform the gimbal reconfiguration corresponding to a variation of the singularity measure index  $\gamma$ , which is defined as [97]

$$\gamma = \gamma_0 \exp(\lambda_2 f), \quad (5-18)$$

where the objective function  $f$  is defined in (5-14), and  $\lambda_2, \gamma_0 \in \mathbb{R}$  denote positive constants. The matrix  $S(\delta) \in \mathbb{R}^{8 \times 8}$  in (5-12) is used as a null motion weight for the VSCMG null motion, which can weigh a proper null motion based on the singularity measure. Specifically,  $S(\delta)$  is designed as

$$S \triangleq \text{diag}([s_w, s_g]) = \begin{bmatrix} \text{sech} \left( \frac{1}{k_d \det(C_T C_T^T) + \varepsilon} \right) I_{4 \times 4} & 0_{4 \times 4} \\ 0_{4 \times 4} & \text{sech}(k_g \det(C_T C_T^T)) I_{4 \times 4} \end{bmatrix}, \quad (5-19)$$

where  $k_d, k_g, \varepsilon \in \mathbb{R}$ . In (5-19),  $s_w(\delta)$  and  $s_g(\delta)$  selectively arbitrate between internal momentum tracking and gimbal reconfiguration, corresponding to how approximate or far the CMG configuration is to a singularity. Gimbal reconfiguration results from null motion when the CMG Jacobian becomes singular (i.e., a hyperbolic singularity), allowing simultaneous attitude and internal momentum tracking with the benefits of torque amplification in CMG mode. When the CMG experiences a degenerate singularity (i.e.,

even though the null motions exist, the singularity cannot be escaped by the null motions) or when a gimbal lock singularity (i.e., an elliptic singularity) occurs, then  $s_w(\delta) \approx 0$  which inhibits momentum tracking so that the VSCMG will operate in RW mode.

The control input  $\dot{\eta}(t)$  in (5-12) can be partitioned as

$$\dot{\eta} = \begin{bmatrix} \dot{\Omega} \\ \dot{\delta} \end{bmatrix} = \begin{bmatrix} R_1 + N_1 \bar{s}_w k_w g \\ R_2 + N_2 \bar{s}_g k_\gamma \frac{\partial \gamma}{\partial \delta} \end{bmatrix}, \quad (5-20)$$

where  $R_i = \left[ \hat{Q}_w^+ \left( Y_1 \hat{\theta}_1 + kr + e_v + C_G [I_W]^d [\omega_T]^d \Omega - C_T [I_W]^d [\omega_G]^d \Omega \right) \right]_i$  indicates components of each  $\mathbb{R}^4$  control input,  $N_1(t), N_2(t) \in \mathbb{R}^{4 \times 8}$  are defined as

$$N \triangleq \begin{bmatrix} N_1 \\ N_2 \end{bmatrix} = \begin{bmatrix} \left( I_8 - \hat{Q}_w^+ \hat{Q} \right) \\ \left( I_8 - \hat{Q}_w^+ \hat{Q} \right) \end{bmatrix} \quad (5-21)$$

and  $\bar{s}_w(\delta), \bar{s}_g(\delta) \in \mathbb{R}^{8 \times 4}$  are defined as

$$\bar{s}_w \triangleq \begin{bmatrix} s_w & 0_{4 \times 4} \end{bmatrix}^T \quad \bar{s}_g \triangleq \begin{bmatrix} 0_{4 \times 4} & s_g \end{bmatrix}^T.$$

After substituting (5-12) into (5-10) and using (5-16), closed-loop dynamics for  $r(\omega, e_0, e_v)$  are given by

$$J\dot{r} = -\frac{1}{2}Jr + Y_1 \tilde{\theta}_1 + Y_2 \tilde{\theta}_2 - kr - e_v, \quad (5-22)$$

where the notation  $\tilde{\theta}_1(t) \in \mathbb{R}^{p_1}$  is defined as

$$\tilde{\theta}_1 = \theta_1 - \hat{\theta}_1. \quad (5-23)$$

Based on (5-22) and the subsequent stability analysis, the parameter estimates  $\hat{\theta}_1(t)$  and  $\hat{\theta}_2(t)$  are designed as

$$\dot{\hat{\theta}}_1 = \text{proj}(\Gamma_1 Y_1^T r) \quad \dot{\hat{\theta}}_2 = \text{proj}(\Gamma_2 Y_2^T r), \quad (5-24)$$

where  $\Gamma_1 \in \mathbb{R}^{p_1 \times p_1}$  and  $\Gamma_2 \in \mathbb{R}^{p_2 \times p_2}$  are constant, positive-definite, diagonal adaptation gain matrices, and  $proj(\cdot)$  denotes a projection algorithm utilized to guarantee that the  $i^{th}$  element of  $\hat{\theta}_1(t)$  and  $\hat{\theta}_2(t)$  can be bounded as

$$\underline{\theta}_{1i} \leq \hat{\theta}_{1i} \leq \bar{\theta}_{1i} \quad \underline{\theta}_{2i} \leq \hat{\theta}_{2i} \leq \bar{\theta}_{2i}, \quad (5-25)$$

where  $\underline{\theta}_{1i}, \bar{\theta}_{1i} \in \mathbb{R}$  and  $\underline{\theta}_{2i}, \bar{\theta}_{2i} \in \mathbb{R}$  are known, constant lower and upper bounds for each element of  $\hat{\theta}_1(t)$  and  $\hat{\theta}_2(t)$ , respectively.

### 5.2.2 Momentum Tracking Control Development

The open-loop dynamics for the momentum tracking error can be obtained by taking the time derivative of (5-2) as

$$\dot{\mu} = -I_W \dot{\Omega}. \quad (5-26)$$

Multiplying (5-26) by the known positive-definite symmetric matrix  $I_W^{-1}$ , and substituting (5-20) into the resulting expansion for  $\dot{\Omega}(t)$  yields

$$I_W^{-1} \dot{\mu} = -R_1 - N_1 \bar{s}_w k_w g. \quad (5-27)$$

Based on the structure of (5-27), the null-space control  $g(t)$  is designed to satisfy

$$k_w N_1 \bar{s}_w g = -R_1 + k_m \mu, \quad (5-28)$$

where  $k_m \in \mathbb{R}$  is a positive constant control gain. The minimum norm solution of (5-28) is

$$g = [k_w N_1 \bar{s}_w]^{-1} (-R_1 + k_m \mu). \quad (5-29)$$

The result in (5-29) indicates that simultaneous attitude and momentum tracking is possible when  $k_w N_1(\delta, t) \bar{s}_w(\delta)$  is invertible. After substituting (5-29) into (5-27), the closed-loop error system is

$$I_W^{-1} \dot{\mu} = -k_m \mu. \quad (5-30)$$

**Remark 5.1.** The bracketed term in (5-29) is invertible, and simultaneous attitude and momentum tracking is possible when  $N_1(\delta, t) \bar{s}_w(\delta) = \left( I_8 - \hat{Q}_w^+(\delta, t) \hat{Q}(t) \right)_{4 \times 8} \bar{s}_w(\delta) \neq 0$ . Since  $\left( I_8 - \hat{Q}_w^+(\delta, t) \hat{Q}(t) \right)$  is nonzero for all  $\hat{Q}(t)$ ,  $N_1(\delta, t) \neq 0$  and simultaneous attitude and momentum tracking can be achieved provided

$$\bar{s}_w \neq 0 \text{ and } \bar{s}_w \notin \mathcal{N}(N_1),$$

where  $\mathcal{N}(N_1(\delta, t))$  denotes the null space of the matrix  $N_1(\delta, t)$ . Hence,  $\bar{s}_w(\delta) \notin \mathcal{N}(N_1)$  except for  $\bar{s}_w(\delta) = 0$ , which means the CMG's Jacobian itself is singular, but  $\bar{s}_w(\delta) = 0$  does not occur for the CMGs Jacobian unless it starts out that way initially. Accordingly, as long as the system does not start in a singular configuration, the minimum norm solution of (5-28) exists and simultaneous attitude and momentum tracking can be achieved.

### 5.2.3 Stability Analysis

**Theorem 5-1:** The weighted control input (5-12) along with the adaptive update laws given in (5-24) ensures global asymptotic attitude tracking such that

$$\|e_v(t)\| \rightarrow 0 \quad \text{as} \quad t \rightarrow \infty, \quad (5-31)$$

along with exponential momentum tracking in the sense that

$$\|\mu(t)\| \leq \mu(0) \exp(-I_W k_m t). \quad (5-32)$$

*Proof:* The exponential internal momentum tracking result is evident from (5-30).

To prove the attitude tracking result, let  $\mathcal{D} \subset \mathbb{R}^8$  be a domain containing  $\rho(e_v, e_0, r, P) = 0$ , where  $\rho(e_v, e_0, r, P) \in \mathbb{R}^8$  is defined as

$$\rho(t) \triangleq \begin{bmatrix} e_v^T(t) & e_0(t) & r^T(e_v, e_0, \omega) & P(\tilde{\theta}_1(t), \tilde{\theta}_2(t)) \end{bmatrix}^T$$

and the auxiliary function  $P(\tilde{\theta}_1(t), \tilde{\theta}_2(t)) \in \mathbb{R}$  is defined as

$$P \triangleq \frac{1}{2} \tilde{\theta}_1^T \Gamma_1^{-1} \tilde{\theta}_1 + \frac{1}{2} \tilde{\theta}_2^T \Gamma_2^{-1} \tilde{\theta}_2, \quad (5-33)$$

and let  $V(\rho, \delta) : \mathcal{D} \times [0, \infty) \rightarrow \mathbb{R}$  be a continuously differentiable, positive definite function defined as

$$V \triangleq e_v^T e_v + (1 - e_0)^2 + \frac{1}{2} r^T J r + P. \quad (5-34)$$

After using (3-17), (5-11), (5-22), (5-23), and (5-33), the time derivative of  $V(\rho, \delta)$  can be expressed as

$$\begin{aligned} \dot{V} &= e_v^T (e_v^\times + e_0 I) \tilde{\omega} + (1 - e_0) e_v^T \tilde{\omega} + r^T (Y_1 \tilde{\theta}_1 + Y_2 \tilde{\theta}_2 - k r - e_v) \\ &\quad - \tilde{\theta}_1^T \Gamma_1^{-1} \dot{\hat{\theta}}_1 - \tilde{\theta}_2^T \Gamma_2^{-1} \dot{\hat{\theta}}_2. \end{aligned} \quad (5-35)$$

By using (5-4), (5-24), and exploiting the fact that  $e_v^T(t) e_v^\times(t) \tilde{\omega}(t) = 0$ , the expression in (5-35) can be upper bounded as

$$\dot{V} \leq -\lambda \|z\|^2, \quad (5-36)$$

where  $\lambda = \lambda_{\min}\{\alpha, k\} \in \mathbb{R}$ , and  $z(e_v, r) \in \mathbb{R}^6$  is defined as

$$z \triangleq \begin{bmatrix} e_v^T(t) & r^T(e_v, e_0, \omega) \end{bmatrix}^T. \quad (5-37)$$

From (5-34) and (5-36),  $r(e_v, e_0, \omega), e_v(t), \tilde{\theta}_1(t), \tilde{\theta}_2(t) \in \mathcal{L}_\infty$ . Thus, from (6-8), (5-4), and (5-37),  $e_v(t), e_0(t), \tilde{\omega}(t), z(e_v, r) \in \mathcal{L}_\infty$ , and (5-3) can be used to conclude that  $\omega(t) \in \mathcal{L}_\infty$ . The open-loop quaternion tracking error in (3-17) can be used to conclude that  $\dot{e}_v(t), \dot{e}_0(t) \in \mathcal{L}_\infty$ . From (5-32),  $\mu(t) \in \mathcal{L}_\infty$  and then (5-1) and (5-2) can be used to indicate that the fact that  $\Omega(t) \in \mathcal{L}_\infty$ . In (2-8), conservation of angular momentum,  $\omega(t)$ , and  $\Omega(t) \in \mathcal{L}_\infty$  shows that  $\dot{\delta}(t) \in \mathcal{L}_\infty$ . The fact that  $\delta(t)$ -dependent function result from direction cosine matrices indicates that the functions contain  $\delta(t)$  within bounded trigonometric functions. Since  $e_v(t), e_0(t), r(e_v, e_0, \omega), \omega(t), \Omega(t) \in \mathcal{L}_\infty$ , (5-7) and (5-25) can be used to show that  $g(t) \in \mathcal{L}_\infty$ . The fact that  $r(e_v, e_0, \omega), e_v(t), \dot{\delta}(t), \tilde{\theta}_1(t), \tilde{\theta}_2(t) \in$

$\mathcal{L}_\infty$  can be used with (5-22) to conclude that  $\dot{r}(e_v, e_0, r, \dot{\delta}, \tilde{\theta}_1, \tilde{\theta}_2) \in \mathcal{L}_\infty$ . From (5-11) and (5-23),  $\hat{\theta}_1(t), \hat{\theta}_2(t) \in \mathcal{L}_\infty$ . Hence, (5-12), (5-17), (5-25), (5-29), and  $z(e_v, r), \Omega(t) \in \mathcal{L}_\infty$  can be used to prove that the control input  $\dot{\eta}(t) \in \mathcal{L}_\infty$ . Standard signal chasing arguments can then be utilized to prove that all remaining signals are bounded during closed-loop operation. Since  $e_v(t), r(e_v, e_0, \omega), \dot{e}_v(t), \dot{r}(e_v, e_0, r, \dot{\delta}, \tilde{\theta}_1, \tilde{\theta}_2) \in \mathcal{L}_\infty$ ,  $e_v(t)$  and  $r(e_v, e_0, \omega)$  are uniformly continuous. Since  $e_v(t)$  and  $r(e_v, e_0, \omega)$  are uniformly continuous, and  $e_v(t), r(e_v, e_0, \omega) \in \mathcal{L}_\infty \cap \mathcal{L}_2$ , Barbalat's Lemma can be used to prove  $r(e_v, e_0, \omega), e_v(t) \rightarrow 0$  as  $t \rightarrow \infty$ . ■

### 5.3 Numerical Examples

#### 5.3.1 Simulation Setup

Numeric simulations illustrate the performance of the developed controller. The satellite parameters are based on a model of a prototype pico-satellite and are given in Table 5-1. A gimbal rate limit was included in the model as

$$\text{sat}(\dot{\delta}_i) = \begin{cases} \dot{\delta}_i, & \text{for } |\dot{\delta}_i| \leq 25 \text{ (rad/sec)} \\ 25 \text{sgn}(\dot{\delta}_i), & \text{for } |\dot{\delta}_i| > 25 \text{ (rad/sec)} \end{cases}, \quad \forall i = 1, 2, 3, 4, \quad (5-38)$$

where  $\text{sgn}(\cdot)$  denotes the standard signum function. The desired angular velocity trajectories  $\omega_d(t)$  are  $\omega_d(t) = \begin{bmatrix} 0.004 \sin(2\pi t/2000) & 0 & 0 \end{bmatrix}$  (rad/sec), and the desired flywheel speed for each wheel is  $\Omega_d = 200 \text{ rad/s} (\approx 2,000 \text{ rpm})$ . The initial conditions are given in Table 5-2.

Physical Parameter	Value
$J(0) \text{ (kg} \cdot \text{m}^2)$	$\text{diag} \{ 6.10 \times 10^{-2} \quad 6.10 \times 10^{-2} \quad 7.64 \times 10^{-2} \}$
$m_{cmg} \text{ (kg)}$	0.165
$I_G \text{ (kg} \cdot \text{m}^2)$	$2.80 \times 10^{-3} I_4$
$I_W \text{ (kg} \cdot \text{m}^2)$	$6.95 \times 10^{-4} I_4$
$\text{skewangle} \text{ (}^\circ)$	54.74

Table 5-1. Physical parameters for the VSCMG simulation.

Initial Parameter	Value
$q(0)$	[ 0.1 0.3 0.8 0.4 ]
$\omega(0)$ (rad/s)	0
$\hat{\theta}_1(0), \hat{\theta}_2(0)$	0
$\delta(0)$ (rad)	[ 0.5498 0.2333 0.5498 0.2333 ]
$\Omega(0)$ (rad/s)	0

Table 5-2. Initial parameters for the VSCMG simulation.

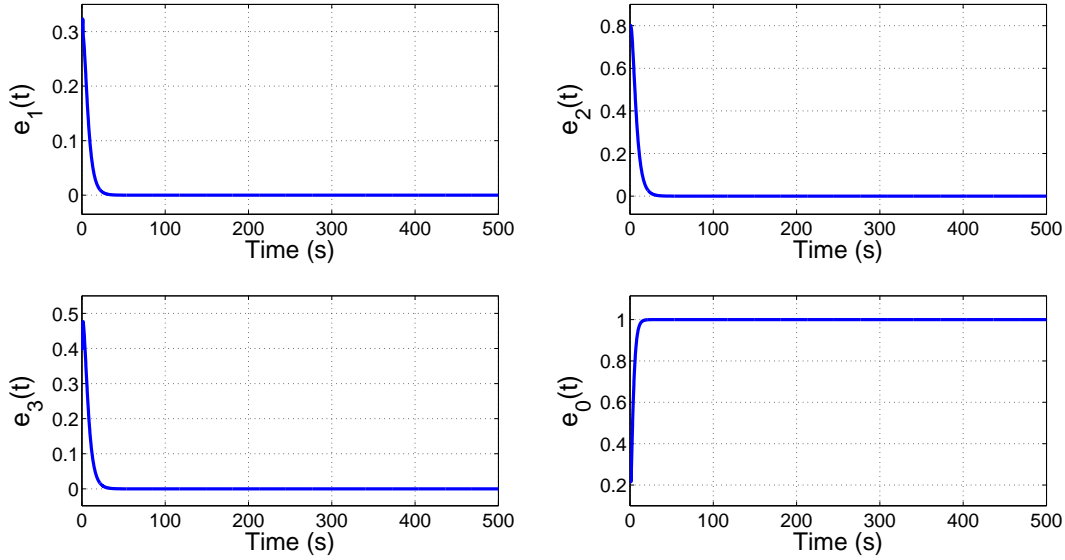


Figure 5-1. Quaternion tracking error  $e(t)$  for Case 1.

### 5.3.2 Simulation Results

The simulation results are developed for two cases. Case 1 is included to illustrate how the controller responds when the momentum tracking has a long transient. For this case the VSCMG has to operate in RW mode during the transient, resulting in gimbal rate saturation. The results are given in Figures 5-1 - 5-8. Case 2 is included to illustrate a more favorable condition (which can be achieved through control gains) where the momentum tracking error has a short transient response. Results in Figures 5-9 - 5-12 illustrate that for this case, gimbal rate saturation is avoided and the VSCMG operates in RW mode less than for Case 1. Figure 5-1 shows the quaternion tracking error results to achieve the control objective denoted in (3-6) during a 500s simulation

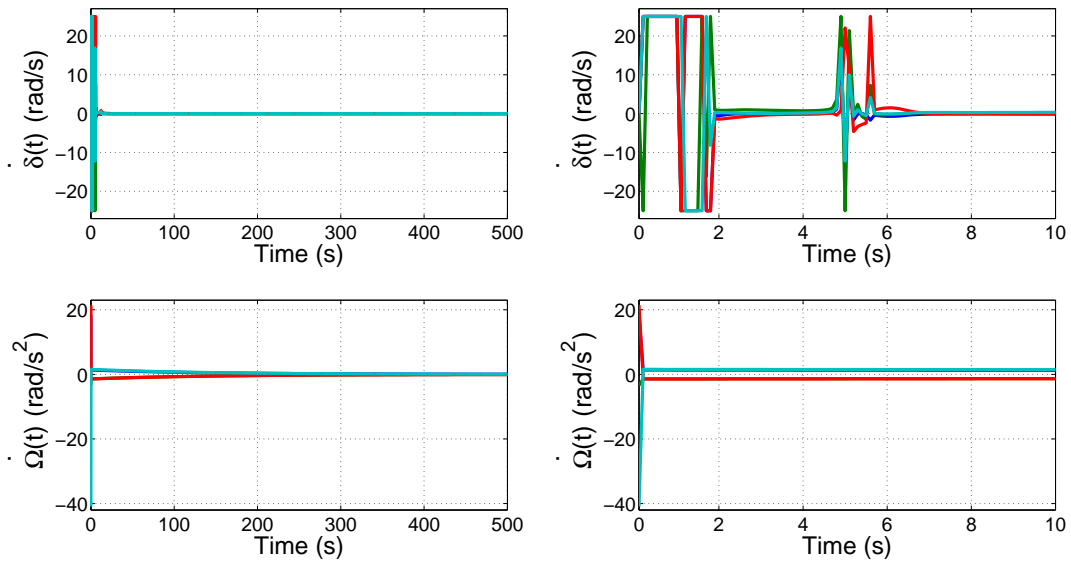


Figure 5-2. Control input gimbal rates  $\dot{\delta}(t)$  and wheel accelerations  $\dot{\Omega}(t)$  for Case 1. The left column illustrates the response for the entire duration, and the right column illustrates the transient response, including gimbal rate saturation.

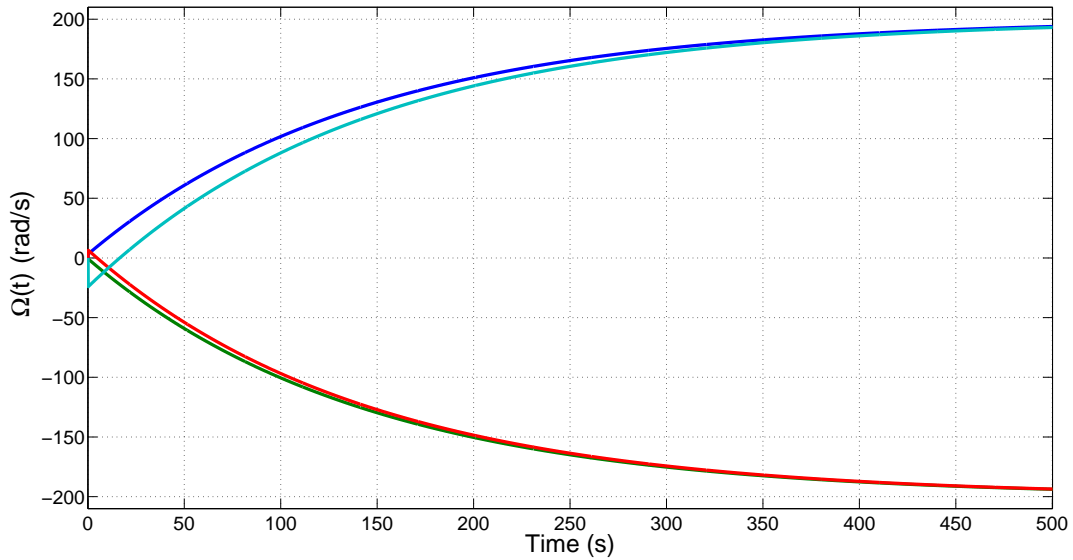


Figure 5-3. Flywheel speed  $\Omega(t)$  induced from internal momentum management for Case 1.

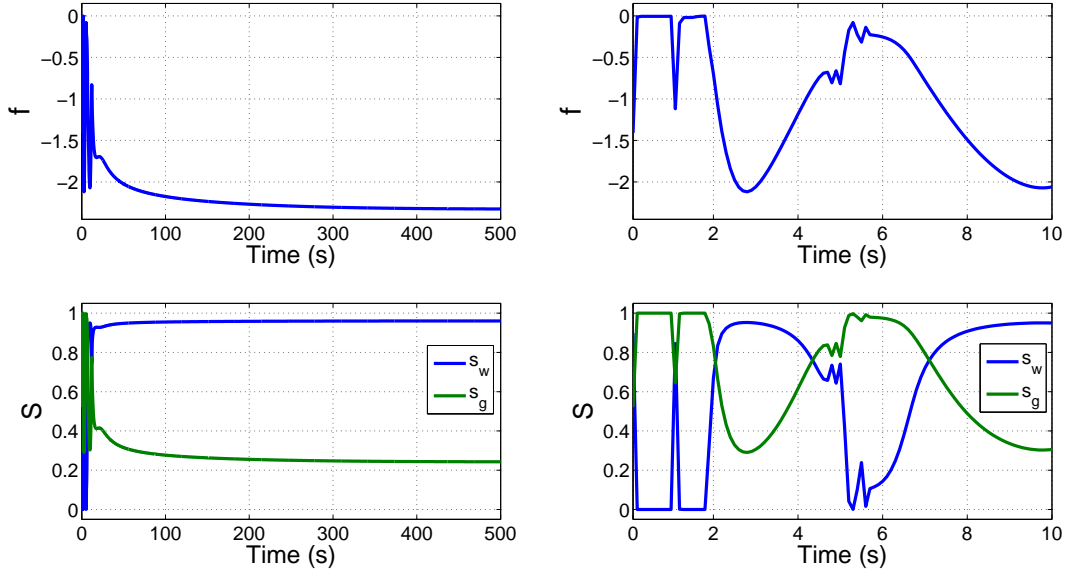


Figure 5-4. Singularity measure function  $f(\delta)$  and null motion weight  $S(\delta)$  for Case 1. The left column illustrates the response for the entire duration, and the right column illustrates the transient response, including gimbal rate saturation.

period. Figure 5-2 shows the control input gimbal rates  $\dot{\delta}(t)$  and wheel accelerations  $\dot{\Omega}(t)$ . While the control inputs achieve attitude stabilization, the wheel acceleration control input  $\dot{\Omega}(t)$  contributes to the internal momentum management by regulating the wheel speed after starting from rest. Figure 5-3 indicates the initial start-up of flywheels from rest. To compensate for the lack of torque generated by the flywheel due to the slow momentum tracking, the gimbal rates in Figure 5-2 are shown to generate more torques (including torque saturation) during the transient response. The increased transient response of the gimbal rate yields increased singularities in the CMG Jacobian, but these singularities are effectively avoided as shown in Figures 5-4 and 5-5. As a result of approaching singularities, the flywheels are required to operate in RW mode as shown in Figure 5-3. The null motion weight  $S$  in (5-19), depicted in Figure 5-4, has an increased transient in this case because  $S$  inhibits the momentum tracking when the CMG Jacobian approaches a singularity so that the flywheel can work in RW mode. Although  $S$  cannot distinguish between different singularities, the weight matrix can adjust the intervention

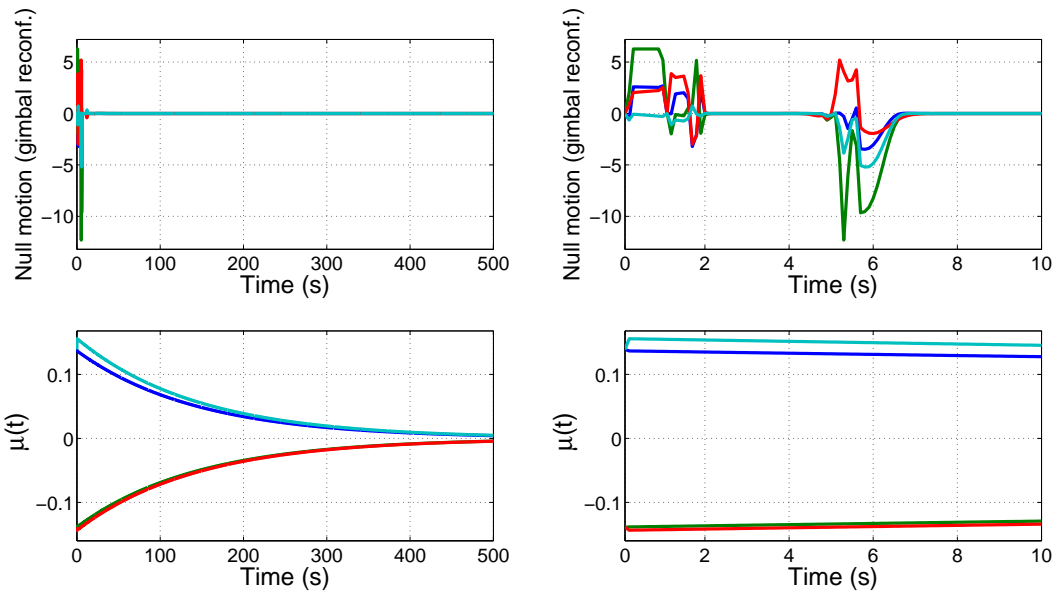


Figure 5-5. Null motion: gimbal reconfiguration and internal momentum tracking error  $\mu(t)$  for Case 1.

The left column illustrates the response for the entire duration, and the right column illustrates the transient response, including gimbal rate saturation.

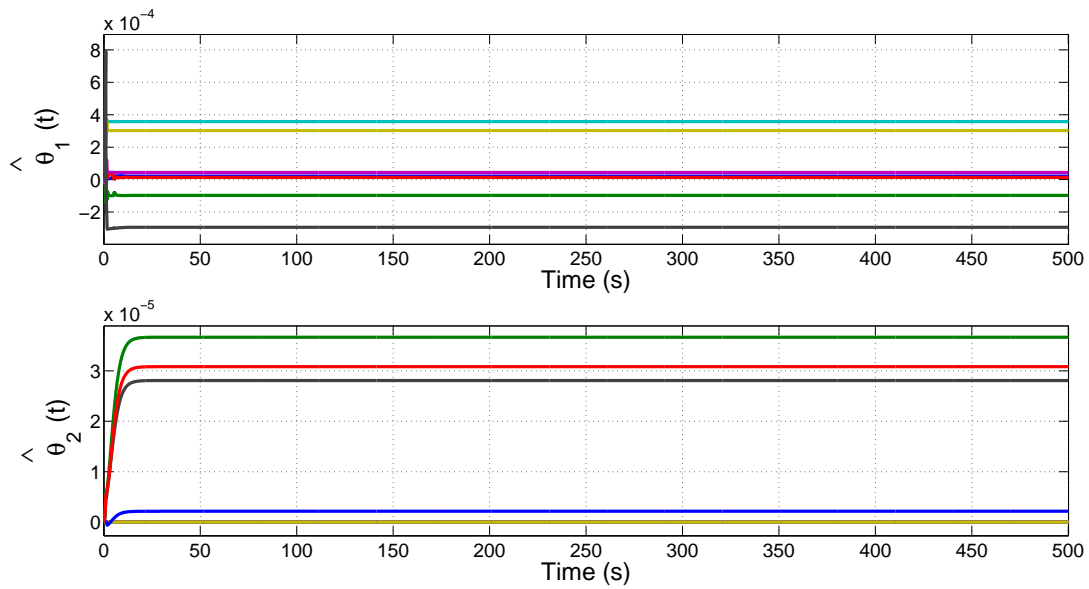


Figure 5-6. Adaptive parameter estimates  $\hat{\theta}_1(t)$  and  $\hat{\theta}_2(t)$  for Case 1.

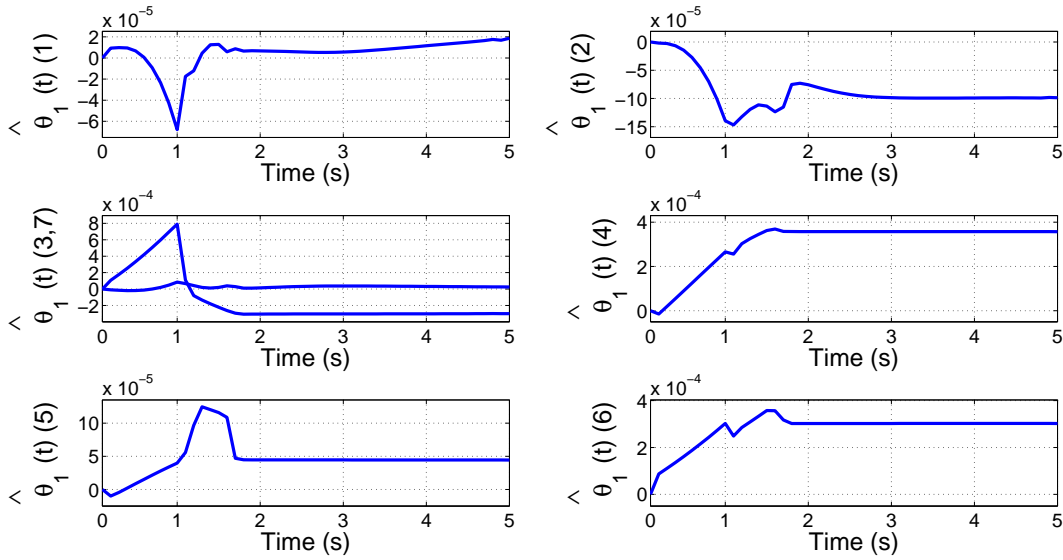


Figure 5-7. Transient response of adaptive parameter estimate  $\hat{\theta}_1(t)$  for Case 1.  
The notation  $\hat{\theta}_1(t)(x)$  denotes the  $x$ -element of  $\hat{\theta}_1(t)$ .

of the flywheel when approaching a singularity. Hence, the composite weighted steering law in (5-12) can cope with an elliptic singularity while maintaining precision attitude control since the steering law generates the required torque in RW mode to pass through or escape an internal singularity differently from the singularity escape methods for CMGs that require added torque [6, 27, 64, 77, 95, 97]. This observation indicates a benefit that results from the extra controllable degree of freedom of the VSCMG. Specifically,  $s_w$  in (5-19), depicted in Figure 5-4, allows momentum tracking when in normal operation and restricts the momentum tracking when approaching a singularity. Thus, in most regions gimbal reconfiguration is responsible for singularity avoidance by exploiting gimbal rate null solution. The null motion weight  $S$  serves as a switch that acts as an alternative to cope with both elliptic and hyperbolic singularities while achieving internal momentum management. This benefit provides an avenue to effectively acquire the initial start-up without a separate feedback loop. The time variation of the adaptive parameter estimates is shown in Figures 5-6 - 5-8. Figure 5-6 shows the elements of the adaptive parameter vectors  $\hat{\theta}_1(t)$  and  $\hat{\theta}_2(t)$ . Figures 5-7 and 5-8, divided into multiple windows for clarity,

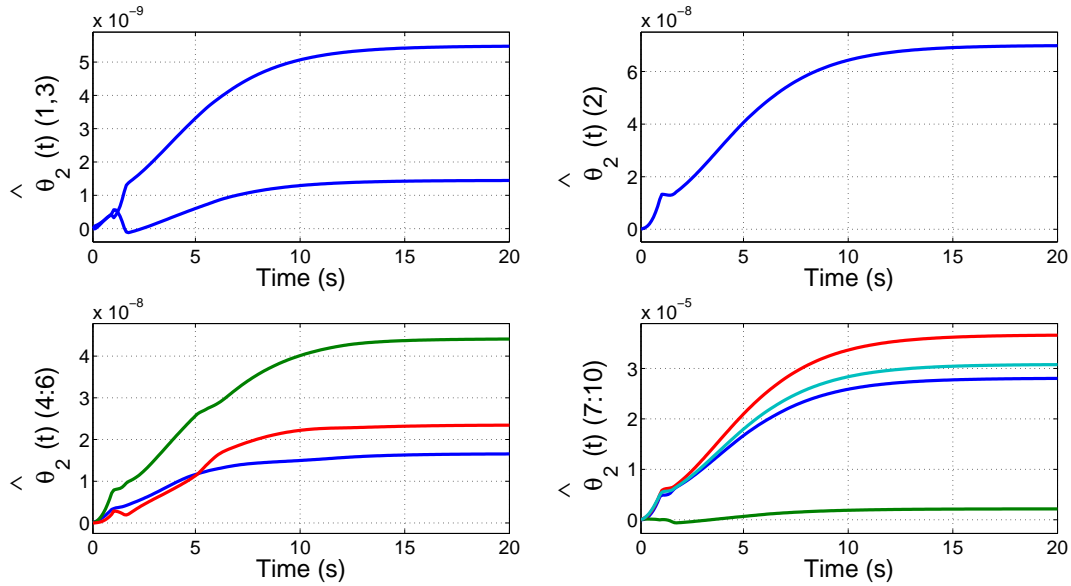


Figure 5-8. Transient response of adaptive parameter estimate  $\hat{\theta}_2(t)$  for Case 1.  
The notation  $\hat{\theta}_2(t)(x)$  denotes the  $x$ -element of  $\hat{\theta}_2(t)$ .

highlight the adaptive parameter estimates of  $\hat{\theta}_1(t)$ ,  $\hat{\theta}_2(t)$ , respectively. The adaptation mechanism adjusts the uncertain parameter estimate so that attitude tracking can be asymptotically achieved. Moreover, the initial values of the uncertain parameters are chosen to be zero, indicating no a priori parameter knowledge. Even though some of the parameter estimates indicate the variation by small magnitudes, the equivalent control torques arising from the feedforward terms  $\hat{\theta}_1(t)$ ,  $\hat{\theta}_2(t)$ , resulting from (2-14), (5-7), (5-8), (5-12), and (5-24), have similar magnitudes to that of the feedback control terms.

Case 2 is developed for the closed-loop operations in fast momentum tracking and the simulated results are provided in Figures 5-9 - 5-12. Figure 5-9 shows the gimbal rate  $\dot{\delta}(t)$  and the wheel acceleration  $\dot{\Omega}(t)$  control inputs. Figure 5-10 shows that the flywheel speed tracks the desired wheel speed from rest. The momentum tracking gain  $k_m$  denoted in (5-28) controls the momentum tracking speed. Since the flywheels rapidly arrive at the desired constant speed, fast momentum tracking allows the VSCMG steering law to operate longer in the CMG mode which provides torque amplification and power savings.

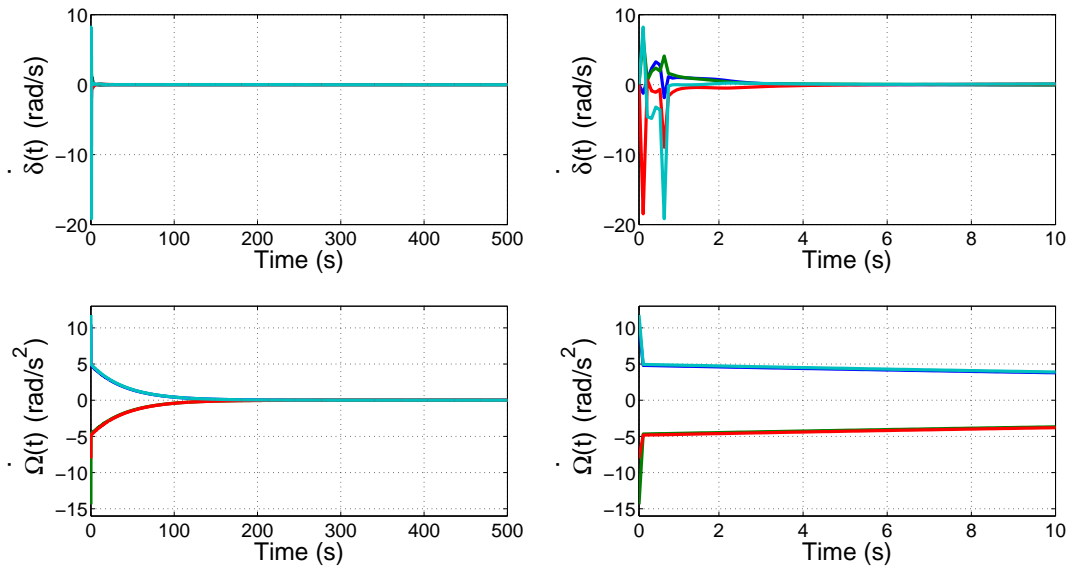


Figure 5-9. Control input gimbal rates  $\dot{\delta}(t)$  and wheel accelerations  $\dot{\Omega}(t)$  for Case 2. The left column illustrates the response for the entire duration, and the right column illustrates the transient response, including gimbal rate saturation.

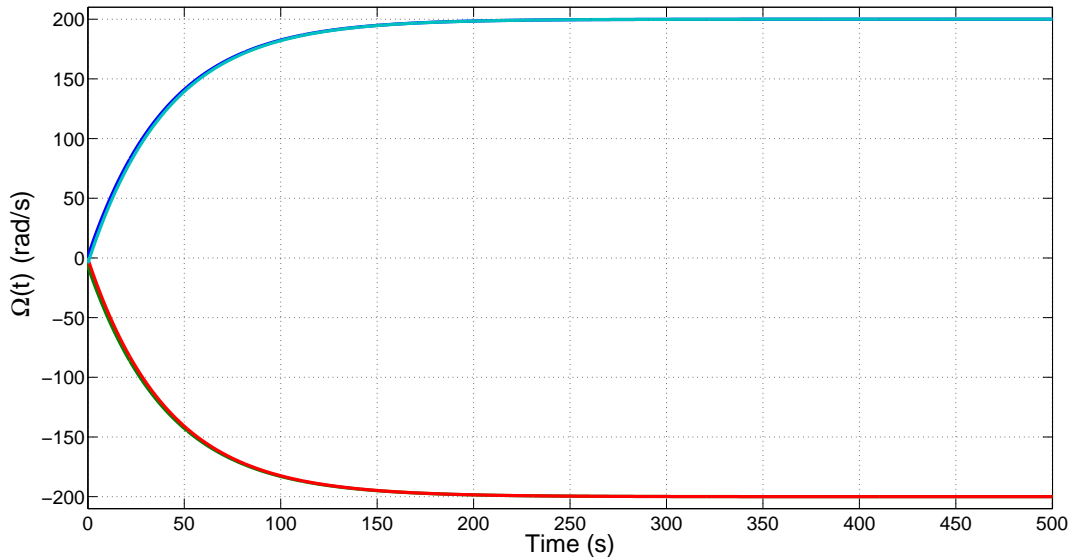


Figure 5-10. Flywheel speed  $\Omega(t)$  induced from internal momentum management for Case 2.

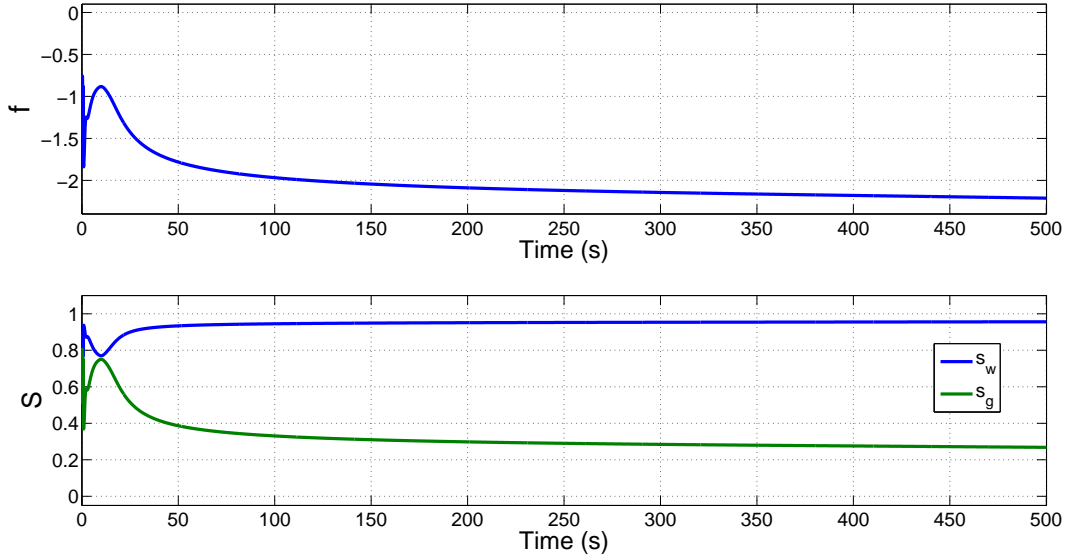


Figure 5-11. Singularity measure function  $f(\delta)$  and null motion weight  $S(\delta)$  for Case 2.

Figure 5-11 illustrates the singularity measure function  $f$  and the null motion weight  $S$ . Corresponding to the moderate variation of  $f$ ,  $s_w$  allows steady momentum tracking, and  $s_g$  generates the proper gimbals reconfiguration as depicted in Figure 5-12.

#### 5.4 Summary

In the presence of satellite inertia uncertainty and actuator uncertainty, the developed attitude controller in this chapter is capable of achieving global asymptotic attitude tracking while simultaneously performing singularity avoidance and internal momentum management. The benefits such as singularity avoidance and internal momentum management emerge from the null solution of the control inputs. In particular, the internal momentum management allows the flywheel to start from rest and to reach the desired speed. To maximize operation in CMG mode, the steering law exploits the singularity avoidance strategy resulting from the gradient method, and the null motion weight adjusts the internal momentum tracking of the flywheels when approaching an internal singularity. The VSCMG-actuated satellite can accomplish asymptotic attitude tracking and exponential internal momentum tracking while simultaneously achieving singularity avoidance.

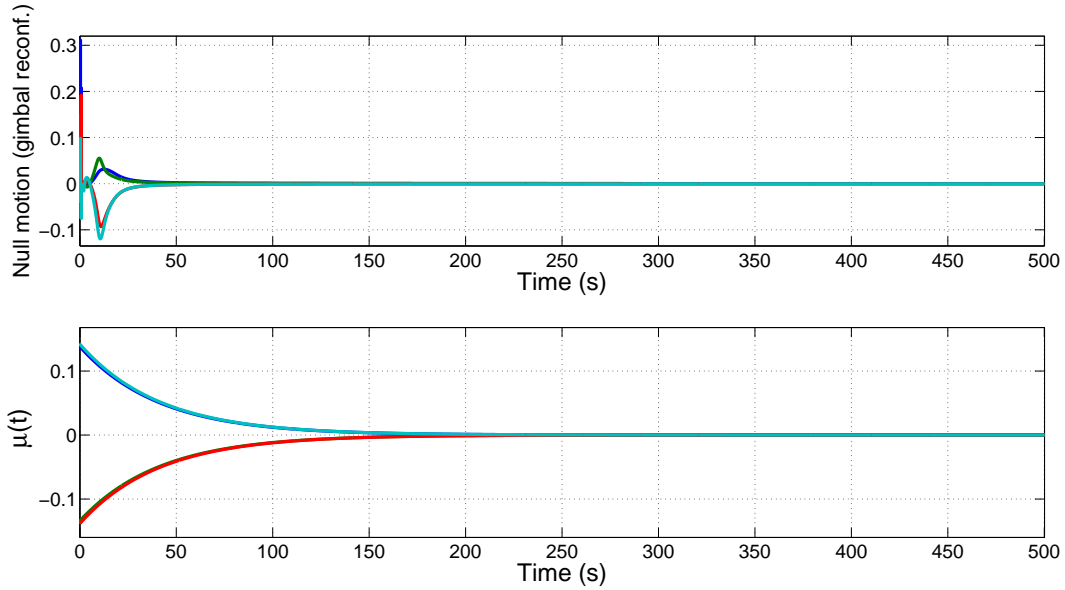


Figure 5-12. Null motion: gimbal reconfiguration and internal momentum tracking error  $\mu(t)$  for Case 2.

The controller also compensates for the effects of uncertain, time-varying satellite inertia properties. The difficulties arising from the uncertain satellite inertia are mitigated through an innovative development of the error system along with a Lyapunov-based adaptive law. The attitude tracking and momentum tracking results are proven via a Lyapunov stability analysis and demonstrated through numerical simulations.

CHAPTER 6  
A RNN-BASED ATTITUDE CONTROL METHOD FOR A VSCMG-ACTUATED  
SATELLITE

An adaptive RNN-based satellite attitude controller is developed to achieve precision attitude control of a VSCMG-actuated satellite in the presence of uncertain, time-varying satellite inertia properties and actuator uncertainties in addition to unmodeled external disturbances. The challenge encountered in the control design is that the control input is premultiplied by a non-square, time-varying, nonlinear, uncertain matrix. The RNN estimator resulting from the RNN structure serves as a composite VSCMG steering law for the satellite, which compensates for satellite and actuator uncertainties present in the nonlinear dynamics. Using null motion, a strategy is developed to simultaneously perform gimbal reconfiguration and wheel speed regularization. Numerical simulations demonstrate the performance of the adaptive RNN-based VSCMG steering law and the RNN training.

### 6.1 Dynamic Model

The equation of motion for a rigid body VSCMG-actuated satellite can be written as

$$L_r = \dot{J}\omega + J\dot{\omega} + \omega^\times J\omega + \tau_d, \quad (6-1)$$

where  $\omega(t) \in \mathbb{R}^3$  is an angular velocity of the satellite, and  $J(\delta) \in \mathbb{R}^{3 \times 3}$  is a total satellite inertia matrix containing a bus and a set of CMG units. The inertia matrix  $J(\delta)$  is positive definite and symmetric and satisfies

$$\frac{1}{2}\lambda_{\min}\{J\}\|\xi\|^2 \leq \xi^T J\xi \leq \frac{1}{2}\lambda_{\max}\{J\}\|\xi\|^2 \quad \forall \xi \in \mathbb{R}^n, \quad (6-2)$$

where  $\lambda_{\min}\{J\}$ ,  $\lambda_{\max}\{J\} \in \mathbb{R}$  are the minimum and maximum eigenvalues of  $J(\delta)$ , respectively and  $\delta(t) \in \mathbb{R}^4$  is a gimbal angular position vector. In (4-10),  $\tau_d(t) \in \mathbb{R}^3$  represents unknown, smooth disturbance torques acting on the system, which are assumed to be bounded as

$$\|\tau_d\| \leq \rho_1, \quad (6-3)$$

where  $\rho_1 \in \mathbb{R}$  is a known positive bounding constant, and the control torque  $L_r(t) \in \mathbb{R}^3$  produced by a set of four VSCMGs can be expressed as

$$\begin{aligned} L_r = & -Q_0\dot{\eta} + C_G [I_W]^d [\omega_T]^d \Omega - C_T [I_W]^d [\omega_G]^d \Omega \\ & -C_G [I_G^{CMG}]^d \ddot{\delta}. \end{aligned} \quad (6-4)$$

In (6-4),  $Q_0(\omega, \delta, \Omega) \in \mathbb{R}^{3 \times 8}$  is defined as

$$\begin{aligned} Q_0 \triangleq & \begin{bmatrix} C_W [I_W]^d & C_W [I_G^{CMG}]^d [\omega_T]^d \\ +C_T \left( [I_W]^d [\Omega]^d - [I_G^{CMG}]^d [\omega_W]^d \right) \end{bmatrix}, \end{aligned} \quad (6-5)$$

$\Omega(t) \in \mathbb{R}^4$  denotes the wheel angular velocity, and  $\dot{\eta}(t) \in \mathbb{R}^8$  denotes the time derivative of  $\eta(t) = \begin{bmatrix} \Omega^T(t) & \delta^T(t) \end{bmatrix}^T$ . Since  $\eta(t)$  depends on reaction caused by the satellite tracking corresponding to conservation of angular momentum, provided that the satellite trajectory is bounded,  $\eta(t)$  can be bounded as

$$\|\eta\| \leq \rho_2, \quad (6-6)$$

where  $\rho_2 \in \mathbb{R}$  is a known positive bounding constant. In (6-4) and (6-5),  $C_G \triangleq \begin{bmatrix} \hat{a}_{G_1} & \hat{a}_{G_2} & \hat{a}_{G_3} & \hat{a}_{G_4} \end{bmatrix}$ ,  $C_W(\delta) \triangleq \begin{bmatrix} \hat{a}_{W_1} & \hat{a}_{W_2} & \hat{a}_{W_3} & \hat{a}_{W_4} \end{bmatrix}$ , and  $C_T(\delta) \triangleq \begin{bmatrix} \hat{a}_{T_1} & \hat{a}_{T_2} \\ \hat{a}_{T_3} & \hat{a}_{T_4} \end{bmatrix} \in \mathbb{R}^{3 \times 4}$  where  $\hat{a}_G$ ,  $\hat{a}_W$ , and  $\hat{a}_T$  are gimbal, wheel, and transverse axes. Also in (6-4) and (6-5), the inertia matrices  $[I_G^{CMG}]^d, [I_W]^d \in \mathbb{R}^{4 \times 4}$  of CMG unit are denoted as  $[I_G^{CMG}]^d \triangleq \text{diag} \left( \begin{bmatrix} I_G^{CMG_1} & I_G^{CMG_2} & I_G^{CMG_3} & I_G^{CMG_4} \end{bmatrix} \right)$  and  $[I_W]^d \triangleq \text{diag} \left( \begin{bmatrix} I_{W_1} & I_{W_2} & I_{W_3} & I_{W_4} \end{bmatrix} \right)$ , and the angular velocity projected to the gimbal-fixed axes is denoted as  $[\omega_\circ]^d \triangleq \text{diag} \left( \begin{bmatrix} \omega_{\circ_1} & \omega_{\circ_2} & \omega_{\circ_3} & \omega_{\circ_4} \end{bmatrix} \right)$  ( $\circ : G, W, T$ )  $\in \mathbb{R}^{4 \times 4}$ , and  $[\Omega(t)]^d$  and  $[\dot{\delta}(t)]^d$  denote diagonal matrices composed of the vector elements of  $\Omega(t)$ ,  $\dot{\delta}(t) \in \mathbb{R}^4$ , respectively. The expression in (6-4) represents the actuator dynamics. The subsequent development focuses on designing the composite VSCMG control inputs  $\dot{\Omega}(t)$  and  $\dot{\delta}(t)$  to impart a desired torque on the satellite body.

## 6.2 Control Objectives

### 6.2.1 Attitude Control Objective

The attitude control objective is to develop a flywheel acceleration and gimbal rate control law to enable the attitude of  $\mathcal{F}$  to track the attitude of  $\mathcal{F}_d$ . The tracking error formulation is quantified in 3.2.1 in Chapter 3. From the definitions of the quaternion tracking error variables, the following constraint can be developed [16]:

$$e_v^T e_v + e_0^2 = 1, \quad (6-7)$$

where

$$0 \leq \|e_v(t)\| \leq 1 \quad 0 \leq |e_0(t)| \leq 1, \quad (6-8)$$

where  $\|\cdot\|$  represents the standard Euclidean norm.

### 6.2.2 Flywheel Angular Momentum Management Objective

The flywheel angular momentum management objective in this chapter is to develop a flywheel acceleration control law so that the actual angular momentum  $h(\Omega) = I_W \Omega(t) \in \mathbb{R}^4$  tracks a desired constant angular momentum  $h_d = I_W \Omega_d$  while simultaneously tracking a desired time-varying attitude. The angular momentum tracking error  $\mu(\Omega) \in \mathbb{R}^4$  is quantified in the sense that (5-2) of Chapter 5 is determined.

## 6.3 Adaptive RNN Controller

### 6.3.1 Adaptive Attitude Control Development

#### 6.3.1.1 Open-Loop Error System

To facilitate the control design, an auxiliary signal  $r(t) \in \mathbb{R}^3$  is defined as [23]

$$r \triangleq \omega - \tilde{R}\omega_d + \alpha e_v, \quad (6-9)$$

where  $\alpha \in \mathbb{R}^{3 \times 3}$  is a constant, positive definite, diagonal control gain matrix. Motivation for the design of  $r(t)$  is based on the subsequent Lyapunov-based stability analysis. After multiplying the time derivative of (6-9) by  $J(\delta)$  and using (6-1) and (6-4), the open-loop

error dynamics for  $r(t)$  can be written as

$$J\dot{r} = -Q\dot{\eta} + C_G [I_W]^d [\omega_T]^d \Omega - C_T [I_W]^d [\omega_G]^d \Omega - \tau_d + Y_1\theta_1 - \frac{1}{2}Jr, \quad (6-10)$$

where the term  $C_G [I_G^{CMG}]^d \ddot{\delta}$  is assumed to be negligible [26, 83, 89], and  $Q(e_v, r, \omega, \delta, \Omega) \in \mathbb{R}^{3 \times 8}$  is defined as

$$\begin{aligned} Q \triangleq & \begin{bmatrix} C_W [I_W]^d \\ C_W [I_G^{CMG}]^d [\omega_T]^d + C_T \left( [I_W]^d [\Omega]^d \right. \\ \left. - [I_G^{CMG}]^d [\omega_W]^d \right) + \frac{\partial J}{\partial \delta} \left( \frac{1}{2}r + \tilde{R}\omega_d - \alpha e_v \right) \end{bmatrix}. \end{aligned}$$

In (6-10),  $Y_1(e_v, e_0, \omega, \delta) \in \mathbb{R}^{3 \times p_1}$  is a measurable regression matrix, and  $\theta_1 \in \mathbb{R}^{p_1}$  is a vector of  $p_1$  unknown constants defined via the parameterization

$$Y_1\theta_1 \triangleq -\omega \times J\omega + J\omega^\times \tilde{R}\omega_d - J\tilde{R}\dot{\omega}_d + \frac{1}{2}J\alpha (e_v^\times + e_0 I_3) \tilde{\omega}. \quad (6-11)$$

To compensate for the linearly parametrizable uncertainty in  $Q(e_v, r, \omega, \delta, \Omega)$ , the following parameterization will be defined:

$$Y_2\theta_2 \triangleq -Q\dot{\eta}, \quad (6-12)$$

where  $Y_2(e_v, r, \omega, \delta, \Omega, \dot{\delta}, \dot{\Omega}) \in \mathbb{R}^{3 \times p_2}$  is a measurable regression matrix, and  $\theta_2 \in \mathbb{R}^{p_2}$  is a vector of  $p_2$  unknown constants. To address the fact that the control input  $\dot{\eta}(t)$  is premultiplied by the nonsquare, time-varying uncertain matrix  $Q(e_v, r, \omega, \delta, \Omega)$ , an estimate  $\hat{Q}(t) \in \mathbb{R}^{3 \times 8}$  of the uncertainty in (6-12) is defined via

$$Y_2\hat{\theta}_2 \triangleq -\hat{Q}\dot{\eta}, \quad (6-13)$$

where  $\hat{\theta}_2(t) \in \mathbb{R}^{p_2}$  is a subsequently designed estimate for the parametric uncertainty in  $Q(e_v, r, \omega, \delta, \Omega)$ . Based on (6-12) and (6-13), the expression in (6-10) can be written as

$$J\dot{r} = Y_2\tilde{\theta}_2 - \hat{Q}\dot{\eta} + Y_1\theta_1 + C_G [I_W]^d [\omega_T]^d \Omega - C_T [I_W]^d [\omega_G]^d \Omega - \tau_d - \frac{1}{2}Jr, \quad (6-14)$$

where the notation  $\tilde{\theta}_2(t) \in \mathbb{R}^{p_2}$  is defined as

$$\tilde{\theta}_2 = \theta_2 - \hat{\theta}_2. \quad (6-15)$$

Based on the open-loop error dynamics of (6-14) and the composite VSCMG steering law of (6-4), the required control torque  $L_r(e_v, r, \dot{\delta}) \in \mathbb{R}^3$  of (6-4) is designed as

$$L_r = -Y_1 \hat{\theta}_1 - (k_1 + k_a) r - e_v + \frac{\partial J}{\partial \delta} \dot{\delta} \left( \frac{1}{2} r + \tilde{R} \omega_d - \alpha e_v \right). \quad (6-16)$$

After substituting (6-16) into (6-4) and performing some algebraic manipulations, the resulting expression for the composite VSCMG steering law can be written as

$$Y_2 \tilde{\theta}_2 - \hat{Q} \dot{\eta} + C_G [I_W]^d [\omega_T]^d \Omega - C_T [I_W]^d [\omega_G]^d \Omega = -Y_1 \hat{\theta}_1 - (k_1 + k_a) r - e_v, \quad (6-17)$$

where  $k_1, k_a \in \mathbb{R}$  are positive constant gains. By exploiting the universal approximation property of NNs, the terms  $C_G [I_W]^d [\omega_T]^d \Omega - C_T [I_W]^d [\omega_G]^d \Omega$  in (6-16) can be represented as

$$C_G [I_W]^d [\omega_T]^d \Omega - C_T [I_W]^d [\omega_G]^d \Omega = f(\chi), \quad (6-18)$$

where  $\chi \triangleq \begin{bmatrix} e_v^T & r^T & \eta^T \end{bmatrix}^T \in \mathbb{R}^{14}$ , and  $f(\chi)$  is defined as

$$f(\chi) \triangleq W^T \sigma(V^T \chi) + \varepsilon(\chi). \quad (6-19)$$

In (6-19),  $\sigma(\cdot) \in \mathbb{R}^{N+1}$  is a basis function vector with smooth, bounded, monotonically increasing elements [3, 18, 28, 37],  $W \in \mathbb{R}^{(N+1) \times 3}$  and  $V \in \mathbb{R}^{14 \times N}$  are constant unknown matrices of ideal RNN weights,  $N$  is the number of hidden layers, and  $\varepsilon(\chi) \in \mathbb{R}^3$  denotes the functional reconstruction error.

**Remark 6.1.** For any positive constant real number  $\varepsilon_N \in \mathbb{R}$ ,  $f(\chi)$  is within  $\varepsilon_N$  of the NN range if there exist finite hidden neurons  $N$  and constant weights so that for all inputs in the compact set  $S$ , the approximation holds with

$$\|\varepsilon(\chi)\| \leq \varepsilon_N. \quad (6-20)$$

The Stone-Weierstrass theorem indicates that any sufficiently smooth function can be approximated by a suitably large network. Therefore, the fact that the approximation error  $\varepsilon(\chi)$  is bounded follows from the universal approximation property of NNs.

Substituting (6-19) into (6-14) yields

$$J\dot{r} = Y_2\tilde{\theta}_2 - \hat{Q}\dot{\eta} + Y_1\theta_1 + W^T\sigma(V^T\chi) + \varepsilon(\chi) - \tau_d - \frac{1}{2}Jr. \quad (6-21)$$

Based on (6-21) and the subsequent stability analysis, the desired steering law can be designed as

$$\begin{aligned} \dot{\eta} = & \hat{Q}_w^+ \left\{ W^T\sigma(V^T\chi) + \varepsilon + Y_1\hat{\theta}_1 + (k_1 + k_a)r + e_v \right\} \\ & - (k_2 + k_b)\eta + \left( I_8 - \hat{Q}_w^+\hat{Q} \right) S\varphi, \end{aligned} \quad (6-22)$$

where  $\hat{Q}_w^+(\delta, t) = W_c(\delta)\hat{Q}^T(t)\left(\hat{Q}(t)W_c(\delta)\hat{Q}^T(t)\right)^{-1}$ , and  $k_2, k_b \in \mathbb{R}$  are positive constant gains, and  $W_c(\delta) \in \mathbb{R}^{8 \times 8}$  denotes a weight matrix determining whether the VSCMG system uses a CMG mode or a RW mode designed as [87, 89, 101]

$$W_c \triangleq \begin{bmatrix} W_\Omega I_{4 \times 4} & 0_{4 \times 4} \\ 0_{4 \times 4} & W_\delta I_{4 \times 4} \end{bmatrix},$$

where  $W_\Omega(\delta) \in \mathbb{R}$  is defined as

$$W_\Omega \triangleq W_{\Omega 0} \exp(\lambda_1 h),$$

where  $\lambda_1, W_{\Omega 0}, W_\delta \in \mathbb{R}$  are positive constants, and the objective function  $h(\delta) \in \mathbb{R}$  measuring the singularity can be denoted as

$$h \triangleq -\det(C_T C_T^T). \quad (6-23)$$

In (6-22), the second term  $\left( I_8 - \hat{Q}_w^+(t)\hat{Q}(t) \right) S(\delta)\varphi(t)$  generates the VSCMG null motion for momentum management and singularity avoidance. Since the matrices  $\hat{Q}_w^+(t)$  and  $\hat{Q}(t)$  are nonsquare, the pseudo-inverse  $\hat{Q}_w^+(t) \in \mathbb{R}^{8 \times 3}$  is defined so that  $\hat{Q}(t)\hat{Q}_w^+(t) =$

$I_3$ , and the matrix  $I_8 - \hat{Q}_w^+(t) \hat{Q}(t)$ , which projects vectors onto the null space of  $\hat{Q}(t)$ , and satisfies the properties

$$\left(I_8 - \hat{Q}_w^+ \hat{Q}\right) \left(I_8 - \hat{Q}_w^+ \hat{Q}\right) = I_8 - \hat{Q}_w^+ \hat{Q} \quad (6-24)$$

$$\hat{Q} \left(I_8 - \hat{Q}_w^+ \hat{Q}\right) = 0. \quad (6-25)$$

To generate null motion for momentum tracking and gimbal reconfiguration, the null motion  $\varphi(t) \in \mathbb{R}^{8 \times 1}$  is defined as

$$\varphi \triangleq \begin{bmatrix} k_d g \\ k_\gamma \frac{\partial \gamma}{\partial \delta} \end{bmatrix}, \quad (6-26)$$

where  $k_d \in \mathbb{R}$  denotes a positive constant, and  $g(t) \in \mathbb{R}^4$  is an auxiliary control signal to track the desired flywheel angular momentum. In (6-26),  $k_\gamma \in \mathbb{R}$  denotes a positive constant and the second row allows the null motion to perform the gimbal reconfiguration corresponding to a variation of singularity measure index  $\gamma$ , which is defined as [97]

$$\gamma \triangleq \gamma_0 \exp(\lambda_2 h), \quad (6-27)$$

where the objective function  $h(\delta)$  is defined in (6-23) and  $\gamma_0, \lambda_2 \in \mathbb{R}$  denote positive constants. Also in (6-22),  $S(\delta) \in \mathbb{R}^{8 \times 8}$  selects a proper null motion based on the singularity measure. Specifically,  $S(\delta) \triangleq \text{diag}([s_w, s_g])$  is designed as

$$\begin{bmatrix} \text{sech} \left( \frac{1}{k_w \det(C_T C_T^T) + \varepsilon_s} \right) I_{4 \times 4} & 0_{4 \times 4} \\ 0_{4 \times 4} & \text{sech} (k_g \det(C_T C_T^T)) I_{4 \times 4} \end{bmatrix}, \quad (6-28)$$

where  $k_w, k_g, \varepsilon_s \in \mathbb{R}$  are positive constants. In (6-28),  $s_w, s_g$  weight either the momentum tracking or the gimbal reconfiguration corresponding to how approximate or far the CMG configuration is to a singularity.

The steering law in (6-22) cannot be implemented because it depends on the unknown ideal weight matrices  $W$  and  $V$  and the reconstruction error  $\varepsilon$ . The implemented steering law  $\dot{\hat{\eta}}(t) \in \mathbb{R}^8$  is developed based on the recursive, internode feedback-based RNN

structure as

$$\dot{\hat{\eta}} = \hat{Q}_w^+ \left\{ \hat{W}^T \sigma \left( \hat{V}^T \hat{\chi} \right) + Y_1 \hat{\theta}_1 + (k_1 + k_a) r + e_v \right\} - (k_2 + k_b) \hat{\eta} + \left( I_8 - \hat{Q}_w^+ \hat{Q} \right) \eta \quad (6-29)$$

where  $\hat{f}(\hat{\chi}) \triangleq \hat{W}^T \sigma \left( \hat{V}^T \hat{\chi} \right) \in \mathbb{R}^3$ , and  $\hat{\chi}(t)$  is defined as  $\begin{bmatrix} e_v^T & r^T & \hat{\eta}^T \end{bmatrix}^T \in \mathbb{R}^{14}$ ,  $\hat{W}(t) \in \mathbb{R}^{(N+1) \times 3}$  and  $\hat{V}(t) \in \mathbb{R}^{14 \times N}$  are estimated weights. The error equation for the RNN estimator can be obtained from (6-22) and (6-29) as

$$\dot{\tilde{\eta}} = \hat{Q}_w^+ \left\{ W^T \sigma \left( V^T \chi \right) - \hat{W}^T \sigma \left( \hat{V}^T \hat{\chi} \right) + \varepsilon \right\} - (k_2 + k_b) \tilde{\eta}, \quad (6-30)$$

where the estimation mismatch  $\tilde{\eta}(t) \in \mathbb{R}^8$  is defined as

$$\tilde{\eta} \triangleq \eta - \hat{\eta}. \quad (6-31)$$

To facilitate the subsequent closed-loop analysis, the open loop equation for  $r(t)$  in (6-21) can be rewritten as

$$J\dot{r} = Y_2 \tilde{\theta}_2 - \hat{Q} \dot{\hat{\eta}} - \hat{Q} \dot{\tilde{\eta}} + Y_1 \theta_1 + W^T \sigma \left( V^T \chi \right) + \varepsilon(\chi) - \tau_d - \frac{1}{2} J r. \quad (6-32)$$

### 6.3.1.2 Closed-Loop Error System

The steering law  $\dot{\hat{\eta}}(t)$  functioning as a control input is designed as a self-tuning adaptive controller constructed in terms of the estimate function  $\hat{W}^T \sigma \left( \hat{V}^T \hat{\chi} \right)$  resulting from the RNN structure where the weights  $\hat{W}(t)$ ,  $\hat{V}(t)$  are updated online via adaptation laws. Substituting (6-29) and (6-30) into (6-32) yields

$$J\dot{r} = Y_1 \tilde{\theta}_1 + Y_2 \tilde{\theta}_2 - (k_1 + k_a) r + (k_2 + k_b) \hat{Q} \eta - e_v - \tau_d - \frac{1}{2} J r, \quad (6-33)$$

where the notation  $\tilde{\theta}_1(t) \in \mathbb{R}^{p_1}$  is defined as

$$\tilde{\theta}_1 = \theta_1 - \hat{\theta}_1. \quad (6-34)$$

Based on (6-33) and the subsequent stability analysis, the parameter estimates  $\hat{\theta}_1(t)$  and  $\hat{\theta}_2(t)$  are solutions to the update laws

$$\dot{\hat{\theta}}_1 = \text{proj}(\Gamma_1 Y_1^T r) \quad \dot{\hat{\theta}}_2 = \text{proj}(\Gamma_2 Y_2^T r), \quad (6-35)$$

where  $\Gamma_1 \in \mathbb{R}^{p_1 \times p_1}$  and  $\Gamma_2 \in \mathbb{R}^{p_2 \times p_2}$  denote constant, positive-definite, diagonal adaptation gain matrices. In (6-35), the function  $\text{proj}(\cdot)$  denotes a projection algorithm utilized to guarantee that the  $i^{\text{th}}$  element of  $\hat{\theta}_1(t)$  and  $\hat{\theta}_2(t)$  can be bounded as

$$\underline{\theta}_{1i} \leq \hat{\theta}_{1i} \leq \bar{\theta}_{1i}, \quad \underline{\theta}_{2i} \leq \hat{\theta}_{2i} \leq \bar{\theta}_{2i}, \quad (6-36)$$

where  $\underline{\theta}_{1i}, \bar{\theta}_{1i}, \underline{\theta}_{2i}, \bar{\theta}_{2i} \in \mathbb{R}$  denote known constant lower and upper bounds for each element of  $\hat{\theta}_1(t)$  and  $\hat{\theta}_2(t)$ , respectively. Minimizing the estimation error  $\tilde{\eta}(t)$  ensures that the state estimate  $\hat{\eta}(t)$  in (6-29) dynamically approximates the system state  $\eta(t)$  in (6-22). After adding and subtracting the terms  $W^T \sigma(\hat{V}^T \hat{\chi})$  and  $W^T \sigma(V^T \hat{\chi})$  inside the bracketed expression in (6-30), the following is obtained:

$$\begin{aligned} \dot{\tilde{\eta}} &= \hat{Q}_w^+ \left\{ W^T \left[ \sigma(V^T \hat{\chi}) - \sigma(\hat{V}^T \hat{\chi}) \right] + W^T \sigma(V^T \chi) - W^T \sigma(V^T \hat{\chi}) + \tilde{W}^T \sigma(\hat{V}^T \hat{\chi}) + \varepsilon(\chi) \right\} \\ &\quad - (k_2 + k_b) \tilde{\eta}. \end{aligned} \quad (6-37)$$

The Taylor series of the vector function  $\sigma(V^T \hat{\chi})$  in the neighborhood of  $\hat{V}^T \hat{\chi}$  is

$$\sigma(V^T \hat{\chi}) = \sigma(\hat{V}^T \hat{\chi}) + \sigma'(\hat{V}^T \hat{\chi}) \tilde{V}^T \hat{\chi} + O^2(\tilde{V}^T \hat{\chi}), \quad (6-38)$$

where  $\sigma'(\hat{V}^T \hat{\chi}) \triangleq d\sigma(V^T \hat{\chi})/d(V^T \hat{\chi})|_{V^T \hat{\chi}=\hat{V}^T \hat{\chi}}$ ,  $\tilde{V}(t) \triangleq V - \hat{V}(t)$ , and  $O^2(\tilde{V}^T \hat{\chi})$  denotes higher order terms. Using the Taylor series of  $\sigma(V^T \hat{\chi})$  given in (6-38), (6-37) can be rewritten as

$$\dot{\tilde{\eta}} = \hat{Q}_w^+ \left\{ \tilde{W}^T \sigma'(\hat{V}^T \hat{\chi}) \tilde{V}^T \hat{\chi} + \tilde{W}^T \sigma(\hat{V}^T \hat{\chi}) + w \right\} - (k_2 + k_b) \tilde{\eta}, \quad (6-39)$$

where  $\tilde{W}(t) \in \mathbb{R}^{(N+1) \times 3}$  and  $\tilde{V}(t) \in \mathbb{R}^{14 \times N}$  denote the RNN weight estimate mismatches defined as

$$\tilde{W} \triangleq W - \hat{W} \quad \tilde{V} \triangleq V - \hat{V}, \quad (6-40)$$

and the disturbance term  $w(e_v, r, \hat{\eta}, t) \in \mathbb{R}^3$  is defined as

$$w \triangleq W^T \sigma(V^T \chi) - W^T \sigma(V^T \hat{\chi}) + \tilde{W}^T \sigma'(\hat{V}^T \hat{\chi}) \tilde{V}^T \hat{\chi} + W^T O^2(\tilde{V}^T \hat{\chi}) + \varepsilon. \quad (6-41)$$

The disturbance  $w(e_v, r, \hat{\eta}, t)$  in (6-41) can be upper bounded as

$$\|w\| \leq \rho_3 + \rho_4 \|z\|, \quad (6-42)$$

where  $\rho_3, \rho_4 \in \mathbb{R}$  are positive bounding constants, and  $z(t) \in \mathbb{R}^{14}$  is defined as

$$z \triangleq \begin{bmatrix} e_v^T & r^T & \tilde{\eta}^T \end{bmatrix}^T. \quad (6-43)$$

Also, based on (6-6), (6-13), and (6-36), the following inequality holds:

$$\|\hat{Q}\|_{i\infty} \leq \gamma_1 \quad \|\hat{Q}_w^+\|_{i\infty} \leq \gamma_2, \quad (6-44)$$

where  $\gamma_1, \gamma_2 \in \mathbb{R}$  are known positive bounding constants and  $\|\cdot\|_{i\infty}$  is the induced infinity norm of a matrix. Based on the subsequent stability analysis, the weight update laws for the RNN are designed via

$$\begin{aligned} \dot{\hat{W}} &= \Gamma_3 \text{proj} \left[ \sigma(\hat{V}^T \hat{\chi}) \left( \tilde{\eta}^T \hat{Q}_w^+ \right) \right] \\ \dot{\hat{V}} &= \Gamma_4 \text{proj} \left[ \hat{\chi} \left( \tilde{\eta}^T \hat{Q}_w^+ \right) \hat{W}^T \sigma'(\hat{V}^T \hat{\chi}) \right], \end{aligned} \quad (6-45)$$

where  $\Gamma_3 \in \mathbb{R}^{(N+1) \times (N+1)}$ ,  $\Gamma_4 \in \mathbb{R}^{14 \times 14}$  denote constant, positive definite, diagonal adaptation gain matrices, and  $\text{proj}(\cdot)$  denotes a projection algorithm utilized to guarantee that the  $i^{\text{th}}$  element of  $\hat{W}(t)$  and  $\hat{V}(t)$  can be bounded as

$$\underline{W}_i \leq \hat{W}_i \leq \overline{W}_i, \quad \underline{V}_i \leq \hat{V}_i \leq \overline{V}_i, \quad (6-46)$$

where  $\underline{W}_i, \overline{W}_i, \underline{V}_i$ , and  $\overline{V}_i \in \mathbb{R}$  denote known, constant lower and upper bounds for each element of  $\hat{W}(t)$  and  $\hat{V}(t)$ .

### 6.3.2 Momentum Tracking Control Development

To achieve the flywheel angular momentum management objective while maintaining the attitude stabilization, the closed-loop error system is developed in (5-30) in Chapter 5.

### 6.3.3 Stability Analysis

**Theorem 6-1:** The adaptive control law given in (6-29) resulting from the RNN structure ensures uniformly ultimately bounded (UUB) attitude tracking in the sense that

$$\|e_v\| \leq \varepsilon_0 \exp\{-\varepsilon_1 t\} + \varepsilon_2 \quad (6-47)$$

where  $\varepsilon_0, \varepsilon_1, \varepsilon_2 \in \mathbb{R}$  denote positive bounding constants while along with exponential momentum tracking in the sense that

$$\|\mu(t)\| \leq \mu(0) \exp(-I_W k_m t). \quad (6-48)$$

*Proof:* The exponential momentum tracking result is evident from (5-30) of Chapter 5.

*Proof:* Let  $V(e_v, e_0, r, \tilde{\eta}, \tilde{\theta}_1, \tilde{\theta}_2, \tilde{W}, \tilde{V}, t) \in \mathbb{R}$  be defined as the following nonnegative function:

$$\begin{aligned} V \triangleq & e_v^T e_v + (1 - e_0)^2 + \frac{1}{2} r^T J r + \frac{1}{2} \tilde{\eta}^T \tilde{\eta} + \frac{1}{2} \tilde{\theta}_1^T \Gamma_1^{-1} \tilde{\theta}_1 + \frac{1}{2} \tilde{\theta}_2^T \Gamma_2^{-1} \tilde{\theta}_2 \\ & + \frac{1}{2} \text{tr} \left( \tilde{W}^T \Gamma_3^{-1} \tilde{W} \right) + \frac{1}{2} \text{tr} \left( \tilde{V}^T \Gamma_4^{-1} \tilde{V} \right). \end{aligned} \quad (6-49)$$

Based on (6-2), (6-8), (6-31), (6-34) - (6-36), (6-40), (6-45), and (6-46), (6-49) can be upper and lower bounded as

$$c_0 \|z\|^2 + c_1 \leq V(t) \leq c_2 \|z\|^2 + c_3, \quad (6-50)$$

where  $c_0, c_1, c_2, c_3 \in \mathbb{R}$  are known positive bounding constants. After using (3-17), (6-33), and (6-39), the time derivative of  $V(t)$  can be expressed as

$$\begin{aligned}
\dot{V} &= e_v^T (e_v^\times + e_0 I_3) \tilde{\omega} + (1 - e_0) e_v^T \tilde{\omega} \\
&\quad + r^T \left\{ Y_1 \tilde{\theta}_1 + Y_2 \tilde{\theta}_2 - e_v - \tau_d \right. \\
&\quad \left. - (k_1 + k_a) r + (k_2 + k_b) \hat{Q} \eta \right\} \\
&\quad + \tilde{\eta}^T \left[ \hat{Q}_w^+ \left\{ \hat{W}^T \sigma' \left( \hat{V}^T \hat{\chi} \right) \tilde{V}^T \hat{\chi} \right\} \right. \\
&\quad \left. + \hat{Q}_w^+ \left\{ \tilde{W}^T \sigma \left( \hat{V}^T \hat{\chi} \right) \right\} + \hat{Q}_w^+ w \right. \\
&\quad \left. - (k_2 + k_b) \tilde{\eta} \right] - \tilde{\theta}_1^T \Gamma_1^{-1} \dot{\tilde{\theta}}_1 - \tilde{\theta}_2^T \Gamma_2^{-1} \dot{\tilde{\theta}}_2 \\
&\quad - \text{tr} \left( \tilde{W}^T \Gamma_3^{-1} \dot{\tilde{W}} \right) - \text{tr} \left( \tilde{V}^T \Gamma_4^{-1} \dot{\tilde{V}} \right). \tag{6-51}
\end{aligned}$$

By using (6-35) and (6-45), and exploiting the fact that  $e_v^T e_v^\times \tilde{\omega} = 0$ , (6-51) can be rewritten as

$$\begin{aligned}
\dot{V} &= - (k_1 + k_a) r^T r - \alpha e_v^T e_v - (k_2 + k_b) \tilde{\eta}^T \tilde{\eta} \\
&\quad + \tilde{\eta}^T \hat{Q}_w^+ w + (k_2 + k_b) r^T \hat{Q} \eta - r^T \tau_d. \tag{6-52}
\end{aligned}$$

Using (6-3), (6-6), (6-42), and (6-44), the resulting expression of (6-52) can be upper bounded as

$$\dot{V} \leq - (k_1 + k_a) \|r\|^2 - \alpha \|e_v\|^2 - (k_2 + k_b) \|\tilde{\eta}\|^2 + \rho_5 \|z\| + \rho_6 \|z\|^2, \tag{6-53}$$

where  $\rho_5 \triangleq (k_2 + k_b) \gamma_1 \rho_2 + \gamma_2 \rho_3 + \rho_1$  and  $\rho_6 \triangleq \gamma_2 \rho_4$ . Based on (6-43),  $\dot{V}(t)$  can be written as

$$\dot{V} \leq -\lambda_1 \|z\|^2 - \lambda_2 \|z\|^2 + \rho_5 \|z\|, \tag{6-54}$$

where  $\lambda_1 \triangleq \min(k_1, \alpha/2, k_2)$  and  $\lambda_2 \triangleq \min(k_a, \alpha/2, k_b) - \rho_6$ . After completing the squares in (6-54), the upper bound of  $\dot{V}(t)$  can be expressed as

$$\dot{V} \leq -\lambda_1 \|z\|^2 - \lambda_2 \left( \|z\| - \frac{\rho_5}{2\lambda_2} \right)^2 + \gamma_3,$$

where  $\gamma_3 \triangleq \frac{\rho_5^2}{4\lambda_2}$ . Since (6-50) can be used to lower bound  $\|z\|^2$  as

$$\|z\|^2 \geq \frac{1}{c_2}V(t) - \frac{c_3}{c_2}. \quad (6-55)$$

The lower bound of  $\|z\|^2$  in (6-55) yields

$$\dot{V} \leq -\frac{\lambda_1}{c_2}V + \gamma_4, \quad (6-56)$$

where  $\gamma_4$  is defined as

$$\gamma_4 \triangleq \frac{\lambda_1 c_3}{c_2} + \gamma_3. \quad (6-57)$$

The linear differential inequality in (6-56) can be solved as

$$V(t) \leq V(0) \exp\left\{-\frac{\lambda_1}{c_2}t\right\} + \gamma_4 \frac{c_2}{\lambda_1} \left(1 - \exp\left\{-\frac{\lambda_1}{c_2}t\right\}\right). \quad (6-58)$$

The expressions in (6-49), (6-50), and (6-58) can be used to prove that  $r(t), \tilde{\eta}(t) \in \mathcal{L}_\infty$ .

Thus, (6-9) can be used to conclude that  $\omega(t) \in \mathcal{L}_\infty$ , and from (3-7) and (6-8),  $\tilde{\omega}(t) \in \mathcal{L}_\infty$ . The attitude kinematics in (3-17) can then be used to show that  $\dot{e}_v(t), \dot{e}_0(t) \in \mathcal{L}_\infty$ .

Since  $\hat{W}(t), \hat{V}(t) \in \mathcal{L}_\infty$  from (6-46), the assumption that  $W, V \in \mathcal{L}_\infty$  can be used along

with (6-40) to prove that  $\tilde{W}(t), \tilde{V}(t) \in \mathcal{L}_\infty$ . The facts that  $e_v(t), \omega(t) \in \mathcal{L}_\infty$  can be

used along with (6-2) to show that  $Y_1(t) \in \mathcal{L}_\infty$ . Based on the assumption that  $\theta_1 \in \mathcal{L}_\infty$ ,

(6-34) and (6-36) can be used to prove that  $\tilde{\theta}_1(t) \in \mathcal{L}_\infty$ . From (6-48),  $\mu(t) \in \mathcal{L}_\infty$  and

then (5-1) and (5-2) of Chapter 5 can be used to indicate that  $\Omega(t) \in \mathcal{L}_\infty$ . The fact

that  $\delta(t)$ -dependent functions are resulting from direction cosine matrices indicates that

the functions contain  $\delta(t)$  within bounded trigonometric functions. Hence, the input

set  $\chi \triangleq \begin{bmatrix} e_v^T & r^T & \eta^T \end{bmatrix}^T \in \mathcal{L}_\infty$  in RNN network of (6-19) following the Universal

approximation theorem [3, 18]. Given that  $\tilde{\eta}(t), W, V, \hat{\theta}_1(t), r(t), e_v(t) \in \mathcal{L}_\infty$ , (6-

20), (6-22), and (6-44) can be used to prove that  $\dot{\eta}(t) \in \mathcal{L}_\infty$ . Since  $\dot{\eta}(t) \in \mathcal{L}_\infty, \dot{\delta}(t),$

$\dot{\Omega}(t) \in \mathcal{L}_\infty$ . Given that  $Y_1(t), \hat{\theta}_1(t), r(t), e_v(t), \dot{\delta}(t) \in \mathcal{L}_\infty, L_r(t) \in \mathcal{L}_\infty$  from (6-

16). Given that  $e_v(t), r(t), \eta(t) \in \mathcal{L}_\infty$ , the RNN input vector  $\chi(t) \in \mathcal{L}_\infty$ . Since  $\eta(t),$

$\tilde{\eta}(t) \in \mathcal{L}_\infty$ , (6-31) can be used to conclude that  $\hat{\eta}(t) \in \mathcal{L}_\infty$ . By utilizing the fact that

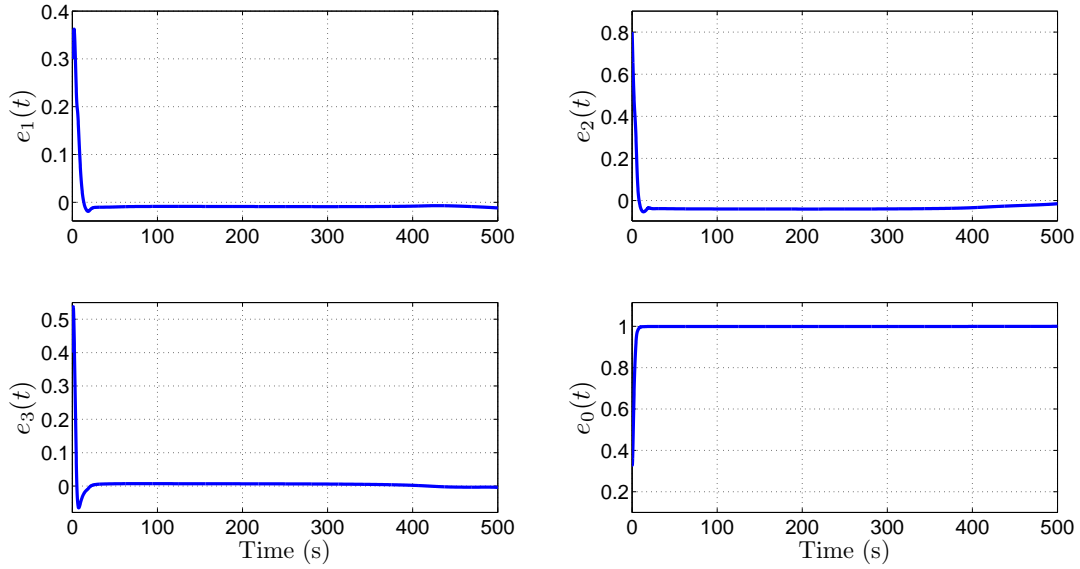


Figure 6-1. Quaternion tracking error  $e(t)$  during closed-loop operation.

$\delta(t)$ -dependent functions only contain  $\delta(t)$  within bounded trigonometric functions and  $e_v(t), r(t), \omega(t), \Omega(t), \dot{\delta}(t), \dot{\Omega}(t) \in \mathcal{L}_\infty$ , (6-12) can be used to show that  $Y_2(t) \in \mathcal{L}_\infty$ . Given that  $\hat{W}(t), \hat{V}(t), r(t), e_v(t), \hat{\theta}_1(t), \hat{\theta}_2(t), Y_1(t), v(t) \in \mathcal{L}_\infty$ , (6-29) and (6-44) can be used to prove that the control input vector  $\hat{\eta}(t) \in \mathcal{L}_\infty$ . Since  $r(t), e_v(t), \dot{\delta}(t), Y_1(t), Y_2(t), \tilde{\theta}_1(t), \tilde{\theta}_2(t) \in \mathcal{L}_\infty$  and by (6-3), (6-33) can be used to show that  $\dot{r}(t) \in \mathcal{L}_\infty$ . Standard signal chasing arguments can then be used to prove that all other signals remain bounded during closed-loop operation. The inequalities in (6-50) can be used along with (6-57) and (6-58) to conclude that

$$\|z\|^2 \leq \left( \frac{c_2 \|z(0)\|^2 + c_3}{c_0} \right) \exp \left\{ -\frac{\lambda_1}{c_2} t \right\} + \frac{\lambda_1^2 c_3 + \gamma_3 \lambda_1 c_2 - c_1}{c_0}. \quad (6-59)$$

The result in (6-47) can now be directly obtained from (6-59).

#### 6.4 Numerical Example

Numeric simulations illustrate the performance of the developed controller.

The satellite parameters are based on a model of a prototype pico-satellite which has a pyramidal arrangement of four VSCMGs. The model has the total inertia of

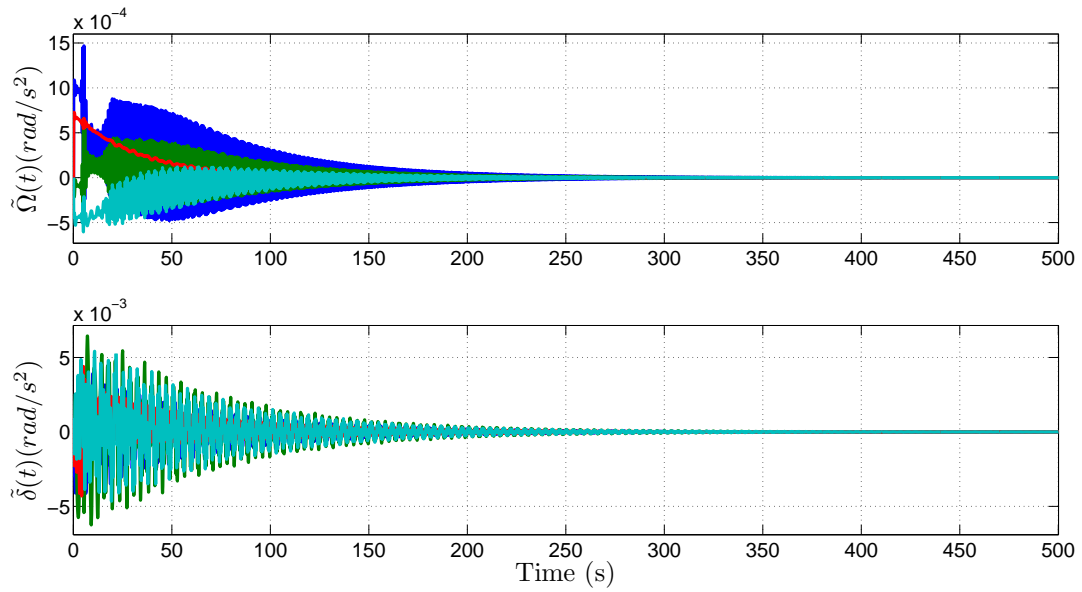


Figure 6-2. RNN estimation error  $\tilde{\eta} \left( \tilde{\Omega}, \tilde{\delta} \right)$  during closed-loop operation.

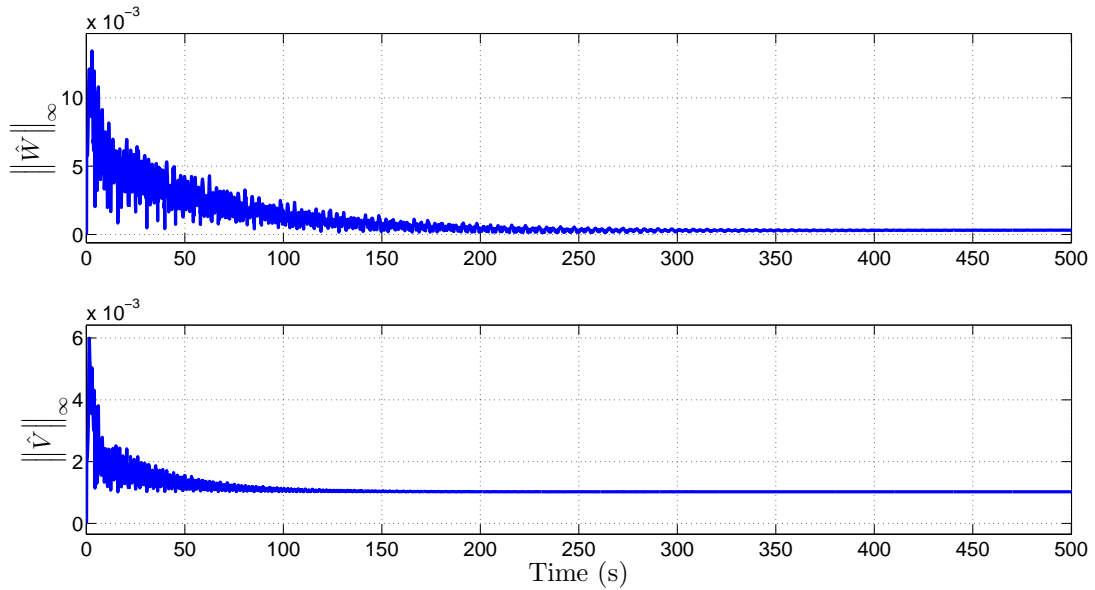


Figure 6-3. Induced infinity norm of RNN weight matrices  $\hat{W}(t), \hat{V}(t)$ .

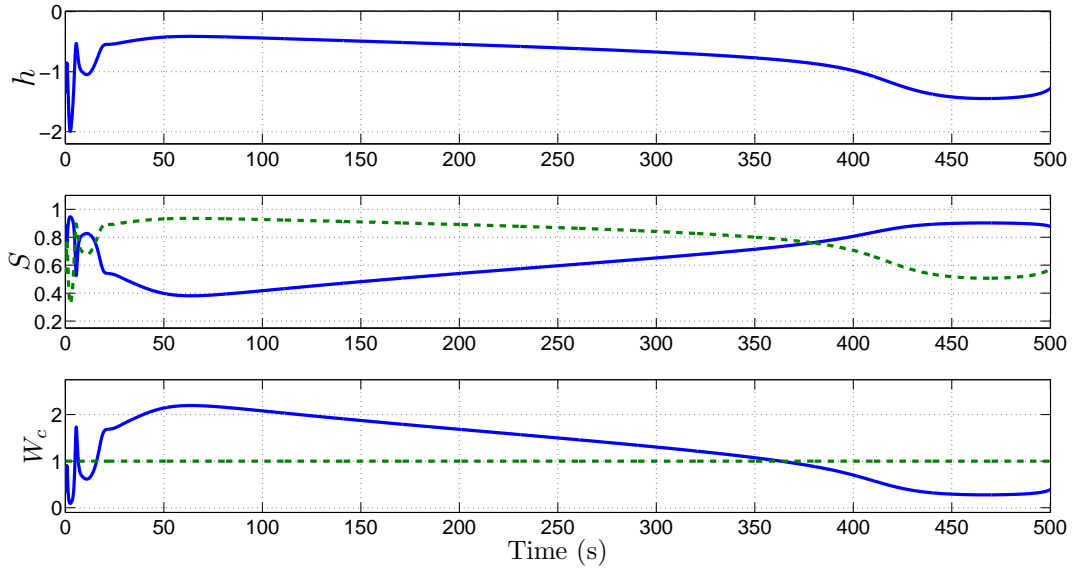


Figure 6-4. Singularity measure function  $h(\delta)$ , null motion weight  $S(\delta)$ , and mode weight  $W_c(\delta)$ .

$J_{total} = \text{diag} \left\{ 6.10 \times 10^{-2} \quad 6.10 \times 10^{-2} \quad 7.64 \times 10^{-2} \right\}$  and the VSCMG unit mass of  $m_{vscmg} = 0.165 \text{ kg}$ . The control objective is to stabilize a satellite's attitude while tracking the desired angular velocity trajectory. The simulation results are given in Figures 6-1 - 6-4. Figure 6-1 shows the quaternion tracking error results during a 500s simulation period. The RNN estimation error  $\tilde{\eta}(\tilde{\Omega}, \tilde{\delta})$  shown by Figure 6-2 illustrates a steady-state response while the RNN estimator resulting from (6-29) compensates for the actuator uncertainty. Since the state  $\eta(\Omega, \delta)$  of the nonlinear function  $f(\chi)$  is dynamically updated in the RNN structure consisting of 10 hidden layers, the state feedback actively contributes to training of weight estimates,  $\hat{W}$ ,  $\hat{V}$  shown in Figure 6-3. Also, the RNN estimator functions as the composite VSCMG steering law which arbitrates between the CMG and RW mode corresponding to mode weight  $W_c$  induced by the singularity measure  $h(\delta)$  as shown in Figure 6-4. The null motion strategy performs gimbals reconfiguration for singularity avoidance and wheel speed regularization for internal momentum management responding to null motion weight  $S$  in Figure 6-4. Although the VSCMG is a geometrically singularity-free device and the singularity avoidance is not always necessary, the singularity avoidance

method reduces/eliminates the amount of time that the VSCMG has to operate in RW mode when the CMG Jacobian becomes singular through the use of null motion.

## 6.5 Summary

In this chapter, a RNN-based control technique is presented, which achieves attitude tracking for a VSCMG-actuated satellite in the presence of uncertainty in the satellite and actuator dynamics and unmodeled external disturbances. A Lyapunov-based stability analysis is used to prove the controller achieves UUB attitude tracking while compensating for the effects of uncertain time-varying satellite inertia properties, parametric uncertainty, and nonlinear external disturbance torques. Innovative development of the error system along with a Lyapunov-based adaptive law mitigates the difficulties resulting from satellite inertia uncertainty. Numeric simulation results illustrate performance of RNN estimator which functions as a composite VSCMG steering law as well as benefits provided by gimbal and wheel null motions.

## CHAPTER 7

### A NEW SINGULARITY DETECTION METHOD FOR VSCMGs USING FLS

As seen in Chapter 4-6, the null motions of VSCMG can provide beneficial effects such as gimbal reconfiguration and internal momentum management for spacecraft operation while the motions generate no net torque from the VSCMGs. Even if the VSCMG is geometrically a singularity-free device except saturation, the singularity avoidance method using the gimbal null motion can reduce/eliminate the amount of time that the VSCMG has to operate in RW mode when the CMG Jacobian becomes singular. According to whether the total angular momentum vector is inside or outside the momentum envelope, the singular state is defined as internal or external. The CMG system encounters external (saturation) singularities when the individual angular momentum has maximum magnitude for its direction. Internal singularities can be classified into elliptic or hyperbolic singularity by whether the null motion is possible around the singular state. The null motions can be generated at the hyperbolic singularity but not at the elliptic singularity [5, 52, 55, 64, 70, 91, 96]. However, the fact that the null motion exists does not guarantee escape from the hyperbolic singularity. There are degenerate solutions which do not affect the rank of the CMG Jacobian. This means that the degenerate hyperbolic singularities cannot be escaped through null motion [5, 55, 64, 96]. If the specific type of singularity can be determined, the VSCMG can acquire more effective performance since the VSCMG can make the best use of the torque amplification in CMG mode and also utilize the wheel null motions (e.g., start-up, power reduction, etc) while properly responding each type of singularity as well as holding precise attitude control.

In this chapter, a new singularity detection method is developed using a fuzzy logic system (FLS). The FLS-based singularity detection and classification method can determine a specific type of singularity using the necessary condition for the null motion and a singularity measure. Numerical simulations demonstrate the performance of the

adaptive VSCMG steering law with FLS-based singularity detection method in the efficacy of singularity avoidance with reduced reaction wheel modes.

## 7.1 Singularity Detection Strategy

For the pyramidal arrangement of the VSCMG system, all internal singularities can be escaped through torque generation in RW mode while maintaining precise attitude tracking performance. The possibility of escape by null motion near singularity that has been studied in [5, 55, 64, 96] can be a desirable criteria to distinguish singular states. However, the singular regions inside the momentum envelope in Figure 2-3 are nonlinear and complex. For degenerate hyperbolic singularities, the surface looks like a hyperbolic singularity which can be escaped by the null motions, but have a feature of an elliptic singularity (i.e., the null motions do not affect the rank of CMG Jacobian.). In this singularity, the null displacements do not allow the singular configuration to be disturbed since the singular state is located on a point on null trajectories for a set of gimbal angle. Hence, singularity escape by the admissible null variations is not possible. Based on the given information such as the passability condition by the null motion near singularity and the singularity measure index, a FLS can be an appropriate tool. A FLS can deal with nonlinear and complex problems in the realms of search, question-answering decision and control, and provides a foundation for the development of new tools for dealing with linguistic information and knowledge representation [7, 71, 105–109]. The basic structure of a FLS is composed of a fuzzifier, fuzzy product inference engine, and defuzzifier.

### 7.1.1 Passability Condition by Null Motion near Singularity

For the VSCMG case, a null motion always exists since a VSCMG Jacobian induced by a combination of 4 gimbals and 4 wheels always spans the three-dimensional space (i.e., the rank deficiency of the VSCMG Jacobian is escapable.) [101]. The passability condition by null motions near singularity is used in CMG mode of the VSCMG system which maintains torque amplification. The test for existence of the null motion is established by a Taylor series expansion about a singular state  $\delta^s \in \mathbb{R}^4$  [5, 55, 64, 96]. Suppose that  $\delta^s$  is

a singular point and  $H(\delta^s) \in \mathbb{R}^3$  is on the singular surface, a second order Taylor series expansion of  $H(\delta)$  in the neighborhood yields

$$\begin{aligned}\delta H &= H(\delta^s + d\delta) - H(\delta^s) \\ &= \sum_{i=1}^4 \left[ \left( \frac{\partial h_i}{\partial \delta_i} \right) \Delta \delta_i + \frac{1}{2!} \left( \frac{\partial^2 h_i}{\partial \delta_i^2} \right) \Delta \delta_i^2 + \dots \right],\end{aligned}$$

where  $\Delta \delta_i$  is the gimbal angle displacement between a gimbal angle  $\delta_i$  and a singular point  $\delta_i^s$ . By using the following relations

$$\frac{\partial h_i}{\partial \delta_i} = f_i \text{ and } \frac{\partial^2 h_i}{\partial \delta_i^2} = -h_i,$$

the null motion constraint can be expressed as

$$\delta H = \sum_{i=1}^4 \left[ f_i \Delta \delta_i - \frac{1}{2!} h_i \Delta \delta_i^2 + \dots \right] = 0_{3 \times 1},$$

where  $\delta H \triangleq 0$  near a singularity since the total angular momentum  $H$  is not affected by null motion.

To obtain the constraint equation for null motion, the inner product of  $\delta H$  with an arbitrary singular vector  $u \in \mathbb{R}^3$  is

$$u \cdot \delta H \simeq -\frac{1}{2!} u \cdot \sum_{i=1}^4 h_i \Delta \delta_i^2 = -\frac{1}{2!} \sum_{i=1}^4 (u \cdot h_i) \Delta \delta_i^2,$$

where  $u = \text{null}(C_T^T(\delta))$  and  $u \cdot f_i = 0$  ( $i = 1, 2, 3, 4$ ) by the definition of a singular vector.

Hence, the second order necessary condition for null motion is written as

$$\sum_{i=1}^4 P \Delta \delta_i^2 = 0,$$

where  $P = u \cdot h_i$  denotes the projection matrix. In matrix form, the condition can be rewritten as

$$\Delta \delta^T P \Delta \delta = 0. \tag{7-1}$$

By using the null-space basis vector  $n_i \in \mathbb{R}^4$  of the CMG Jacobian matrix  $C_T(\delta) \in \mathbb{R}^{3 \times 4}$ , the null motion of gimbal angles can be represented as

$$\Delta\delta = \sum_{i=1}^{4-2} c_i n_i = Nc, \quad (7-2)$$

where  $c$  is a set of weighting coefficients denoted as  $c = (c_1, c_2)$ , and the null space  $N \in \mathbb{R}^{4 \times [4 - \text{rank}(C_T)]}$  is written as

$$N(C_T) = \{n_i \in \mathbb{R}^4 \mid C_T \cdot n_i = 0_{3 \times 1}\}.$$

Substituting (7-2) into (7-1), a necessary condition for null motion is obtained as

$$c^T Q c = 0, \quad (7-3)$$

where  $Q = N^T P N$ . The quadratic form of (7-3) represents a null motion constraint equation in the vicinity of a singular state, and can be a singularity classification criteria according to properties of (7-3): 1) definite  $Q$ , or 2) indefinite or singular  $Q$  [5, 96]. If  $Q$  is a definite matrix,  $c = 0$  is the only solution and the null motion is not possible. The definite matrix  $Q$  indicates an elliptic singularity which has no null motions. When  $Q$  is an indefinite (or singular) matrix,  $Q$  indicates a hyperbolic singularity and the null motion is possible. Although the classification criteria based on  $Q$  implies the existence of null motion, the mere possibility of null motion does not guarantee escape from a singularity. Degenerate hyperbolic singularities which do not affect the rank of the CMG Jacobian must be excluded [5, 96]. For the detection of degenerate hyperbolic one, the conventional singularity measure index denoted as  $f(\delta) \triangleq -\det(C_T(\delta) C_T^T(\delta))$  can be used to provide additional information. Such convoluted criteria to determine a type of singularity can be effectively classified by IF-THEN rules of FLS.

### 7.1.2 Fuzzification

The first step in fuzzy logic system is to convert the measured signals into a set of fuzzy variables. Specifically, the fuzzification process turns each

$sign(\text{multiplication of eigenvalues})$  of  $Q$  in (7-3) for the null motion passability conditions near singularity and a measured conventional singularity index  $f(\delta)$  into a set of fuzzy variables. Based on whether null motions are possible, the type of singularity is determined as

$$\begin{aligned} sign(\text{multiplication of eigenvalues}) > 0, & \text{ Elliptic singularity} \\ sign(\text{multiplication of eigenvalues}) \leq 0, & \text{ Hyperbolic singularity.} \end{aligned} \quad (7-4)$$

However, in this criteria, it's impossible to detect degenerate hyperbolic singularity. As an additional information for degenerate hyperbolic singularity, the conventional singularity measure index  $f(\delta)$  is used. This information supplements the null motion passability condition of (7-4). For example, let a singular state be included to a criterion of hyperbolic singularity. However, if the singularity measure index stays around zero (i.e., even though the null motions exist, the rank of CMG Jacobian is still deficient) and it occurs the variation of angular momentum by the torque generation of RW, it can be considered to be a degenerate hyperbolic singularity. The integrated IF-THEN rules for singularity detection are as follows:

$$\begin{aligned} \text{IF } sign(\text{multiplication of eigenvalues}) > 0, & \text{ THEN Elliptic Singularity} \\ \text{IF } sign(\text{multiplication of eigenvalues}) \leq 0 \text{ AND } f < 0.3, & \text{ THEN Hyperbolic Singularity} \\ \text{IF } sign(\text{multiplication of eigenvalues}) \leq 0 \text{ AND } f < 0.1, & \text{ THEN Degenerate Hyperbolic Singularity,} \end{aligned} \quad (7-5)$$

where for detecting elliptic singularity, it is not essential for the singularity measure index  $f(\delta)$  to be used since the IF clause of (7-5) clarifies the specific type of singularity. The degenerate hyperbolic singularity which does not affect the rank of CMG Jacobian makes the index  $f(\delta)$  approach to zero although the null motion exists. Hence, IF-THEN rules of FLS in (7-5) detects a type of singularity and singularity measure, and by using the determined singularity identity the steering law can determine an efficient operation mode.

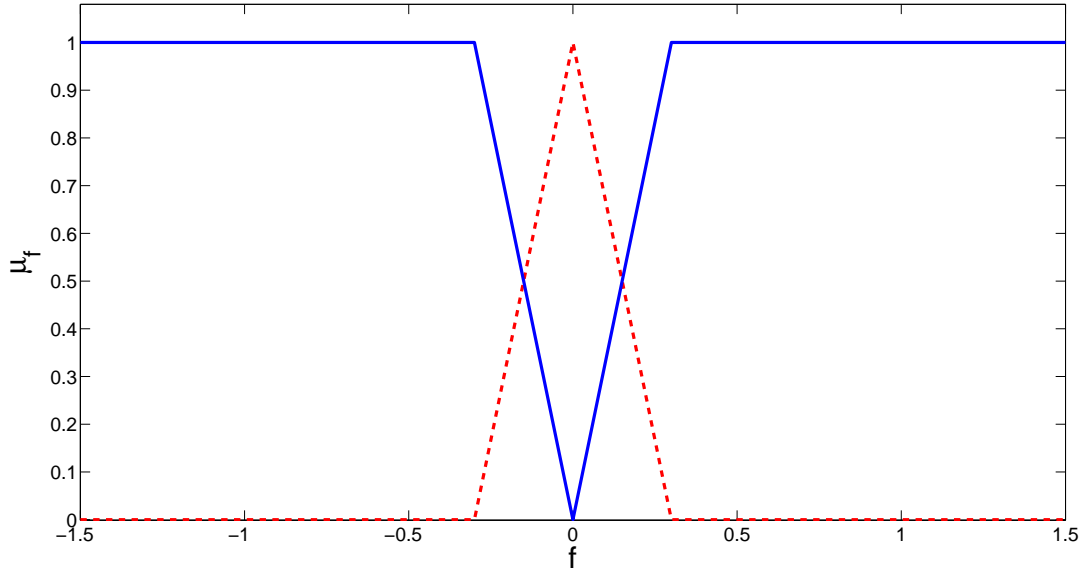


Figure 7-1. Membership function for singularity measure index  $f(\delta)$ .

Specifically,  $f(\delta) < 0.3$  in (7-5) is determined as a reference to start gimbal null motions; otherwise, the steering law does not need even gimbal null motions but needs CMG mode as a minimum norm pseudo-inverse solution. Also, in  $sign(\text{multiplication of eigenvalues}) \leq 0$  and  $f(\delta) < 0.1$ , the singularity is referred to as a degenerate hyperbolic singularity and the steering law requires the torque generation of RW. The singularity measure and threshold reference for refining hyperbolic singularity are determined and fuzzified by membership functions as shown by Figure 7-1. The dotted line fuzzifies the singularity measure index  $f(\delta)$  to additionally detect degenerate hyperbolic singularity and the region intersected by two triangles reflects fuzziness between hyperbolic singularity and degenerate hyperbolic singularity in the singularity measure index  $f(\delta)$ . Specifically, when a singularity is determined as hyperbolic singularity ( $sign(\text{multiplication of eigenvalues}) \leq 0$ ) and there exists null motions, the fact that singularity measure index  $f(\delta)$  still decrease to 0.1 under 0.3 allows RW to induce torque generation following the consecutive FLS process.

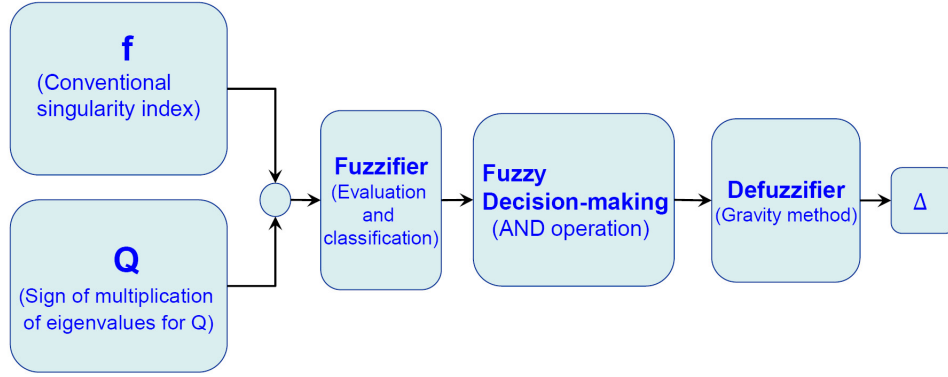


Figure 7-2. Block diagram of FLS-based singularity detection method.

### 7.1.3 Product Inference Engine

The FLS-based singularity detection method uses fuzzy equivalents of logical AND operations to build up fuzzy logic rules. If  $\mu_{sign}$  is the membership of class *sign*(multiplication of eigenvalues) for indicating a type of singularity and  $\mu_{f_i}$  is the membership of class  $f_i(\delta)$  for a conventional singularity measure, then the fuzzy AND is obtained as the multiplication of the membership values:

$$\mu_{sign \text{ AND } f_i} = \mu_{sign} \wedge \mu_{f_i} = \mu_{sign} \times \mu_{f_i}$$

where the symbol  $\wedge$  is used to denote the fuzzy AND operation and  $\mu_{sign}$  has a value of 0 or 1 (i.e., If a *sign* in (7-5) is determined,  $\mu_{sign}$  has 1).

### 7.1.4 Defuzzification

The last step in building a fuzzy logic system is turning the fuzzy variables generated by the fuzzy logic rules into a singularity detection index. The defuzzifier combines the information in the fuzzy inputs so that it obtains a single crisp output variable using the center of gravity method. To be more specific, if the fuzzy levels given in (7-5) have membership values  $\mu_{sign}$  and  $\mu_{f_i}$ , then the crisp output signal  $D_j$  is defined as

$$D_j = \frac{\sum_{i=1}^k W_i \mu_i}{\sum_{i=1}^k \mu_i} \quad (7-6)$$

where  $D_j$  ( $j = 1, 2$ ) is a defuzzified value:  $D_1$  and  $D_2$  are resulting from the rules for elliptic singularity and hyperbolic singularity, respectively,  $\mu_i$  is a fuzzified value like  $\mu_{sign}$ ,  $\mu_{f_i}$ , and  $\mu_{sign \text{ AND } f_i}$  resulting from the IF-THEN rule or the product inference engine,  $W_i$  is a weight value designed by heuristic information, and  $k$  is the number of fuzzified values. A new singularity detection index as seen in Figure 7-2 is defined as

$$\Delta = \text{sech}(D_1 + D_2 + \nu), \quad (7-7)$$

where  $\nu$  denotes a shift constant to adjust a function output signal.

## 7.2 Implementation of FLS-based singularity detection index

Based on the proposed singularity detection index  $\Delta(t)$ , the composite VSCMG steering law of Chapter 5 can be written as

$$\dot{\eta} = \hat{Q}_w^+ \left( Y_1 \hat{\theta}_1 + kr + e_v + C_G [I_W]^d [\omega_T]^d \Omega - C_T [I_W]^d [\omega_G]^d \Omega \right) + \left( I_8 - \hat{Q}_w^+ \hat{Q} \right) S \sigma, \quad (7-8)$$

where a mode weight matrix  $W(\Delta)$  is designed as

$$W \triangleq \begin{bmatrix} W_\Omega I_{4 \times 4} & 0_{4 \times 4} \\ 0_{4 \times 4} & W_\delta I_{4 \times 4} \end{bmatrix},$$

where  $W_\delta \in \mathbb{R}$  is defined as

$$W_\delta \triangleq W_{\delta 0} \Delta,$$

$W_{\delta 0}, W_\Omega \in \mathbb{R}$  are positive constants, and the new singularity detection index  $\Delta(t)$  is obtained as (7-7). Since the index  $\Delta(t)$  detects the singularity type and property of the singularity, the flywheels can generate the required torque in RW mode at elliptic singularity and degenerate hyperbolic singularity based on the FLS-based singularity detection. In (7-8), to generate null motion for internal momentum tracking and gimbal reconfiguration, the null motion  $\sigma(t) \in \mathbb{R}^8$  is defined as

$$\sigma \triangleq \begin{bmatrix} k_w g^T & k_\gamma \frac{\partial \gamma}{\partial \delta}^T \end{bmatrix}^T, \quad (7-9)$$

where  $k_w, k_\gamma \in \mathbb{R}$  denote positive constants,  $g(t) \in \mathbb{R}^4$  is an auxiliary control signal to track the desired flywheel angular momentum, and the second row is the gradient method for the gimbal reconfiguration. The matrix  $S(\Delta) \in \mathbb{R}^{8 \times 8}$  in (7-8) is a null motion weight for the VSCMG null motion denoted as

$$S \triangleq \Delta I_{8 \times 8}, \quad (7-10)$$

where  $I_{8 \times 8} \in \mathbb{R}^{8 \times 8}$  is an identity matrix. When the singularity detection index detects elliptic singularity or degenerate hyperbolic singularity, the index  $\Delta(t)$  inhibits both gimbal and wheel null motions so that the VSCMG can be operated as RW. When encountering hyperbolic singularity and in normal workspace, the steering law works for a conventional CMG with the torque amplification and internal momentum tracking.

### 7.3 Numerical Examples

#### 7.3.1 Simulation Setup

Numeric simulations illustrate the performance of the developed controller. The satellite parameters and initial conditions are based on a model of a prototype picosatellite in Table 5-1 and 5-2 of Chapter 5. The initial and desired flywheel speed for each wheel are  $\Omega_0 = \Omega_d = 200 \text{ rad/s}$  ( $\approx 2,000 \text{ rpm}$ ). The simulation parameters for defuzzification are  $W_1 = -1$ ,  $W_2 = -3$ ,  $\nu = 3$  where  $W_1$  and  $W_2$  are weight values for each membership function of Figure 7-1, and  $\nu$  is a shift constant. Differently from the initial startup of Chapter 5, the wheel null motion achieves the internal momentum tracking to maintain the desired flywheel speed so that the VSCMG system can steadily gain torque amplification in CMG mode.

#### 7.3.2 Simulation Results

The simulation results are developed to show the performance of the FLS-based singularity detection index for two cases. To illustrate the performance of the singularity detection and escape at internal elliptic singularity, Case 1 is started at an internal elliptic singular point denoted as  $\delta(0) = \begin{bmatrix} -90 & 0 & 90 & 0 \end{bmatrix} (\text{deg})$  and the results are given in

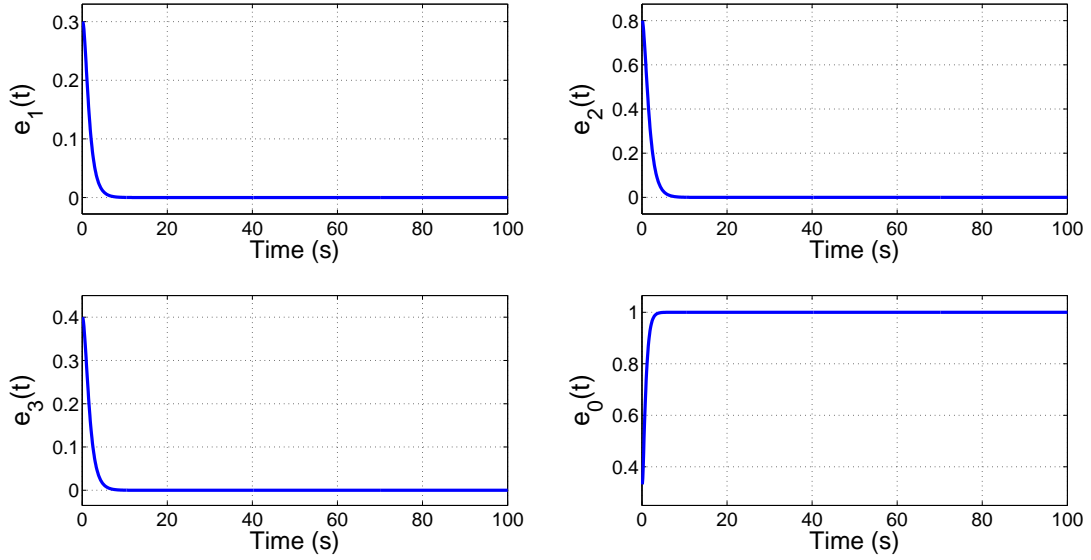


Figure 7-3. Quaternion tracking error  $e(t)$  for Case 1.

Figures 7-3 - 7-9. Case 2 is started at an internal hyperbolic singular point denoted as  $\delta(0) = \begin{bmatrix} 0 & 90 & 180 & -90 \end{bmatrix}$  (deg) and the results are given in Figures 7-10 - 7-13.

Figure 7-3 shows the quaternion tracking error results during a 100s simulation period. Figure 7-4 shows the control input gimbal rates  $\dot{\delta}(t)$  and wheel accelerations  $\dot{\Omega}(t)$ . The wheel acceleration control input  $\dot{\Omega}(t)$  contributes to the internal momentum management by equalizing the wheel speed after escaping from the internal elliptic singularity at an initial point while the control inputs achieve attitude stabilization. Since the simulation for Case 1 starts at an internal elliptic singular point, the  $\det(Q)$  regarded as multiplication of eigenvalues shows a positive sign in Figure 7-6 and the singularity measure index  $f(\delta)$  shows the start at 0 in Figure 7-7. Also, the FLS-based singularity detection index  $\Delta(t)$  inhibits both gimbal and wheel null motions while it allows a torque generation of RW as shown by Figure 7-6, 7-7, and 7-5. Once the CMG Jacobian escapes the internal elliptic singularity, the gimbal null motions help the system escape the singularity while the wheel null motions achieve wheel speed equalization (internal momentum tracking error  $\mu(t) \rightarrow 0$ ) as shown in Figure 7-8. Figure 7-9 shows the elements of the adaptive parameter vectors  $\hat{\theta}_1(t)$  and  $\hat{\theta}_2(t)$ .

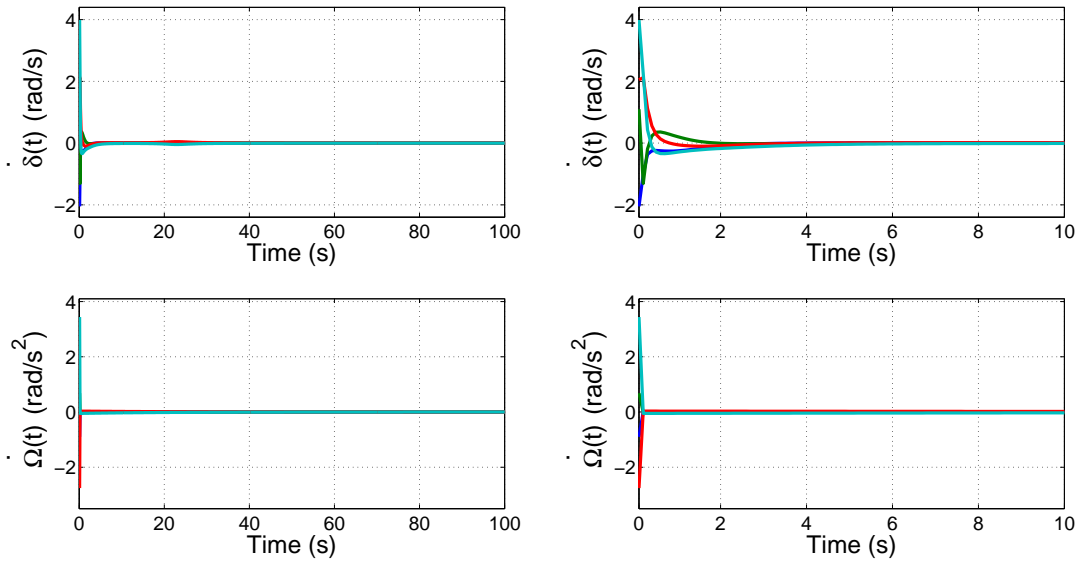


Figure 7-4. Control input gimbal rates  $\dot{\delta}(t)$  and wheel accelerations  $\dot{\Omega}(t)$  for Case 1. The left column illustrates the response for the entire duration, and the right column illustrates the transient response.

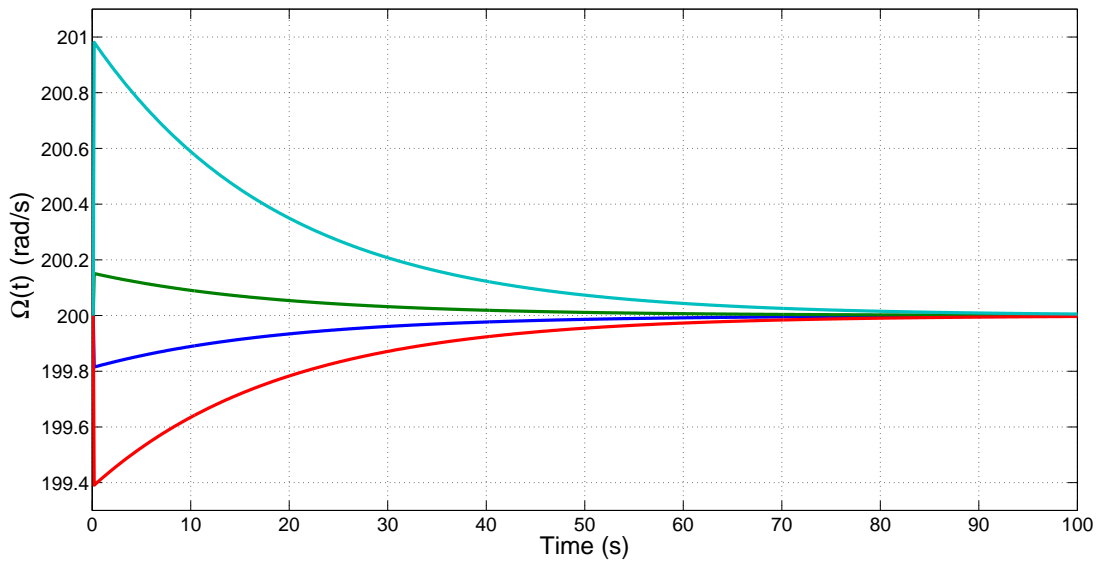


Figure 7-5. Flywheel speed  $\Omega(t)$  for Case 1.

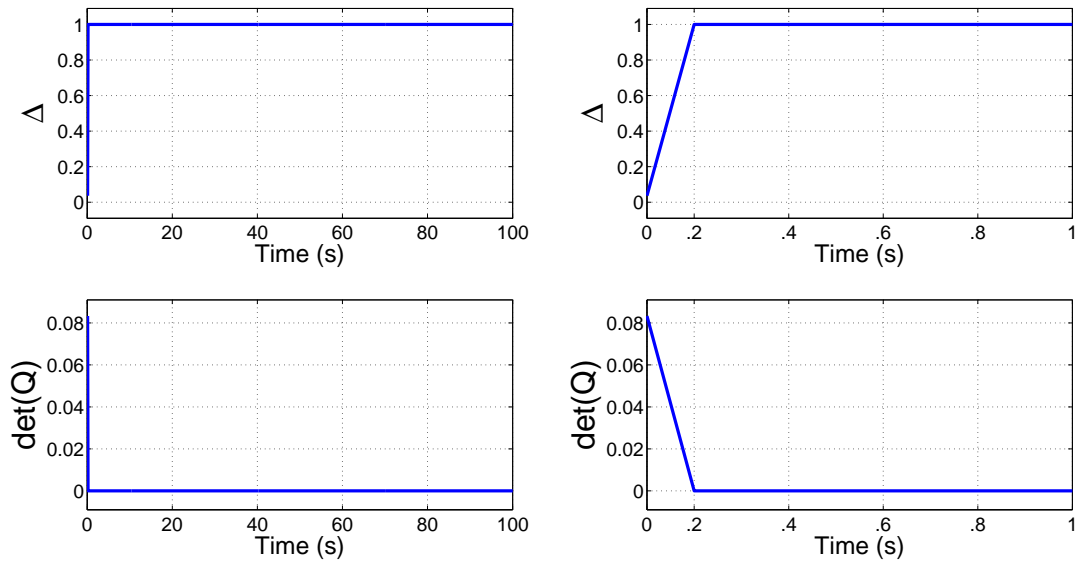


Figure 7-6. Singularity detection index  $\Delta(t)$  and null motion condition  $\det(Q)$  for Case 1. The left column illustrates the response for the entire duration, and the right column illustrates the transient response.

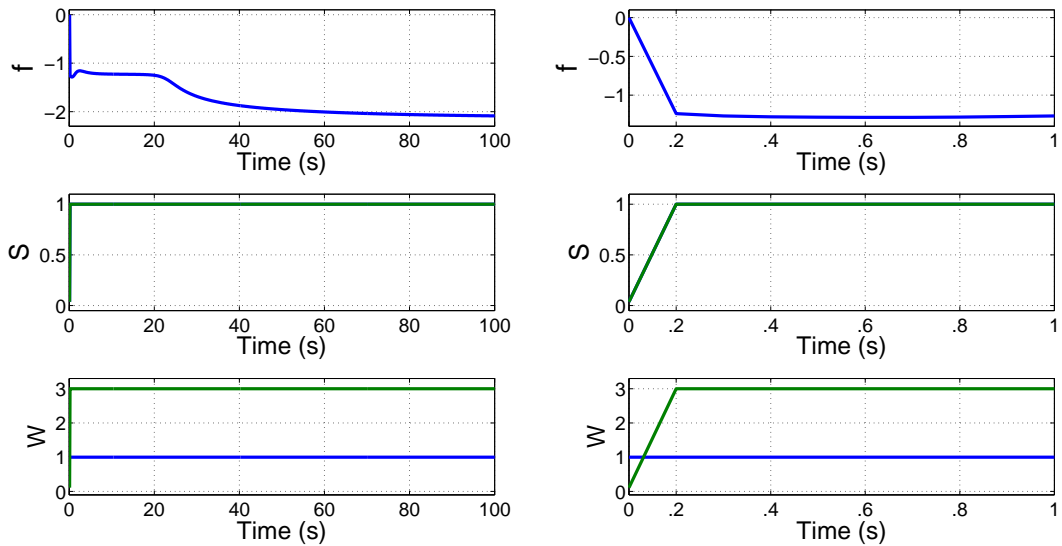


Figure 7-7. Singularity measure index  $f(\delta)$ , null motion weight  $S(\Delta)$ , and mode weight  $W(\Delta)$  for Case 1.

The left column illustrates the response for the entire duration, and the right column illustrates the transient response.

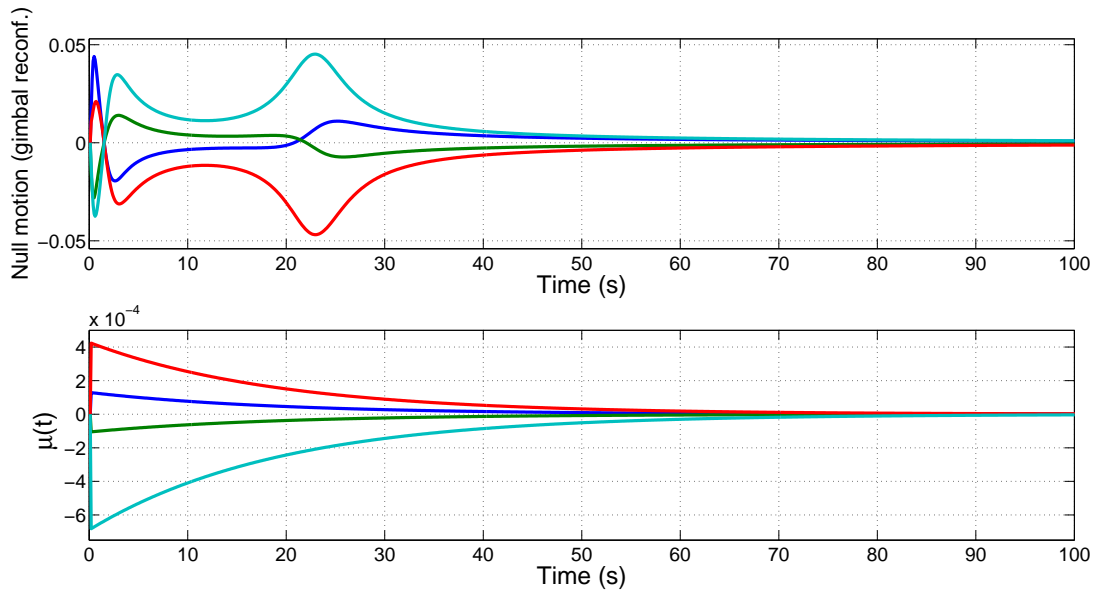


Figure 7-8. Null motion results for gimbal reconfiguration and wheel speed tracking error  $\mu(t)$  for Case 1.

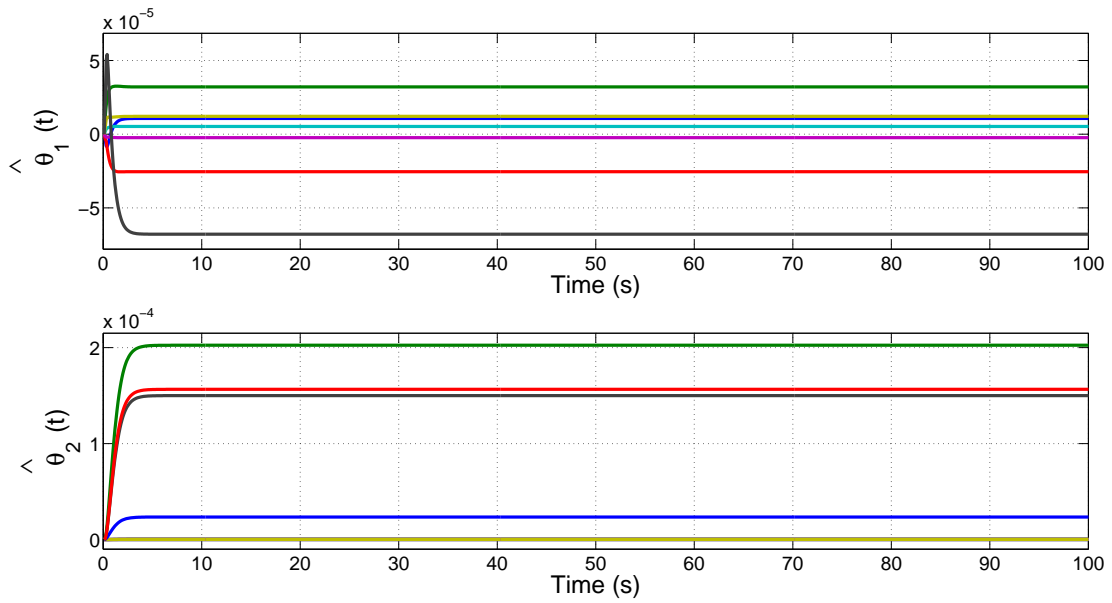


Figure 7-9. Parameter estimates  $\hat{\theta}_1(t)$ ,  $\hat{\theta}_2(t)$  for Case 1.

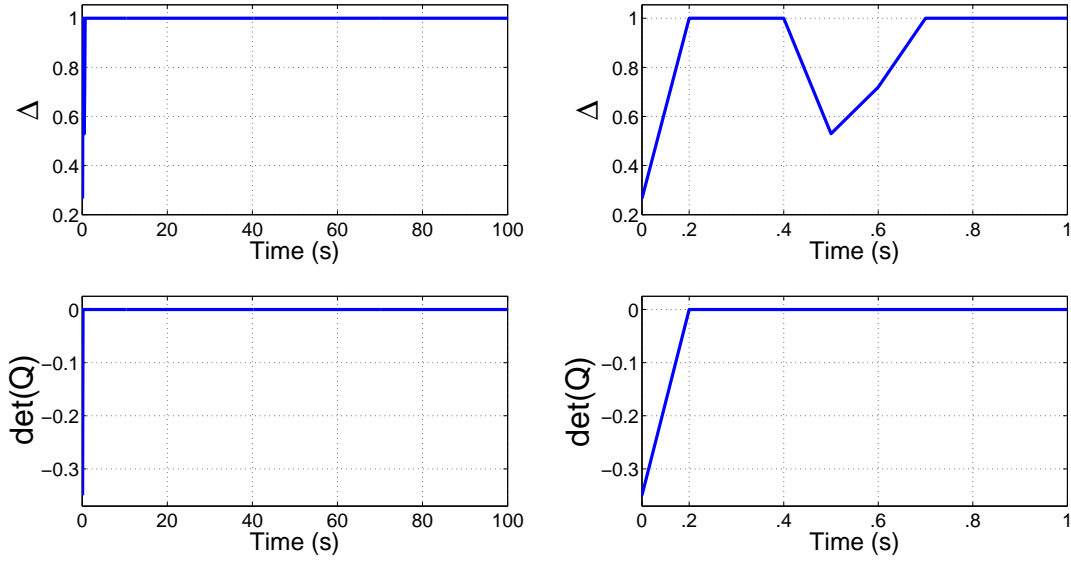


Figure 7-10. Singularity detection index  $\Delta(t)$  and null motion condition  $\det(Q)$  for Case 2.

The left column illustrates the response for the entire duration, and the right column illustrates the transient response.

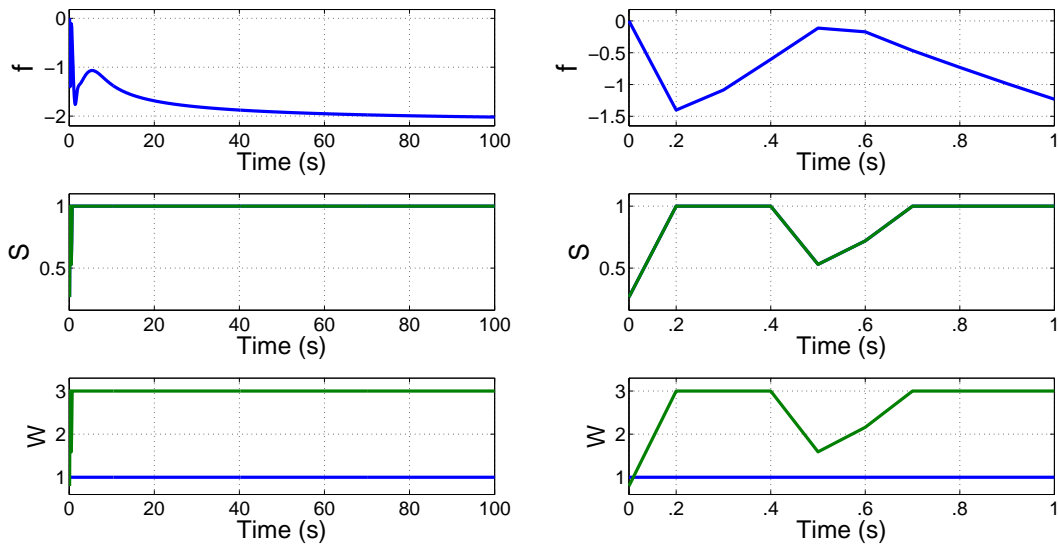


Figure 7-11. Singularity measure index  $f(\delta)$ , null motion weight  $S(\Delta)$ , and mode weight  $W(\Delta)$  for Case 2.

The left column illustrates the response for the entire duration, and the right column illustrates the transient response.

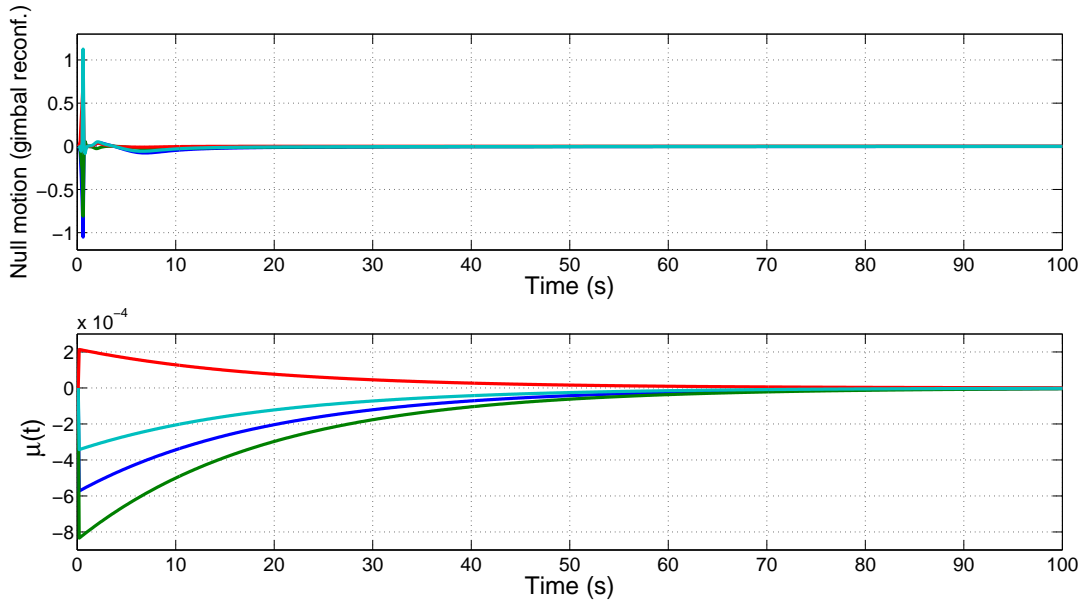


Figure 7-12. Null motion results for gimbal reconfiguration and wheel speed tracking error  $\mu(t)$  for Case 2.

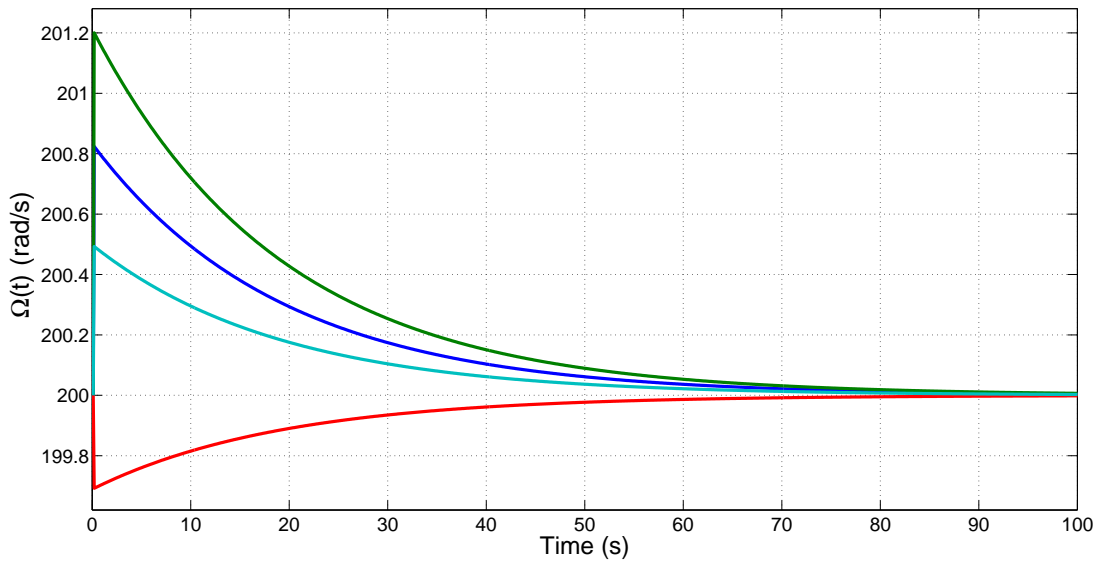


Figure 7-13. Flywheel speed  $\Omega(t)$  for Case 2.

The simulation results for Case 2 (started at an internal hyperbolic singular point) are provided in Figure 7-10 - 7-13. In Figure 7-10, the  $\det(Q)$  showing the null motion condition illustrates a negative sign at the starting point which means the start from the internal hyperbolic singularity. The singularity detection index shows two variations which are shown in Figure 7-10. The second variation is resulting from access to another singular point right after escaping from the internal hyperbolic singularity. Corresponding to the second variation of  $\Delta(t)$  and  $f(\delta)$ , the singularity encounter is escaped by the gimbal null motions without the torque generation of RW shown in Figure 7-12 and 7-13.

#### 7.4 Summary

In this chapter, a FLS-based singularity detection method is developed for the pyramidal arrangement of the VSCMG system. The FLS fuzzifies the possibility by null motion near singularity to primarily classify singularity into elliptic and hyperbolic one, and then use additional information denoted as the existing singularity measure index to even detect degenerate hyperbolic singularity. Based on the determined singularity identity, the steering law can determine an efficient operation mode depending on singularity detection input and steadily maintain torque amplification. Numeric simulations have two cases divided into elliptic and hyperbolic singularity case, and each case illustrates both the singularity detection performance and the singularity avoidance of the FLS-based singularity detection method.

## CHAPTER 8 CONCLUSIONS AND FUTURE WORK

### 8.1 Conclusions

To make the best use of an extra DOF provided by VSCMGs, various multi-functional steering laws are developed in Chapters 3 - 6. Since the VSCMG system includes satellite and actuator uncertainties such as dynamic and static friction, inertia, etc., the difficulties resulting from uncertain properties are mitigated through innovative development of the error system along with a Lyapunov-based adaptive law. The previous chapters provide the Lyapunov-based stability analysis to prove precision attitude tracking while simultaneously achieving additional tracking objectives denoted as power tracking and internal momentum tracking. Chapter 7 promotes the effective utilization of hybrid mode (i.e., CMG mode and RW mode) resulting from an extra DOF of VSCMGs. Although the VSCMG is geometrically a singularity-free device, the singularity avoidance method using the gimbal null motion can reduce/eliminate the amount of time that the VSCMG has to operate in RW mode when the CMG Jacobian becomes singular. Moreover, detecting a specific type of singularity can provide the maximum use of CMG mode to utilize torque amplification and a stable, efficient singularity avoidance effect. Hence, a FLS-based singularity detection method developed in Chapter 7 distinguishes the specific type of singularity, which arbitrates gimbal and wheel null motions so that all internal singularities can be escaped/avoided.

In Chapter 3, in dynamic and static friction in the VSCMG gimbals and wheels, the controller is capable of achieving GUUB attitude tracking while simultaneously tracking a desired power profile asymptotically. In addition, the controller compensates for the effects of uncertain, time-varying satellite inertia properties. The wheel null motions resulting from the extended DOF of VSCMGs allow the VSCMG system to accomplish a novel combined objective as precision attitude tracking and power storage (i.e., mechanical

battery). The attitude and power tracking results are proven via Lyapunov stability analysis and demonstrated through numerical simulations.

In Chapter 4, the majority of control research focused on VSCMGs has assumed ideal conditions such as frictionless flywheel and gimbal bearings and a system of VSCMGs as a rigid body. When scaling the size of CMGs/VSCMGs, the effects of friction present in the system are significant. To actively consider friction effect inside dynamics, a coupled dynamics connection of a satellite, gimbals, and wheels is developed. A backstepping method is used to develop the controller from a cascade dynamics connection for a VSCMG-actuated satellite. In the presence of uncertain dynamic and static friction in both the gimbals and the flywheels, the controller is capable of achieving globally asymptotical attitude tracking while simultaneously performing singularity avoidance and wheel deceleration. Simulations show that the applied torques of the wheels containing friction contribute to power reduction in that the friction enables the wheel to obtain more torques without an additional torque request. Such benefit is induced by the deceleration mode resulting from the null motion and can give the actuator both torque and power reduction effect.

Previous space missions using CMGs have used a separate feedback control loop to spin up the rotor to the required spin rate and maintain it while securing attitude stabilization using additional devices such as magnetorquers. In Chapter 5, the VSCMG steering law including the internal momentum management allows the flywheel to start from rest and to reach the desired speed. In the presence of satellite inertia uncertainty and actuator uncertainty, the developed attitude controller in this chapter is capable of achieving global asymptotic attitude tracking while simultaneously performing singularity avoidance and internal momentum management. The significant benefit of the developed steering law is to condense several discontinuous, separate feedback control steps such as the initial start-up and initial attitude acquisition mode into one continuous and simultaneous control step. The attitude tracking and internal momentum tracking

results are proven via a Lyapunov stability analysis and demonstrated through numerical simulations.

Chapter 6 shows a RNN-based control technique which achieves attitude tracking for a VSCMG-actuated satellite in the presence of uncertainty in the satellite and actuator dynamics and unmodeled external disturbances. The capability of RNN modeling to evolve the states corresponding to nonlinear state equations is exploited to compensate for actuator uncertainties of VSCMGs. A Lyapunov-based stability analysis is used to prove the controller achieves UUB attitude tracking while compensating for the effects of uncertain time-varying satellite inertia properties, parametric uncertainty, and nonlinear external disturbance torques. Numeric simulation results illustrate performance of the RNN estimator which functions as a composite VSCMG steering law as well as benefits provided by gimbal and wheel null motions.

In Chapter 7, a FLS-based singularity detection method is developed for the pyramidal arrangement of the VSCMG system. Since the FLS copes with complex and nonlinear patterns of singularity, the FLS provides an effective singularity detection strategy considering the passability condition for the null motion and the singularity measure index. The FLS fuzzifies the passability condition of the null motion to primarily classify singularity into elliptic and hyperbolic one, and then use additional information denoted as the existing singularity measure index to detect a degenerate hyperbolic singularity. Based on the determined singularity identity, the steering law can determine an efficient operation mode depending on singularity detection input and steadily maintain torque amplification. The developed singularity detection methods can escape all of internal singularities including degenerate hyperbolic singularity and this method is the first result that can escape all internal singularities for the pyramidal arrangement. Numeric simulations have two cases divided into elliptic and hyperbolic singularity case, and each case illustrates both the singularity detection performance and the singularity avoidance of the FLS-based singularity detection method.

## 8.2 Future Work

The IPACS method in Chapter 3 needs a electronic device to store mechanical energy in practice. It is important to compare friction energy loss of wheel with kinetic energy growth to grasp reliability of IPACS. In the same manner of Chapter 4, IPACS method can also consider actuator friction in a physical torque level. For Chapter 4, the steering law is developed by a combination between gimbal rate and wheel speed. A practical test for this steering law can illustrate a realistic effect about power reduction in despinning mode and give a comparison with a steering law developed by gimbal rate and wheel acceleration. Considering external disturbance for the initial startup method in Chapter 5, the start-up method can provide more attractive results to use the startup steering law in practice. The quantified investigation of start-up method using just one feedback loop can illustrate viable effects of the start-up method developed in Chapter 5 comparing with other start-up methods using separate feedback loop and extra devices. Hence, the hardware implementing and comparison study are required to ensure reliability for various multi-functional steering laws.

One of shortcomings of the RNN-based steering law is that UUB stability is achieved. Further investigation which includes addition of robust feedback control term or other intelligent method is needed to improve the stability result. Avenues to obtain a semi-global asymptotic result are provided in [44, 80, 81] under a set of assumptions.

The FLS-based singularity detection method developed in Chapter 7 can be also applied to SGCMG without loss of generality. Hence, the development of CMG steering law utilizing the FLS-based singularity detection method is needed and future efforts can focus on comparing the method of Chapter 7 with a variety of established CMG steering laws.

## REFERENCES

- [1] A. Altay and O. Tekinalp. Spacecraft energy storage and attitude control. In *Proc. Int. Conf. Recent Adv. Space Technol.*, pages 201–206, Istanbul, Turkey, Jun. 2005.
- [2] V. Babuska, S. M. Beatty, B. J. deBlonk, and J. L. Fausz. A review of technology developments in flywheel attitude control and energy transmission systems. In *Proc. IEEE Aerosp. Conf.*, pages 2784–2800, Chantilly, VA, Mar. 2004.
- [3] AR Barron. Universal approximation bounds for superpositions of a sigmoidal function. *IEEE Trans. Inf. Theory*, 39(3):930–945, 1993.
- [4] S. R. Bauer. Difficulties encountered in steering single gimbal cmgs. Technical Report 10E-87-09, The Charles Stark Draper Laboratory, Inc., 1987.
- [5] N. Bedrossian, J. Paradiso, E. Bergmann, and D. Rowell. Redundant single gimbal control moment gyroscope singularity analysis. *J. Guid. Contr. Dynam.*, 13(6):1096–1101, 1990.
- [6] N. Bedrossian, J. Paradiso, E. Bergmann, and D. Rowell. Steering law designs for redundant SGCMG systems. *J. Guid. Contr. Dynam.*, 13(6):1083–1089, 1991.
- [7] R. E. Bellman and L.A. Zadeh. Decision making in a fuzzy environment. *Manage. Sci.*, 17:141–164, 1970.
- [8] A. Bradford, L.M. Gomes, M. Sweeting, G. Yukse, C. Ozkaptan, and U. Orlu. Bilsat-1: A low-cost, agile, earth observation microsatellite for turkey. *Acta Astronaut.*, 53:761–769, 2003.
- [9] J. Busseuil, M. Llibre, and X. Roser. High precision mini-cmg’s and their spacecraft applications. In *AAS Guid. Control*, pages 91–107, 1998.
- [10] V. Carrara, S. E. C. Varotto, and A. Rios Neto. Satellite attitude control using multilayer perceptron neural networks. *Adv. Astronaut. Sci.*, 100:565–579, 1998.
- [11] Y. Chang, B. Lee, and S. Kim. Momentum wheel start-up method for HAUSAT-2 ultra-small satellite. *Aerosp. Sci. Technol.*, 10:168–174, 2006.
- [12] Jongsoo Choi, Antonio C. de C. Lima, and Simon Haykin. Kalman filter-trained recurrent neural equalizers for time-varying channels. *IEEE Trans. Commun.*, 53(3):472–480, Mar. 2005.
- [13] M.-T. Choi and H. Flashner. Neural-network-based spacecraft attitude control. In *Proc. AIAA Guid. Navig. Control Conf.*, Denver, CO, Aug. 2000.
- [14] D. E. Cornick. Singularity avoidance control laws for single gimbal control moment gyros. In *Proc. of AIAA Guid., Nav. and Contr. Conf.*, number Paper 79-1698, pages 20–33, Boulder, CO., Aug. 1979.

- [15] B. T. Costic, M.S. de Queiroz, D. M. Dawson, and Y. Fang. Energy management and attitude control strategies using flywheels. In *Proc. IEEE Conf. Decis. Control*, pages 3435–3440, Orlando, FL, Dec. 2001.
- [16] B.T. Costic, D.M. Dawson, M.S. de Queiroz, and V. Kapila. A quaternion-based adaptive attitude tracking controller without velocity measurements. In *Proc. IEEE Conf. Decis. Control*, volume 3, pages 2424–2429, Sydney, Australia, Dec. 2000.
- [17] J.W. Crenshaw. 2-speed, a single gimbal cmg attitude control system. Technical Report TR-243-1139, Northrop Services Inc. (NASA CR), 1972.
- [18] G. Cybenko. Approximation by superpositions of a sigmoidal function. *Math. Control Signals Syst.*, 2:303–314, 1989.
- [19] S. Das and O. Olurotimi. Noisy recurrent neural networks: The continuous-time case. *IEEE Trans. Neural Networks*, 9(5):913–936, 1998.
- [20] A. Defendini, K. Lagadec, P. Guay, and G. Griseri. Low cost cmg-based AOCS designs. In *Proc. of the 4th ESA Int. Conf. Spacecraft Guid., Nav. and Contr. Sys.*, pages 393–398, Noordwijk, The Netherlands, 1999. ESA Publishing Division.
- [21] D. A. DeVon and R. J. Fuentes. Adaptive attitude control and closed-loop power tracking for an integrated power and attitude control system using variable speed control moment gyroscopes. In *Proc. AIAA Guid. Navig. Control Conf.*, San Francisco, CA., Aug. 2005.
- [22] D. A. DeVon, R. J. Fuentes, and J. L. Fausz. Closed-loop power tracking for an integrated power and attitude control system using variable speed control moment gyroscopes. In *Proc. AIAA Guid. Navig. Control Conf.*, Providence, RI, Aug. 2004 AIAA-2004-5130.
- [23] W. E. Dixon, A. Behal, D. M. Dawson, and S. Nagarkatti. *Nonlinear Control of Engineering Systems: A Lyapunov-Based Approach*. Birkhäuser: Boston, 2003.
- [24] W. E. Dixon, Y. Fang, D. M. Dawson, and T. J. Flynn. Range identification for perspective vision systems. *IEEE Trans. Automat. Control*, 48:2232–2238, 2003.
- [25] J. L. Fausz and D. J. Richie. Flywheel simultaneous attitude control and energy storage using a VSCMG configuration. In *Proc. IEEE Int. Conf. Control Appl.*, pages 991–995, Anchorage, AK, Sep. 2000.
- [26] K. A. Ford and C. D. Hall. Flexible spacecraft reorientations using gimballed momentum wheels. *Adv. Astronaut. Sci.*, 97:1895–1914, 1997.
- [27] K. A. Ford and C. D. Hall. Singular direction avoidance steering for control-moment gyros. *J. Guid. Contr. Dynam.*, 23(4):648–656, 2000.
- [28] K. Funahashi and Y. Nakamura. Approximation of dynamic systems by continuous-time recurrent neural networks. *Neural Networks*, 6:801–806, 1993.

- [29] S. Di Gennaro. Adaptive robust stabilization of rigid spacecraft in presence of disturbances. In *Proc. IEEE Conf. Decis. Control*, pages 1147–1152, New Orleans, LA, Dec. 1995.
- [30] C. Hall. Integrated spacecraft power and attitude control systems using flywheels. Technical Report TR 000, Air Force Institute of Technology, 1997.
- [31] N. Hamzah and Y. Hashida. *TiungSAT-1: From Inception to Inauguration*, chapter TiungSAT-1 Momentum Wheel Commissioning, pages 73–92. Astronautic Technology, 2001.
- [32] D. M. Harland and R. D. Lorenz. *Space Systems Failures*. Springer-Praxis, 2005.
- [33] Simon Haykin. *Neural Networks and Learning Machines*. Prentice Hall, Upper Saddle River, NJ, 3rd ed. edition, 2008.
- [34] R. D. Hefner and C. H. McKenzie. A technique for maximizing the torque capability of control moment gyro systems. *Astrodynamics*, 54(AAS 83-387):905–920, 1983.
- [35] B.R. Hoelscher and S.R. Vadali. Optimal open-loop and feedback control using single gimbal control moment gyroscopes. *J. Astronaut. Sci.*, 39:431–438, 1994.
- [36] K. Hornik. Approximation capabilities of multilayer feedforward networks. *Neural Networks*, 4:251–257, 1991.
- [37] K. Hornik, M. Stinchcombe, and H. White. Multilayer feedforward networks are universal approximators. *Neural Networks*, 2:359–366, 1985.
- [38] Qinglei Hu. Neural network-based adaptive attitude tracking control for flexible spacecraft with unknown high-frequency gain. *Int. J. Adapt Control Signal Process.*, 24(6):477–489, 2009.
- [39] H. Jaeger. Tutorial on training recurrent neural networks, covering BPTT, RTRL, EKF and the "echo state network" approach. Tech. Rep. 159, German National Research Center for Information Technology, Bremen, 2002.
- [40] R. Jansen. Single axis flywheel IPACS@ 1300w, 0.8nm. In *NASA Space Power Workshop*, April 2005.
- [41] D. Jung and P. Tsiotras. An experimental validation of spacecraft attitude and power tracking with variable speed control moment gyroscopes. In *AAS Spacefl. Mech. Meet.*, Sedona, AZ, AAS Paper 07-130 2007.
- [42] H. Kennel. A control law for double-gimballed control moment gyros used for space vehicle attitude control. Technical Report TM 64536, NASA, 1997.
- [43] B.H. Kenny, R. Jansen, P. Kascak, T. Dever, and W. Santiago. Integrated power and attitude control with two flywheels. *IEEE Trans. Aero. Elec. Sys.*, 41(4):1431–1449, 2005.

- [44] D. Kim, H. T. Chung, S. Bhasin, and W. E. Dixon. Robust composite adaptive fuzzy identification and control for a class of MIMO nonlinear systems. In *Proc. Am. Control Conf.*, pages 4947–4952, San Francisco, CA, 2011.
- [45] D. Kim, F. Leve, N. Fitz-Coy, and W. E. Dixon. Adaptive attitude control for a small satellite with integrated singularity avoidance and momentum management. In *Proc. Am. Control Conf.*, pages 1015–1020, San Francisco, CA, 2011.
- [46] D. Kim, F. A. Leve, N. Fitz-Coy, and W. E. Dixon. Integrated power reduction and adaptive attitude control system of a VSCMG-based satellite. In *AAS/AIAA Space Flight Mech. Meet.*, 2011.
- [47] D. Kim, W. Mackunis, N. Fitz-Coy, and W. E. Dixon. Precision IPACS in the presence of dynamic uncertainty. *J. Astronaut. Sci.*, 58(1), 2011.
- [48] Seung-Jae Kim, M.D. Fairchild, A. Iarkov, J.J. Abbas, and R. Jung. Adaptive control of movement for neuromuscular stimulation-assisted therapy in a rodent model. *IEEE Trans. Biomed. Eng.*, 56(2):452–461, feb. 2009.
- [49] Y. Konda, T. Usuda, T. Sagami, K. Omagari, M. Kashiwa, and S. Matunaga. Development of attitude determination and control system for pico-satellite cute-1.7+APD. In *The 16th Workshop on JAXA Astrodyn. and Flight Mech.*, pages 242–247, 2006.
- [50] K. KrishnaKumar, S. Rickard, and S. Bartholomew. Adaptive neuro-control for spacecraft attitude control. *Neurocomputing*, 9:131–148, 1995.
- [51] S. Krishnan and S.R. Vadali. An inverse-free technique for attitude control of spacecraft using cmgs. *Acta Astronaut.*, 39:431–438, 1997.
- [52] H. Kurokawa. Exact singularity avoidance control of the pyramid type cmg system. In *Proc. of AIAA Guid., Nav. and Contr. Conf.*, number Paper 94-3559-CP, pages 170–180, Washington D.C., Aug. 1994.
- [53] H. Kurokawa. Constrained steering law of pyramid-type control moment gyros and ground tests. *J. Guid. Contr. Dynam.*, 20(3):445–449, 1997.
- [54] H. Kurokawa. A geometry of Single Gimbal Control Moment Gyros - singularity problem and steering law. Technical Report TR 175, Mechanical Engineering Lab., Tsukuba, Japan, Jan. 1998.
- [55] H. Kurokawa. Survey of theory and steering laws of single-gimbal control moment gyros. *J. Guid. Contr. Dynam.*, 30(5):1331–1340, 2007.
- [56] H. Kurokawa and N. Yajima. A study of cmg systems - for selection and evaluation. In *Proc. 16th Inter. Symp. Space Tech. Science*, pages 1243–1249, 1988.
- [57] H. Kurokawa, N. Yajima, and S. Usui. A study of single gimbal cmg systems. In *Proc. 15th Inter. Symp. Space Tech. Science*, pages 1219–1224, 1986.

- [58] T. Lafon and F. Parisot. The jason-1 satellite design and development status. In *Proc. of 12th AIAA/USU Conf. on Small Sat.*, 1998.
- [59] V.J. Lappas, WH Steyn, and C.I. Underwood. Attitude control for small satellites using control moment gyros. *Acta Astronaut.*, 51:101–111, 2002.
- [60] V.J. Lappas, C.I. Underwood, and W.H. Steyn. Experimental testing of a cmg cluster for agile microsattellites. In *Proc. of the 54th Int. Astronaut. Cong. of the IAF*, pages 371–377, 2003.
- [61] T. Lee and Y. Kim. Nonlinear adaptive flight control using backstepping and neural networks controller. *J. Guid. Contr. Dynam.*, 24(4):675–682, 2001.
- [62] H. Leeghim, Y. Choi, and H. Bang. Adaptive attitude control of spacecraft using neural networks. *Acta Astronaut.*, 64(7-8):778–786, April-May 2009.
- [63] F. Leve, G. Boyarko, and N. Fitz-Coy. Precise torque mapping of pico-satellite single-gimbal control moment gyroscopes. In *AAS Guid. Control Conf.*, Breckenridge, CO, 2010.
- [64] F. Leve and N. Fitz-Coy. Hybrid steering logic for single-gimbal control moment gyroscopes. *J. Guid. Contr. Dynam.*, 33(4):1202–1212, July-Aug. 2010.
- [65] F. Leve, V. Nagabhushan, and N. Fitz-Coy. P-n-P attitude control system for responsive space missions. In *Responsive Space Conf.*, April 2009.
- [66] F. Leve, A. Tatsch, and N. Fitz-Coy. A scalable control moment gyro design for attitude control of micro-, nano-, and pico-class satellites. In *AAS Guid. Control Conf.*, Breckenridge, CO, 2007.
- [67] X.-D. Li, J. L. Ho, and T. S. Chow. Approximation of dynamical time-variant systems by continuous-time recurrent neural networks. *IEEE Trans. on Circuits and Syst.*, 52(10):656–660, 2005.
- [68] W. MacKunis, K. Dupree, N. Fitz-Coy, and W. E. Dixon. Adaptive neural network satellite attitude control in the presence of inertia and CMG actuator uncertainties. In *Proc. Am. Control Conf.*, pages 2975–2980, Seattle, WA, USA, June 2008.
- [69] W. MacKunis, K. Dupree, N. Fitz-Coy, and W. E. Dixon. Adaptive satellite attitude control in the presence of inertia and CMG gimbal friction uncertainties. *J. Astronaut. Sci.*, 56:121–134, 2008.
- [70] G. Margulies and J. N. Aubrun. Geometric theory of single-gimbal control moment gyro systems. *J. Astronaut. Sci.*, 26:159–191, 1978.
- [71] J. M. Mendel. Fuzzy-logic systems for engineering - a tutorial. In *Proc. of the IEEE*, pages 345–377, March 1995.

- [72] D. T. Mirikitani and N. Nikolaev. Recursive bayesian recurrent neural networks for time-series modeling. *IEEE Trans. Neural Networks*, 21(2):262–274, Feb. 2010.
- [73] E. Montfort, M. Kessab, M. Rennie, D.P. McGuinness, P. Palomo, T. Zwartbol, and B.A. Oving. Real-time test bench with control moment gyro in the loop. In *Proc. of the 6th Int. ESA Conf. on Guid., Nav. and Contr. Syst.*, 2006.
- [74] Y. Nakamura and H. Hanafusa. Inverse kinematic solutions with singularity robustness for robot manipulator control. *J. Dyn. Syst. Meas. Contr.*, 108(3):163–171, 1986.
- [75] J. Nishida and Y. Tsubuku. Tokyo tech’s technical demonstration satellite TSUB-AME. In *Proc. of the 21st Small Sat. Conf.*, 2007.
- [76] J. E. Notti, A. Cormack, and W. J. Klein. Integrated Power/Attitude Control System (IPACS). *J. Spacecraft Rockets*, 12(5):485–491, 1975.
- [77] H. Oh and S. Vadali. Feedback control and steering laws for spacecraft using single gimbal control moment gyro. *J. Astronaut. Sci.*, 39:183–203, 1991.
- [78] J. Paradiso. Global steering of single gimballed control moment gyroscopes using a directed search. *J. Guid. Contr. Dynam.*, 15(5):1236–1244, 1992.
- [79] J. Park and A. Palazzolo. Magnetically suspended vscmg for simultaneous attitude control and power transfer IPAC service. *J. DYN. SYST.-T. ASME*, 132(5), 2010.
- [80] P. M. Patre, W. MacKunis, K. Kaiser, and W. E. Dixon. Asymptotic tracking for uncertain dynamic systems via a multilayer neural network feedforward and RISE feedback control structure. *IEEE Trans. Automat. Control*, 53(9):2180–2185, 2008.
- [81] P. M. Patre, W. Mackunis, C. Makkar, and W. E. Dixon. Asymptotic tracking for systems with structured and unstructured uncertainties. *IEEE Trans. Control Syst. Technol.*, 16:373–379, 2008.
- [82] B. Powell, G. Lang, S. Lieberman, and S. Rybak. Synthesis of double gimbal control moment gyro systems for spacecraft attitude control. In *Proc. AIAA Guid. Contr., and Flight Mech. Conf.*, pages 71–937, Hempstead, NY, Aug. 16-18 1971.
- [83] D. J. Richie, P. Tsiotras, and J. L. Fausz. Simultaneous attitude control and energy storage using VSCMGs: Theory and simulation. In *Proc. Am. Control Conf.*, pages 3973–3979, Arlington, VA, Jun. 2001.
- [84] D.J. Richie, V.J. Lappas, and G Prassinis. A Practical Small Satellite Variable-Speed Control Moment Gyroscope For Combined Energy Storage and Attitude Control. *Astronaut. Acta*, 65(11–12):1745–1764, 2009.
- [85] D.J. Richie, V.J. Lappas, and B. Wie. Practical steering law for small satellite energy storage and attitude control. *J. Guid. Contr. Dynam.*, 32(6):1898–1911, 2009.

- [86] C.M. Roithmayr, C.D. Karlgaard, R.R. Kumar, and D.M. Bose. Integrated power and attitude with spacecraft flywheels and control moment gyroscopes. *J. Guid. Contr. Dynam.*, 27(5):859–873, 2004.
- [87] H. Schaub and J. L. Junkins. Singularity avoidance using null motion and variable-speed control moment gyros. *J. Guid. Contr. Dynam.*, 23(1):11–16, 2000.
- [88] H. Schaub and J.L. Junkins. *Analytical Mechanics of Space Systems*. AIAA Education Series, New York, 2003.
- [89] H. Schaub, S. R. Vadali, and J. L. Junkins. Feedback control law for variable speed control moment gyros. *J. Astronaut. Sci.*, 46(3):307–328, Jul. 1998.
- [90] N. Sivaprakash and J. Shanmugam. Neural network based three axis satellite attitude control using only magnetic torquers. In *Proc. WSEAS Int. Conf. Neural Netw.*, pages 30–34, Lisbon, Portugal, 2005.
- [91] E. N. Tokar and V. N. Platonov. Singular surfaces in unsupported gyrodyne systems. *Cosmic Research*, 16(5):547–555, 1979.
- [92] P. Tsiotras, H. Shen, and C. Hall. Satellite attitude control and power tracking with momentum wheels. In *Proc. AAS/AIAA Astrodyn. Specialist Conf.*, Blacksburg, VA, Paper AAS 99-317 1999.
- [93] S. R. Vadali, S. Krishnan, and T. Singh. Attitude control of spacecraft using neural networks. *Adv. Astronaut. Sci.*, 82:271–285, 1993.
- [94] S. R. Vadali, H. S. Oh, and S. R. Walker. Preferred gimbal angles for single gimbal control moment gyros. *J. Guid. Contr. Dynam.*, 13(6):1090–1095, 1990.
- [95] B. Wie. New singularity escape and avoidance steering logic for control moment gyro systems. In *Proc. of AIAA Guid., Nav. and Contr. Conf.*, number Paper 2003-5659, pages 2191–2201, Austin, TX., Aug. 2003.
- [96] B. Wie. Singularity analysis and visualization for single-gimbal control moment gyros systems. *J. Guid. Contr. Dynam.*, 27(2):271–282, March–April 2004.
- [97] B. Wie, D. Bailey, and C. Heiberg. Singularity robust steering logic for redundant single-gimbal control moment gyros. *J. Guid. Contr. Dynam.*, 24(5):865–872, 2001.
- [98] B. Wie, D. Bailey, and C. Heiberg. Rapid multitarget acquisition and pointing control of agile spacecraft. *J. Guid. Contr. Dynam.*, 25(1):96–104, 2002.
- [99] R. Q. Xie, Y. Yao, F. H. He, and K. M. Ma. Simultaneous attitude stabilization and power tracking for a spacecraft with two VSCMGs. In *Proc. IEEE Int. Conf. Control Appl.*, pages 1121–1126, San Antonio, TX, Sep. 2008.

- [100] H. Yoon and P. Tsiotras. Spacecraft adaptive attitude and power tracking with variable speed control moment gyroscopes. *J. Guid. Contr. Dynam.*, 25(6):1081–1090, Nov.-Dec. 2002.
- [101] H. Yoon and P. Tsiotras. Singularity analysis of variable-speed control moment gyros. *J. Guid. Contr. Dynam.*, 27(3):374–386, 2004.
- [102] H. Yoon and P. Tsiotras. Adaptive spacecraft attitude tracking control with actuator uncertainties. In *Proc. AIAA Guid. Navig. Control Conf.*, San Francisco, CA, 2005.
- [103] T. Yoshikawa. A steering law for three double gimbal control moment gyro systems. Technical Report TM-X-64926, NASA, 1975.
- [104] T. Yoshikawa. Steering law for roof type configuration control moment gyro system. *Automatica*, 13:359–368, 1979.
- [105] L.A. Zadeh. Fuzzy sets. *Inform. Control*, 8:338–353, 1965.
- [106] L.A. Zadeh. Fuzzy algorithm. *Inform. Control*, 12:94–102, 1968.
- [107] L.A. Zadeh. Similarity relations and fuzzy orderings. *Inform. Sci.*, 3:177–200, 1971.
- [108] L.A. Zadeh. Outline of a new approach to the analysis of complex systems. *IEEE Trans. Syst. Man, Cybern.*, SMC-3(1):28–44, 1973.
- [109] L.A. Zadeh. The concept of a linguistic variable and its application to approximate reasoning: I, ii, iii. *Inform. Sci.*, 8:199–251, 1975.
- [110] J. Zhou and D. Zhou. Spacecraft attitude control with double-gimballed control moment gyroscopes. In *Proc. IEEE Int. Conf. on Robotics and Biomimetics (ROBIO 2007)*, pages 1557–1562, Piscataway, NJ, 2007.

## BIOGRAPHICAL SKETCH

Dohee Kim was born in Seoul, Korea. He received his Bachelor of Science degree in 2006 and his Master of Science degree in 2008 in the Department of Astronomy from the Yonsei University, Korea. In his master's degree thesis, he designed and developed Hardware-In-the-Loop (HIL) simulator for spacecraft attitude control. He then joined the Nonlinear Controls and Robotics (NCR) research group of the Department of Mechanical and Aerospace Engineering, University of Florida in the Fall of 2008 to pursue his doctoral research under the advisement of Warren E. Dixon.